Image-guidance in ophthalmic surgery using intraoperative optical coherence tomography

By

Mohamed Tarek El-Haddad

Dissertation

Submitted to the Faculty of the

Graduate School of Vanderbilt University

in partial fulfillment of the requirements

for the degree of

DOCTOR OF PHILOSOPHY

in

Biomedical Engineering

February 28, 2019

Nashville, Tennessee

Approved:

Yuankai Tao, Ph.D.

Benoit Dawant, Ph.D.

Karen Joos, Ph.D., MD.

Michael Miga, Ph.D.

Richard Alan-Peters, Ph.D.

Andrew Rollins, Ph.D.

DEDICATION

To Haddad Jr., and to my parents.

ACKNOWLEDGMENTS

First and foremost, I would like to thank my parents for putting up with me throughout the years that led up to this journey and for the unrelenting support they have provided me all the way. I'm extremely grateful to my brother and my cousins for the countless hours of listening that they have graciously lent me, and for the amazing vacations that have always recharged me for another extended bout of research. I cannot begin to express my thanks to Hande for lifting me up when I was at my lowest, and for always being there to celebrate the good times too. Special thanks to my friends from Cairo, especially Islam and Mahmoud, who have been with me through every step of this.

These past few years were a period of personal and academic growth, and I owe much of my academic progress to my mentors who have been very generous with their time with me. Thanks to Dr. Andrew Rollins, whose unique teaching has been key to my understanding of optics and OCT, to Dr. Karen Joos for her continuous feedback, clinical insight, and support, and to Dr. Anita Mahadevan-Jansen for her incredible support, career advice, and constructive critique. I am also very grateful to my committee members, Dr. Richard Alan-Peters, Dr. Benoit Dawant, and Dr. Michael Miga, for being tremendously helpful and for all the thought-provoking discussions and feedback. Many thanks should also go to Dr. Michael Giacomelli, whom I came to know 10 years ago, and who helped me start this journey by introducing me to my advisor. Thanks also to my friends at the DIIGI lab, especially Ivan and Joe, who have been very supportive through much of my time there.

Throughout this degree, I spent varying amounts of time at 4 different institutions: Cleveland Clinic, CSU, CWRU, and Vanderbilt. While this presented some challenges, I was very lucky to have made many friends and met many mentors at all of those places, to whom I am very grateful. Special thanks go to my friends at Vanderbilt who helped me with presentations, experiments, writing, and overall made my time here at Vanderbilt much nicer. Many thanks also to Amanda King for being problem-solver extraordinaire at the BME department and at the graduate school, and Michelle Bukowski for her incredible work with

ACKNOWLEDGMENTS

VISE and the publicity she provided for our research, whether on the VISE blog or on social media. Finally, I would like to extend my sincere gratitude to my advisor Dr. Yuankai (Kenny) Tao for the great training experience, for his mentoring and guidance, and for providing a research environment where we discussed Seinfeld almost as much as we did Fourier.

TABLE OF CONTENTS

Page

TABLE OF CONTENTS

TABLE OF CONTENTS

TABLE OF CONTENTS

TABLE OF CONTENTS

LIST OF TABLES

Table Page

LIST OF FIGURES

Figure Page

LIST OF FIGURES

Chapter 1

1. Background and significance

The following chapter is adapted from M. T. El-Haddad and Y. K. Tao, "Advances in intraoperative optical coherence tomography for surgical guidance," Curr. Opin. Biomed. Eng. (2017).

1.1. Fundamentals of OCT

OCT relies on low-coherence interferometry [1]images of subsurface microstructures. Light from a broadband source is split in power by a beamsplitter to reference and sample beams. Reflections from the reference and the sample are recombined at the beamsplitter where they are interfered, and detected by a square-law photodetector (Figure 1-1). The acquired signal provides a profile of sample reflectivity over depth (A-scan), which results from refractive index variations in the sample. By scanning the sample beam, A-scans can be acquired at adjacent positions and stacked to form two-dimensional (2D) images (B-scans), and three-dimensional (3D) volumes.

In spectral-domain OCT (SD-OCT), the interference pattern is detected as a function of wavelength by a spectrometer and a line-detector. In swept-source OCT (SS-OCT), the interference pattern is recorded one wavelength at a time with a single-pixel detector as the light source sweeps through its optical tuning range.

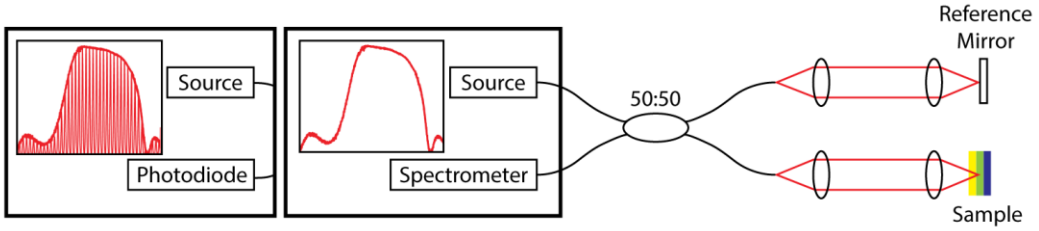

Figure 1-1 - Schematic of an OCT system with a Michelson interferometer. SS, swept-source; SD, spectral-domain.

The detected current as a function of wavenumber is given by (Eq. 1-1):

$$I_D(k) = \frac{\rho}{4}[S(k).(R_R + R_{S1} + R_{S2} + \cdots)] \quad \text{DC terms}$$

$$+ \frac{\rho}{2}[(S(k)\sum_{n=1}^{N}\sqrt{R_R R_{sn}}\cos(2k(z_R - z_{sn}))] \quad \text{Cross-correlation terms} \quad (1\text{-}1)$$

$$+ \frac{\rho}{4}[(S(k)\sum_{n\neq m=1}^{N}\sqrt{R_{sn}R_{sm}}\cos(2k(z_{sn} - z_{sm}))], \quad \text{Auto-correlation terms}$$

The design equations for an OCT system are summarized in the following table,

Signal-to-Noise Ratio (SNR)	$10Log(\frac{\rho P_s T}{e})$	$\boldsymbol{\rho}$, detector responsivity; Ps, sample power; T, A-scan rate; e, electron charge	(1-2)
Axial Resolution	$\frac{2\sqrt{\ln(2)}}{\Delta k} = \frac{2\ln(2)}{\pi}\frac{\lambda_o^2}{\Delta\lambda}$	$\boldsymbol{\lambda_o}$, source center wavelength; $\boldsymbol{\Delta\lambda}$, source optical bandwidth; $\boldsymbol{\Delta k}$, source bandwidth in wavenumber	(1-3)
6-dB Imaging Depth	$\frac{2\ln(2)}{\delta_r k} = \frac{\ln(2)}{\pi}\frac{\lambda_o^2}{\delta_r\lambda}$	$\boldsymbol{\delta_r}$, spectrometer resolution (SD-OCT) or instantaneous line-with (SS-OCT) in wavenumber and wavelength	(1-4)
Maximum Imaging Depth	$\frac{\boldsymbol{\pi}}{\boldsymbol{2\delta k}} = \frac{\boldsymbol{\lambda_o^2}}{\boldsymbol{4\delta_s\lambda}}$	**$\boldsymbol{\delta_s}$, pixel size (SD-OCT) or sampling-clock frequency (SS-OCT) in wavenumber and wavelength**	**(1-5)**

Table 1-1 - OCT design equations in wavenumber (k) and wavelength (λ) units

where ρ is the detector responsivity, S(k) the spectral shape of the source, RR is the reference reflectivity, and Rsn is the sample reflectivity, and the sample is modeled as N discrete reflectors.

The DC terms arise from non-interfering reflections from the sample and the reference mirror. The A-scan is encoded in the cross-correlation terms, where the frequency of the cosine is proportional to the axial position of the reflector, and is multiplied by a gain factor given by the reference mirror reflectivity (RM).

The auto-correlation terms arise from interference between light reflected from different scatterers within the sample and result in imaging artefacts. However, the autocorrelation signal is usually limited to small magnitudes and low frequencies, thus it is usually sufficient to ensure that the sample is kept farther away from DC during acquisition to avoid these effects.

The A-scan information is retrieved by taking the Fourier transform of the recorded spectrum (Eq. 1-1). Sample reflections transform to delta functions, and the multiplication with S(k) transforms to a convolution, so that each peak is broadened by the coherence length of the light source. Therefore, the axial point-spread function (PSF) of the system is inversely proportional to the spectral bandwidth of source (Eq. 1-3). Furthermore, due to the finite resolving power of spectrometers in SD-OCT or finite line-width of the source in SS-OCT, the signal is modulated by an envelope such that the visibility decreases with depth. A standard metric is the 6-dB imaging range which is defined as the depth at which the signal visibility is reduced to half the maximum (Eq. 1-4). Finally, the maximum imaging depth is given by the Nyquist limit which depends on the spectral sampling density due to the finite pixel width in SD-OCT or sampling clock frequency in SS-OCT (Eq. 1-5).

1.2. Intraoperative OCT in ophthalmology

Optical coherence tomography (OCT) enables non-contact exogenous contrast-free imaging of subsurface tissue microstructures [1]. When combined with latest-generation broadband light sources and detection schemes, OCT achieves 1-10 μm axial resolution at up to megahertz line-rates [2–11]. The high resolution and detection sensitivity of OCT have benefited clinical imaging in cardiology [12], gastroenterology [13], and oncology [14–16], and OCT is currently the gold standard for ophthalmic diagnostics [17,18]. Over the last decade, translation of OCT technologies to applications in surgical planning and guidance in ophthalmology [19–29] and other specialties [15,30–43] has been an active area of research and commercialization. Benefits of intraoperative OCT include verification that surgical goals

have been achieved; enhanced contrast using optical or computational methods; improved axial resolution and visualization of subsurface features-of-interested as compared to surgical stereomicroscopy; image-guided surgical maneuvers, especially during minimally invasive and microsurgical procedures; and real-time feedback on interactions between surgical instruments and underlying tissue morphology.

Technological innovations, thus far, have primarily focused on addressing barriers to translating OCT into the surgical suite. The need for optimal surgical ergonomics and optical performance has led to novel scanner designs for handheld imaging probes [19,21–23,44–47], surgical instrumentation [26,28,29], and microscope-integrated systems [20,24,27,48]. Concurrently, advances in parallel detection [17,18,49–52] and novel high-speed swept laser sources [4–6] have led to significant increases in imaging speeds, which allow for denser spatiotemporal sampling and reduced motion-induced artefacts when imaging surgical dynamics. To achieve real-time feedback, novel image-processing algorithms and visualization hardware have enabled rendering and display of three- [53] and four-dimensional (several volumes-per-second) [24,54–56] data. Finally, OCT has been integrated with complementary technologies for precision guidance of micro-surgical maneuvers that include augmented reality (AR) overlays of volumetric OCT data onto the surgical microscope view [27] using heads-up display (HUD) [48,57] and commercial virtual reality (VR) headsets [58,59]; depth stabilization [60–62], and active tremor cancelation [63]; and integrated surgical tools for robotic-assisted surgery [64,65].

Ophthalmology is by far the largest market for intraoperative OCT and drives much of the research and commercialization efforts in the field [66,67]. In this section, a review of the state-of-the-art and recent developments in ophthalmic intraoperative OCT technology will be given, along with a brief discussion about their clinical potential and impact.

1.2.1. Perioperative imaging with hand-held and microscope-mounted probes

Early ophthalmic OCT system designs were coupled to conventional slit-lamps which enabled high-resolution diagnostic imaging of the anterior segment [68]. However, their diagnostic utility was limited to cooperative patients who could maintain an upright position over the duration of imaging. This motivated the design of handheld systems that would allow imaging of uncooperative and supine patients, and facilitate intraoperative monitoring.

Radhakrishnan et al. described the first handheld probe for anterior segment OCT (Figure 1-2 (a)) [44]. The system employed a 1310 nm center wavelength light source, and the imaging optics were packaged into a handheld probe with a miniature single-axis galvanometer scanner that provided a lateral scan range of 5 mm at 8 frames-per-second (fps). *In vivo* imaging results showed visualization of structure and dynamics such as corneal epithelial and stromal layers, angle of the anterior chamber, and pupillary reflex due to a light stimulus. This demonstrated the potential utility of OCT for guidance in refractive surgery. Advances in detection methods led to higher imaging speeds, which allowed for larger field-of-views (FOVs) and higher sampling densities. The speed advantage has also enabled volumetric imaging [19,21] while use of MEMS scanners has substantially reduced the size of latest-generation handheld probes, which provide improved portability and ergonomics (Figure 1-2 (c)) [45,47]. In a 2009 clinical study using a commercial handheld probe (Bioptigen) (Figure 1-2 (b)), Dayani et al. showed successful perioperative visualization of macular changes due to surgical intervention in eight patients undergoing vitrectomy [19]. In a subsequent study, Ray et al. presented a custom mount that attached the Bioptigen handheld probe to an ophthalmic surgical microscope [21]. This enabled manual alignment of the OCT field using the microscope foot-pedal controls, which reduced motion artefacts as compared to handheld imaging and allowed aiming of the OCT FOV to image regions-of-interest (ROIs). In this study, OCT images from 24 patients undergoing macular hole (MH) or epiretinal membrane (ERM) surgery were analyzed. Quantitative measurement of MH geometry and retinal thickness provided novel insight into the anatomical changes in

the retina resulting from macular surgery. These observational studies were the first to demonstrate the utility of OCT for verifying completion of surgical goals and to provide image-based feedback to benefit clinical decision-making during surgical cases. More recently, a two-year prospective clinical trial (PIONEER) reported on the feasibility and safety of OCT in 531 enrolled eyes over a wide range of surgeries including cataract, bullous keratopathy, corneal graft, keratoconus, ERM, MH, retinal detachment, proliferative diabetic retinopathy, and vitreous hemorrhage [23]. The authors used a microscope-mounted handheld OCT probe [21] and concluded that intraoperative imaging enhanced surgeon understanding of the underlying anatomy in more than 40% of the cases during lamellar keratoplasty and retinal membrane peeling. Similar results were observed in retrospective [22] and prospective [69] clinical studies using handheld OCT probes from Optovue, Inc.

Despite benefits to surgical visualization, the utility of handheld probes is limited by the need for repeated pauses during surgery to acquire OCT images [21–23,69], which can increase operating time by as much as 25 minutes [23]. While handheld probes have significantly improved OCT portability and ergonomics to enable imaging of uncooperative and supine patients [19,22,45,47], broad adoption of the technology for intraoperative feedback in ophthalmology will likely be limited by the lack of a stable imaging platform, aiming capabilities and sterility concerns.

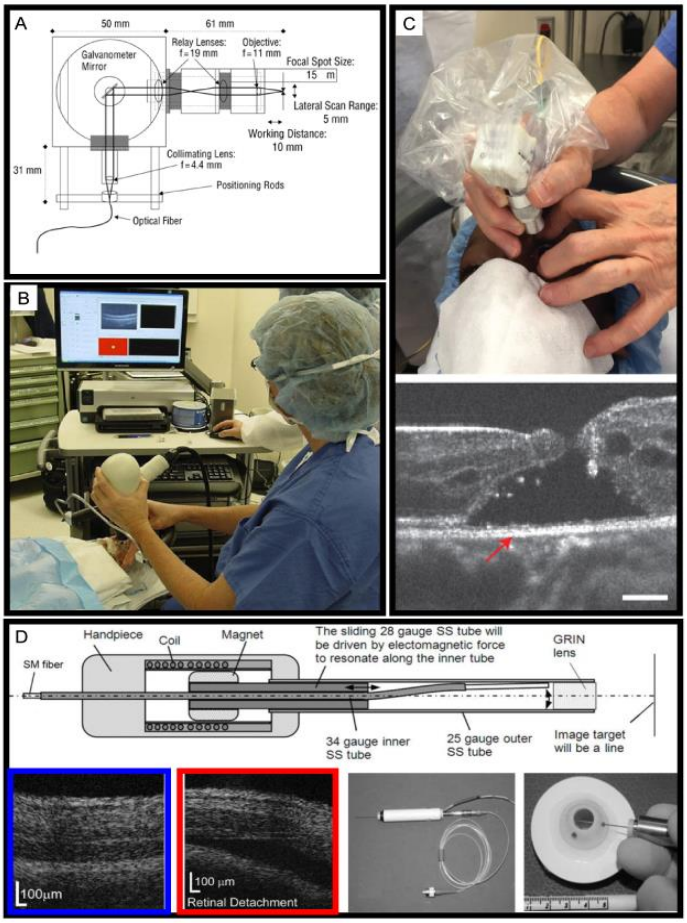

Figure 1-2 - Handheld OCT probes.(A) First handheld probe design [44]. (B) Commercial handheld probe (Bioptigen) [19]. (C) Miniaturized MEMS scanner-based handheld probe showing a B-scan of a macular hole [70]. (D) Needle-based intraocular OCT probe with B-scans showing healthy retina (blue box) and retinal detachment (red box) [26].

1.2.2. Microscope-integrated intraoperative OCT

Microscope-integrated systems combine the OCT and surgical microscope optical paths to enable imaging concurrent with surgical maneuvers [20,48,55,71–73]. Most current-generation microscope-integrated intraoperative OCT systems may be combined with direct or indirect ophthalmic viewing systems and allow for both anterior and posterior segment imaging during corneal and vitreoretinal surgeries. The ability to acquire OCT images simultaneously with surgical microscopy visualization overcomes major limitations of intraoperative handheld probes by eliminating the need for frequent pauses

during surgery, allowing surgical microscope guided aiming of the OCT FOV, and enabling imaging of surgical dynamics. In addition, integration with the surgical microscope inherently benefits image stability and reduces sterility considerations. Current implementations include research [20,24,48] and commercial [10,11,74] scan-head modules that attach to conventional ophthalmic surgical microscopes and fully-integrated surgical microscopy platforms (Zeiss RESCAN 700) with built-in OCT scanning and acquisition functionality (Figure 1-3 (a)) [9]

Several clinical studies have validated the advantages of microscope-integrated intraoperative OCT for ophthalmic surgical feedback. A 2011 pilot study evaluated the Cirrus HD-OCT (Carl Zeiss Meditec) in 25 patients undergoing vitreoretinal and cataract surgeries [75]. The results emphasized the ability to monitor morphological changes in real-time and the positive impact this had on influencing surgical decision-making and techniques. In another study, Steven et al. retrospectively analyzed Haag-Streit OCT data from 6 patients undergoing deep anterior lamellar keratoplasty (DALK) [76]. DALK is a technically challenging procedure that requires manual dissection and removal of the corneal epithelium and stroma while maintaining the integrity of Descemet's membrane [77]. Here, Steven et al. showed that intraoperative OCT provides reliable visualization of trephination depth, needle positions, and air injection into the posterior stroma during DALK, which may reduce surgical complexity and failure rates. More recently, a prospective study (DISCOVER) of 227 anterior and posterior segment surgeries showed that intraoperative OCT changed surgical decision-making in 39% of lamellar keratoplasty cases and 19% of membrane peels [60]. The Duke MIOCT research prototype [20] was also clinically evaluated in a study involving 8 patients undergoing surgery for MH, ERM peeling, and vitreomacular traction [78].The results confirmed the ability to observe surgically-induced changes in retinal contour and MH configuration. These observational imaging studies were all performed using SD-OCT engines operating at center wavelengths of 840-880 nm, with 10-30 kHz line-rates, and an axial resolution in tissue of 4-8 μm. While these parameters were sufficient for video-rate cross-sectional imaging, complexities in alignment and co-

localization of the OCT FOV with surgical ROIs, shadowing from surgical instruments, and lack of quantitative image analysis precluded real-time feedback within the standard surgical workflow [60,78,79].

Advances in high-speed swept lasers and high throughput digitizers have increased OCT acquisition rates to between several hundred kilohertz [27,56,80] and over one megahertz [4–6,54] line-rates. Increases in imaging speed combined with parallelized computation using graphics processing units (GPUs) have enabled real-time 3D [54], and more recently, four-dimensional (4D) [24,56] intraoperative OCT (Figure 1-3 (b)). Video-rate volumetric imaging has been demonstrated in preliminary studies and provides enhanced feedback on the depth position of surgical instruments as compared to conventional surgical stereomicroscopy visualization [55,73].

Another area of active research in microscope-integrated intraoperative OCT is dynamic control and co-localization of the OCT field with the surgical ROI using lateral and/or axial tracking. In several commercial and research systems, the OCT FOV may be manually positioned either by the surgeon using foot pedal controls [9,10] or an imaging technician during surgery [24,72]. Tao et al. used an electrically tunable lens (Optotune AG) to provide real-time adjustments of the OCT focus to maintain parfocality with the surgical microscope at different axial positions and zoom levels, and to accommodate for different refractive powers between surgeons [48]. Similarly, the Zeiss RESCAN 700 provides semi-automated axial tracking and focus control to maintain optimal image quality during surgical maneuvers [9].

One of the main motivations for intraoperative OCT is the need to provide real-time depth-resolved feedback at the instrument-tissue interface to better understand correlations between surgical biomechanics and post-operative vision recovery and develop novel surgical techniques to improve surgical outcomes [24,25,48]. Research efforts in this area may be broadly classified as advances in either instrumentation or visualization and feedback.

In one example of advances in instrumentation, Ehlers et al. evaluated the optical properties of semi-transparent materials to develop OCT-compatible surgical instrumentation [71]. Here, results showed ex

vivo imaging of novel surgical pick and needle prototypes with minimal shadowing and refractive artefacts. Another approach called spatial compounding [79] combines novel scanning and image-processing protocols. Acquisition of OCT cross-sections aligned to the trajectory of surgical maneuvers and sparsely spanning the width of surgical instrument tips followed by incoherent averaging minimizes shadowing artefacts by using information from adjacent spatial positions while reducing volumetric sampling density to allow video-rate imaging and display of surgical dynamics.

Ongoing developments in visualization and feedback include heads-up display (HUD) technology that integrate OCT visualization directly into the microscope ocular view [60]. HUDs enable projection of custom information, OCT cross-sections [71] and volume renderings [57], directly onto the surgical field, thus, eliminating the need to look away from the microscope. Using a custom stereoscopic HUD, Carrasco-Zevallos et al. demonstrated the clinical utility of displaying volumetric renderings of four-dimensional (4D) OCT data for real-time surgical feedback (Figure 1-3 (b)) [24] [57]. Recent advances in visualization and feedback combine image-processing algorithms with display hardware to implement augmented reality (AR) or virtual reality (VR) platforms. Li et al. demonstrated segmentation-based methods to overlay depth-information from volumetric OCT data onto the surgical microscope field as additional contrast channels for AR surgical guidance (Figure 1-3 (c)) [27]. Similarly, other groups have demonstrated integration of three-dimensional OCT data with VR platforms [58,59] for applications in surgical feedback and training.

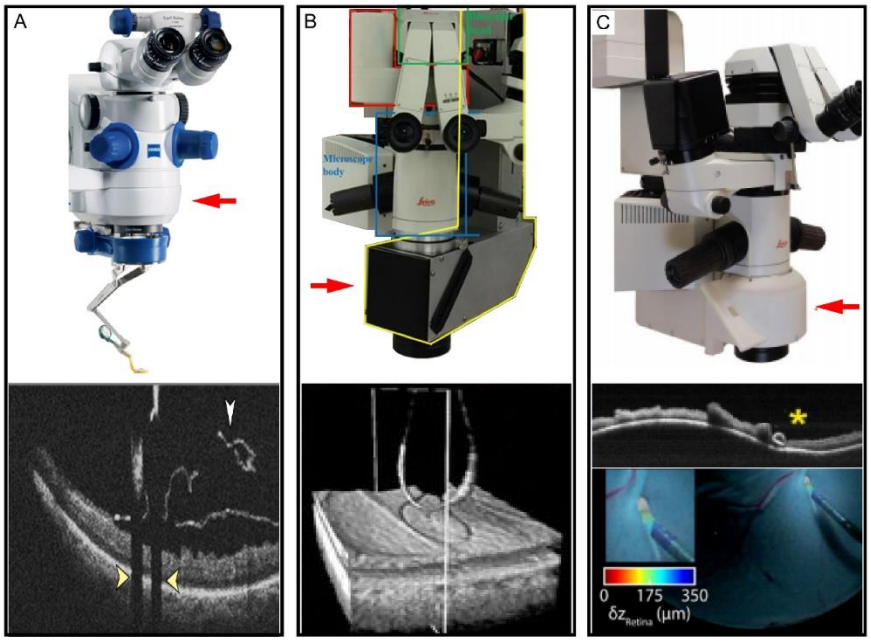

Figure 1-3 - Commercial and research microscope-integrated OCT systemsfor intraoperative ophthalmic imaging with (A) fully-integrated and (B), (C) modular OCT scan-heads (red arrows). (a) Zeiss RESCAN 700 with a representative OCT cross-section during ERM peeling (white arrow) showing shadowing from the instrument body (yellow arrows) [9,60]. (b) Research prototype showing four-dimensional visualization of simulated surgical maneuvers in ex vivo porcine retina [24,57]. (c) Research prototype with a representative OCT cross-section of a diamond-dusted membrane scraper (yellow asterisk) on ex vivo porcine retina and color-encoded overlay of depth information on the corresponding surgical microscope field for augmented reality feedback [27].

1.2.3. Intraocular probes for intraoperative OCT

An alternative approach for ophthalmic surgical guidance is OCT-integrated intraocular instrumentation. These OCT probes are designed to fit through standard trocar systems and are less susceptible to poor image quality as a result of corneal or media opacities as compared to microscope-integrated OCT. Han et al. demonstrated a custom 21-gauge OCT needle probe for vitreoretinal surgery [28]. Two angle-polished gradient-index (GRIN) lenses were counter-rotated for lateral scanning at the image plane. The probe had a working distance of <0.8 mm and retinal images from enucleated porcine eye were acquired with a frame-rate of 0.5 fps. Here, a 1310 nm center wavelength OCT engine was used for better penetration into the choroid and choriocapillaris. Intraocular delivery of OCT avoids absorption losses in the lens and vitreous [81] and provides the flexibility to use longer wavelength light-

sources. In fact, the strong absorption provided additional contrast for visualizing vitreous remnants during surgery. In 2013, Joos and Shen demonstrated a 25-gauge intraocular probe (Figure 1-2 (d)) [26]. The sample arm fiber was housed inside a 34-gauge stainless steel tube with a smooth S-profile and an outer 28-gauge stainless steel tube that was electromagnetically actuated, which resulted in lateral scanning at the tip of the 34-gauge tube. The probe achieved 5 fps frame-rates over a 2 mm FOV at a working distance of 3-4 mm. The system was integrated with a commercial SD-OCT engine (Bioptigen) with 870 nm center wavelength and 4-6 µm axial resolution for ex vivo imaging of porcine cornea and retina. Asami et al. demonstrated a 23-gauge probe design using a rotational scanning mechanism and 100 kHz swept-source OCT engine at 1060 nm [29]. The system acquired OCT cross-sections at 30 fps over a 2.5 mm FOV at 1.5 mm from the probe tip. *In vivo* imaging was demonstrated in 3 patients to obtain real-time images of ERM peeling. Despite advantages in image quality and access to the peripheral retinal, potential limitations of intraocular probes, such as safety and sterilization concerns, imaging stability and hand tremor, may impact their utility in practical settings.

One potentially high-impact application of intraocular probes has been integration of OCT into surgical tools for automated haptic feedback and robotic surgery. Yu et al. combined an intraocular OCT probe [26] with modified vitreoretinal forceps [65] for robotic assistance with a 7 degrees-of-freedom (DoF) tele-manipulator. This was the first study to combine robotic surgery with OCT guidance and the results showed significant reductions in tremor as compared to free-handed operation. An alternative approach integrated an OCT axial distance sensor for closed-loop control of piezo-electric actuated surgical instruments to compensate for surgeon tremor [63,64]. This approach has recently been incorporated into bi-manual tools to actively suppress tremor and assist in ex vivo simulations of complex ophthalmic surgical maneuvers [82,83].

1.3. The clinical problem

A summary of the advantages and disadvantages of the reviewed technologies is presented in (Table 1-2 - Summary of the advantages and limitations of all three approaches for ophthalmic intraoperative OCT).

	Handheld probes	Microscope-integrated scan-heads	Intraocular probes
Advantages	• Portability • Imaging in uncooperative and supine patients	• Imaging concurrent with surgery • No sterilization concerns • Not disruptive to the surgical workflow • Simple control of FOV intraoperatively • Stable imaging platform	• Uninterrupted OCT imaging at the instrument tip • Bypasses optical aberrations from patient's cornea and lens • No shadowing artefacts
Limitations	• Tremor • Surgical pauses, up to 25 minutes • Imaging surgical dynamics is not possible • Sterilization concerns • Lack of registration with the surgical microscope FOV	• Complex alignment of the OCT FOV with the surgical region-of-interest • Shadowing artefacts	• Tremor • Sterilization concerns • Complex scanning mechanisms limit acquisition rates • Limited FOV • Limited clinical validation

Table 1-2 - Summary of the advantages and limitations of all three approaches for ophthalmic intraoperative OCT

Despite the advantages of microscope-integrated OCT for intraoperative guidance, the limitations outlined in (Table 1-2) need to be addressed for broad adoption of the technology.

While 4D MIOCT has indeed provided enhanced visualization of the surgical field, the lack of instrument tracking had two negative implications: 1) trading sampling density for FOV precluded high-

resolution depth-resolved visualization of the surgical dynamics, and 2) manual alignment of the OCT FOV during surgery was still required to co-localize the microscope view of the surgical ROI with that of the OCT.

Chapter 2

2. Automated stereo-vision tracking of surgical instruments for the anterior segment

The following chapter is adapted from M. T. El-Haddad and Y. K. Tao, "Automated stereo vision instrument tracking for intraoperative OCT guided anterior segment ophthalmic surgical maneuvers," Biomed. Opt. Express 6, 3014–3031 (2015).

2.1. Introduction

Intraoperative optical coherence tomography (iOCT) enables cross-sectional imaging of tissue-instrument interactions and surgical dynamics. Over the last decade, various technologies have been developed to aid in intraoperative visualization during ophthalmic surgery, including intraocular fiber probes [26,28] integrated instruments [64], and modified OCT scan-heads [20,84–91]. More recently, surgical microscope-integrated iOCT systems [75,92] have successfully demonstrated real-time OCT imaging concurrent with ophthalmic surgical maneuvers [4,6,93,94]. However, limitations in data acquisition and processing speeds remain critical barriers to real-time volumetric visualization of instrument-tissue interactions and iOCT-guided ophthalmic surgery. Recent developments in swept-source technology have significantly increased imaging speeds over current-generation OCT systems to multi-megahertz line-rates [18-21]. While these novel light sources have demonstrated video-rate volumetric imaging, many remain research prototypes with limited availability and require complex scanning and acquisition systems. Moreover, there remain fundamental trade-offs between imaging speed, optical power incident on the sample, and SNR and between field-of-view (FOV) and sampling density, which are approaching limits of current-generation detector and digitizer bandwidths. Finally, real-time surgical guidance using iOCT requires precision feedback on the three-dimensional position of surgical instruments relative to adjacent tissue microstructures. Despite previous work using complex ray casting and projection

methods to help distinguish subsurface features in volumetric iOCT datasets [95–97], three-dimensional renderings remain difficult to manipulate and interpret in real-time as compared to individual cross-sectional images.

Spatial compounding is a method for cross-sectional visualization of instrument-tissue interactions during surgical maneuvers at video-rates using iOCT [79,98]. A fixed three-dimensional region-of-interest (ROI) is imaged using densely sampled B-scans and sparsely sampled C-scans. Here, the ROI is set such that the B-scan dimension is aligned with the trajectory of the surgical instrument and sparse C-scans span the width of the surgical instrument. Adjacent B-scans are then averaged, which ensures the surgical instrument cross-section is visible as surgical maneuvers are performed within the ROI. This technique provides several advantages, including SNR enhancement and mitigation of shadowing artifacts as a result of averaging, and enables video-rate visualization of surgical dynamics at the modest imaging speeds of current-generation clinical OCT systems (~10-50 kHz line-rate). However, spatial compounding trades-off temporal resolution with FOV, which generally limits video-rate visualization to small ROIs at the tip of surgical instruments. Another limitation is that the spatial compounding FOV must be precisely aligned with the surgical instrument such that the B-scan dimension is parallel to its projected trajectory, which constrains the types of surgical maneuvers able to be imaged and adds additional complexity and delays to standard surgical workflow. While the implementation of heads-up display has aided the alignment and localization of spatial compounding FOVs relative to surgical ROIs [48,71], the potential for iOCT-guided surgery using spatial compounding remains limited.

Real-time visualization of surgical dynamics requires tracking both the orientation and tip position of surgical instruments and using this information to dynamically control the OCT scan-field in real-time. While documentation cameras, which are integrated in all surgical microscopes, may be used to track instrument positions, image processing of live surgical video frames suffers from several drawbacks. Complex image processing algorithms are needed for high-accuracy tracking. These methods are

computationally expensive and trades-off tracking with temporal resolution, therefore, making video-rate operation not readily achievable [99–103]. Several methods for video-rate instrument-tracking using a video feed have been developed specifically for retinal microsurgery and are based off of machine learning and data fusion [26–30]. However, these methods rely on offline training models, which are susceptible to large errors when encountering complex features not included in their training set [79]. As a solution, recent approaches have employed online-learning with a continuously adaptive model [100]. While this has improved performance over previous methods, the tracking accuracy of both approaches remains highly dependent on properties of the video feed and generally achieves 70-90% accuracy at a 15-pixel error threshold [100]. Instrument modifications to increase the contrast of the working-tip may help reduce the computational complexity of tracking algorithms but poses potential safety hazards. For example, placing LEDs at the instrument working-tip in conjunction with wavelength-specific imaging may provide enhanced contrast and easier instrument detection using image processing. However, any modification to conventional surgical instruments raises significant safety concerns, such as alterations to the ergonomics and performance of the instruments, potential sterilization complexities, electrical shock hazards, and chemical and light toxicity. Magnetic tracking methods may cause fewer safety concerns, but are susceptible to noise from ferromagnetic and electromagnetic interference caused by objects placed near the tracking volume, such as surgical instrumentation and clinical monitoring equipment [104].

We propose an alternative approach by tracking the free-tip of the instrument and computing the position of the working-tip using prior information on instrument geometry. This allows for a wider range of instrument modifications by using active or passive markers with minimal safety concerns. A larger FOV needs to be tracked using this approach because small motions at the working-tip will result in a larger range of motions at the free-tip assuming that the instrument is held closer to the working-tip for optimal control and stability. Moreover, the three-dimensional pose of the instrument needs to be unambiguously determined to accurately compute the working-tip position. Similar tracking methods for image-guided

surgery have been previously demonstrated for fMRI and CT [105]. Similarly, a manual OCT-integrated scanning probe has also been reported [106] that implements known computer vision and photogrammetry algorithms for three-dimensional position estimation from two-dimensional images at video-rates [107,108]. However, this system requires large tracking features and imaging distance (51 cm), which are impractical in a surgical setting.

Binocular stereo vision is a well-known method for three-dimensional metrology using computer vision. Information about the mathematical model of a fixed camera-pair setup is used to compute the three-dimensional position of points within the overlapping FOV of two cameras. The main bottleneck in these systems is stereo matching or correspondence, in which pixel locations in an image from one camera have to be mapped to corresponding locations in the image acquired by the second camera to create an accurate disparity map. However, if prior information is available about the scene, then the stereo matching problem can be significantly constrained and reduced to a sorting step, which costs virtually no computational overhead. Here, we implement a stereo vision tracking system using infrared markers and two CMOS area sensors for real-time tracking of the free-tip of surgical instruments. The tracking information is then used to calculate the three-dimensional position of the working-tip, which is used to automatically align the iOCT scan-field. The proposed system is agnostic to the surgical instrument, OCT system, and surgical microscope. This design is suitable for tracking surgical maneuvers in the anterior segment. For posterior segment tracking, the calculated tip positions may need to be offset in proportion to the refractive power and axial length of the eye. This may potentially be resolved by employing methods for measuring the intraocular lens power and the axial length [109,110] and using this information to apply a forward correction of the measured tip positions in real-time.

2.2. Methods

2.2.1. Design specifications

The lateral tracking resolution was determined by the range of working-tip thicknesses for different ophthalmic surgical instruments. The optimal lateral tracking resolution was set at 150 μm to accommodate the diameter of a 40 G instrument such that the instrument tip will be continuously visible in iOCT cross-sections. The orientation resolution (δθ) (Figure 2-1) was set such that a full instrument cross-section was visible across half of each B-scan (Figure 2-2). The tracking update rate was chosen to be at least video rate (~30 Hz) to avoid the instrument moving out of plane in sequential cross-sections and reduce blurring artifacts.

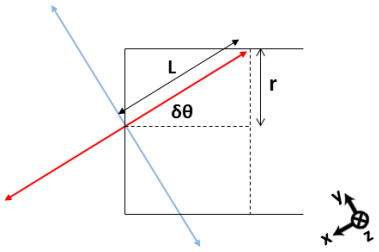

Figure 2-1 - Orientation resolution criterion. Solid black outline is a schematic representation of the *en face* view of an instrument tip with radius r. The red and blue lines represent orthogonal iOCT scan beams with length 2L. For a maximum iOCT scan length of 10 mm and a 40 G instrument tip, δθ is ~0.9°. x-, y-, and z-axes denote B-scan, C-scan, and A-scan directions, respectively.

2.2.2. Binocular stereo vision setup and camera calibration

We implemented a binocular stereo vision system to track active markers at the free-tip of surgical instruments. Binocular stereo vision relies on triangulation to calculate the three-dimensional position of a point based on the disparity in its projection in the image planes of two cameras (Figure 2-3). The FOV overlap between the cameras represents the "stereo field". The stereo vision tracking system was comprised of two CMOS area detectors (PixArt Imaging, Inc.), each with 128 x 96 pixel density and 8X sub-pixel

sampling resulting in a 1024 x 768 pixel image. Each camera had a 40° x 30° FOV and on-board processing, which reported the pixel positions of the 4 brightest points in the image plane.

The stereo vision setup was calibrated using methods described in [38] and Bouguet's camera calibration toolbox for MATLAB [111]. The calibration yields a 3 x 4 matrix of extrinsic parameters,

$$[R \mid t] = \left(\begin{array}{ccc|c} r_{11} & r_{12} & r_{13} & t_x \\ r_{21} & r_{22} & r_{23} & t_y \\ r_{31} & r_{32} & r_{33} & t_z \end{array}\right), \qquad (2\text{-}1)$$

which is used to describe the relative pose between the cameras, and an intrinsic parameter matrix for each camera,

$$A = \begin{pmatrix} S_x & (\tan\theta)S_y & x_o \\ 0 & S_y & y_o \\ 0 & 0 & 1 \end{pmatrix}. \qquad \textbf{(2-2)}$$

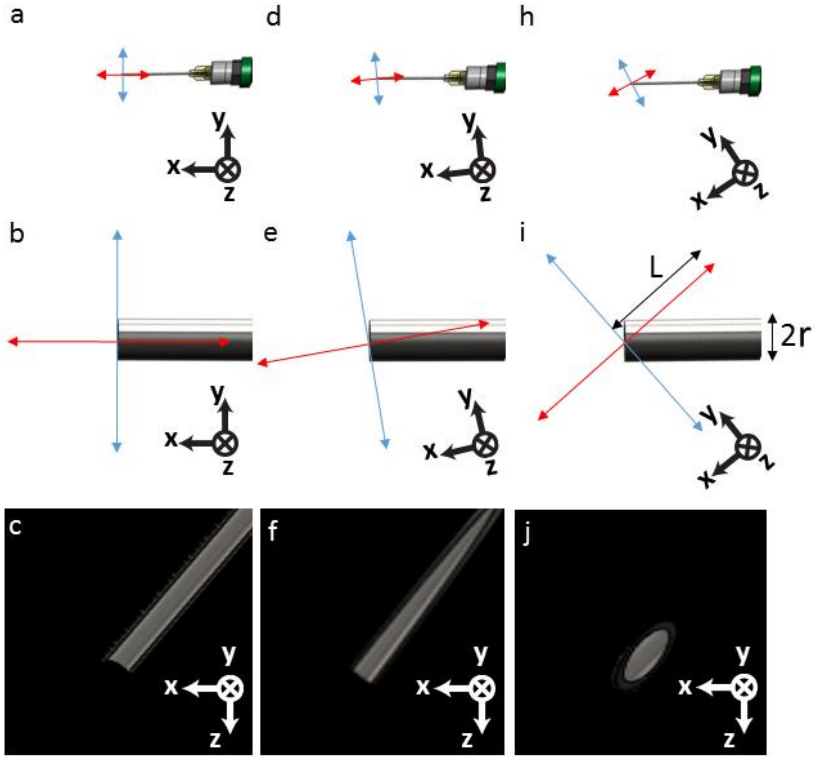

Figure 2-2 - Simulated iOCT cross-sectional images relative to instrument orientation tracking error. (a) *En face* view of the instrument, (b) magnified view of the instrument tip, and (c) simulated iOCT cross-sectional

image along the instrument axis (red line) with no orientation error. (d)-(f) Small orientation error resulting in a slightly rotated iOCT field relative to the instrument, but the entire instrument cross-section remains visible on iOCT. (h)-(j) Large orientation error resulting in a partial instrument cross-section on iOCT. Red and blue lines denote orthogonal iOCT cross-sectional scans and x-, y-, z-axes denote B-scan, C-scan, and A-scan directions, respectively.

Here, Sx and Sy are the x- and y-dimension scaling factors, respectively, and θ is the pixel skew angle. The skew was set to zero in the calibration process for rectangular pixels. x_o and y_o denote the positions of the principal point, which is defined as the intersection of the optical axis of the camera and image plane. The three-dimensional coordinates of a point, M, and its two-dimensional projection in the camera image plane, $m_{L,R}$, are linearly related in homogeneous coordinates by $zm_{L,R} = A[R\ T]M$ [38], where $m_{L,R}$ is defined up to a scalar, z, which is the distance along the optical axis (Figure 2-3 (b)). From this equation, it is immediately clear that using a pair of cameras provides a well-defined system of linear equations, allowing us to compute the three-dimensional position, M, from its projection. Depth resolution in stereo vision, Δz, is directly proportional to the square of the imaging distance and inversely proportional to both the focal length of and separation distance between the cameras, conventionally defined as the baseline,

$$\Delta z = \frac{z^2}{bf}. \quad \textbf{(3)}$$

For a fixed imaging distance and focal length, the baseline can be maximized in order to achieve optimal depth resolution. In our setup, the upper limit of the baseline was set to 100 mm as not exceed the body width of the iOCT system. The cameras were pointed inwards in a converging stereo setup with a tilt that maximized the stereo vision FOV overlap at a desired imaging distance of approximately 19 cm. This imaging distance was set by the axial distance between the bottom of the iOCT chassis and ophthalmic surgical microscope focal plane.

A model square with 4 IR LEDs (center wavelength: 940 nm) separated by 50 mm was used to calibrate the cameras. The model was manually moved in front of the cameras and 1500 frames were captured at different lateral positions and rotations and used to minimize uncertainty in camera parameter estimation.

Information about the model and the captured frames were used by the calibration toolbox to estimate the intrinsic and extrinsic parameters of the stereo system and four orders of lens distortion coefficients in post-processing.

A separate triangulation calibration step was necessary for three-dimensional tracking. Similar to the previous stereo vision calibration, this step only needs to be performed once assuming the relative positions of the stereo vision cameras remain unchanged. First, the pixel coordinates from each camera were normalized using their respective intrinsic parameters (Eq. 2-2) and lens distortion coefficients. Direct triangulation uses the three-dimensional intersect between rays $\vec{m}_L$ and $\vec{m}_R$ to find M (Figure 2-3 (b)) [112]. However, noise in localizing the pixel position of the active marker and errors in the estimated camera parameters may cause the rays to be non-coplanar and nonintersecting (Figure 2-3 (c)). To account for these noise sources, we employed a triangulation method that computed the midpoint of the shortest line segment connecting both rays [113]. In Figure 2-3 (b) and (c), OL and OR denote the optical centers of both cameras. Three-dimensional rays connecting OL and OR to normalized pixel coordinates ML and MR, respectively, are represented in homogenous coordinates as

$$\vec{m}_L = \begin{pmatrix} x_L \\ y_L \\ 1 \end{pmatrix}, \quad \vec{m}_R = \begin{pmatrix} x_R \\ y_R \\ 1 \end{pmatrix}. \qquad \textbf{(2-4)}$$

Using our triangulation method, we can define

$$\begin{aligned} a\vec{m}_L + b\vec{N} - c\vec{m}_R &= \vec{T} \\ \vec{N} &= \vec{m}_L \times \vec{m}_R. \end{aligned} \qquad \textbf{(2-5)}$$

This results in a system of three linear equations with three unknowns (a, b, and c). By applying the intrinsic and extrinsic parameters from the camera calibration, we solve this system of linear equations to calculate the midpoint of the line connecting ML and MR using

$$M_L = O_L + a\vec{m}_L$$
$$M_R = O_R + c\vec{m}_R$$
$$M = \frac{1}{2}(M_L + M_R). \qquad \textbf{(2-6)}$$

The resulting three-dimensional point, M, is our triangulated point.

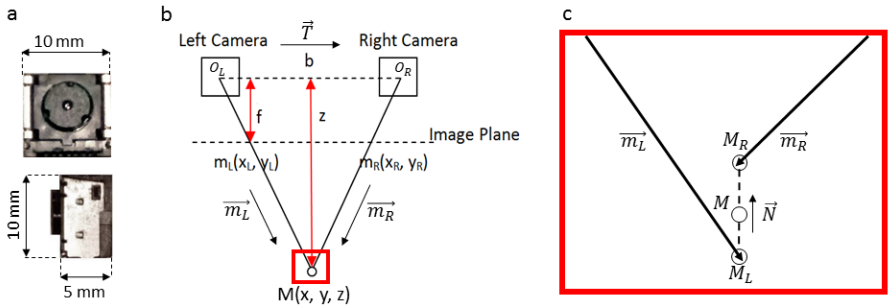

Figure 2-3 - Bionocular stereo vision setup. (a) CMOS area sensor. (b) Stereo vision triangulation with two cameras with optical centers, OL,R; baseline, b; focal length, f; and imaging distance, z. mL.R are projections of M at the camera image plane. c) Stereo vision noise may result in non-coplaner calculated three-dimensional rays. Here, the midpoint between MR and ML is used to approximate the three-dimensional intersect, M.

2.2.3. Camera-to-world coordinate transformation matrix

The three-dimensional positions from the stereo system are computed with respect to the frame of reference of one camera. In our implementation, the left camera was used as the reference. A transformation matrix is then used to convert these coordinates to the desired "world" coordinate system. To compute this transformation, a single IR LED was mounted on a three-axis motorized stage with 25 mm travel in each direction (Thorlabs, MTS25-Z8). The stage was software controlled and moved in preprogrammed trajectories in the x- and y-axes at 200 μm steps over 6 different z planes separated by 4 mm steps. The starting position of the stage was designated as the "world" coordinate origin. 1500 points were triangulated at known stage positions and used to compute the transformation matrix between the camera and "world" coordinate systems. The computed matrix was then applied to all triangulated coordinates to evaluate the triangulation error in "world" coordinates.

2.2.4. Active markers and mathematical model

Three IR LEDs (center wavelength: 940 nm) with 160° beam angle were attached to collars and placed on the instrument body in the arrangement shown in Figure 2-4. The LEDs were used as active stereo vision markers and the three-dimensional positions of all three LEDs were continuously updated at the frame-rate of the camera. The coordinates of the markers were triangulated and used to calculate the working-tip position and orientation of the instrument.

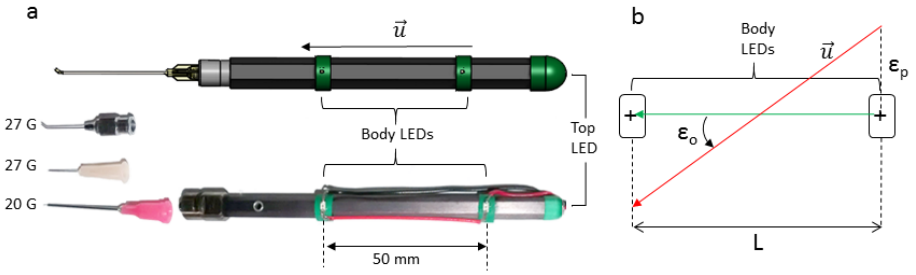

Figure 2-4 - Active stereo vision tracking markers (a) Solidworks model and photo of the instrument with LED active marker collars attached. The instrument body included a Luer lock termination and was used with three detachable tips: 27 G blunt canula, 27 G needle tip, and 20 G silicone soft-tip. (b) Shematic showing computed orientation error (ε_o) based on LED separation distance, L, and triangulation position error (ε_p).

To calculate the working-tip position, a directional vector, $\vec{u}$, which was defined by the two body LEDs. These LEDs were positioned such that $\vec{u}$ would be parallel to instrument axis. The tip was then defined as a point along a vector parallel to $\vec{u}$ that intersected the top LED. The two body LEDs were radially offset from the axis of the instrument and an LED at the free-tip of the instrument was needed to compensate for the thickness of the instrument at each body LED position. Instrument orientation was defined as the angle between $\vec{u}$ and the y-axis of the "world" coordinate.

Triangulation position error of each active marker and the desired orientation resolution determines the separation distance between the body LEDs. Thus, for $\varepsilon_o < \delta\theta$, where $\delta\theta = 0.9°$, and a measured triangulation position error, ε_p, of 150 µm (reported in Results), the minimum LED separation distance, L, would have to be 19.1 mm. To compensate for additional error sources, such as variability in the placement of each LED, a separation distance of approximately 2.5 times the calculated minimum was used (Figure 2-4).

2.2.5. Control of the scanning mirrors drive signal

For optimal cross-sectional visualization of tissue-instrument interactions, we chose to continuously acquire sequential B-scans aligned parallel and perpendicular to the instrument axis and centered at the instrument tip. To maintain an OCT agnostic platform, we relayed conventional sawtooth scanner drive waveforms, generated from our iOCT system, through a DAQ board (National Instruments, PCI-6221) to add voltage and phase offsets calculated from our stereo vision system to track the tip position and orientation of surgical instruments. At the beginning of each imaging session, one second of the drive signal for each galvanometer was sampled at 100 KS/s on two analog channels and stored in internal buffers. Custom software was developed to find the zero-crossings in the stored sampled signals to identify the start of each scan trajectory. For each channel, the corresponding output buffer output contiguous chunks of samples from the stored drive signal corresponding to a single B-scan. The output buffer looped over the stored signal circularly, starting and ending at a zero-crossing to avoid discontinuities in the output signal. The output buffer size was determined based on the selected sampling rate and desired update rate (30 Hz was used), where

$$bufsize_{output} = \frac{\text{sampling rate}}{\text{update rate}}. \quad \textbf{(2-7)}$$

The calculated tip position and orientation of the tracked instrument were translated to the following transformation matrices, which were applied to the output samples,

$$\begin{pmatrix} \hat{X}_i \\ \hat{Y}_i \end{pmatrix} = R \begin{pmatrix} X_i \\ Y_i \end{pmatrix} + \begin{pmatrix} DC_x \\ DC_y \end{pmatrix}. \quad \textbf{(2-8)}$$

Here, $DC_{x,y}$ denoted the position of the tip and R was a 2D rotation matrix defined as

$$R = \begin{pmatrix} \cos\theta & -\sin\theta \\ \sin\theta & \cos\theta \end{pmatrix}. \quad \textbf{(2-9)}$$

The modified output signals were then output to their respective galvanometer scanner drivers such that sequential orthogonal scan trajectories were centered at the tracked instrument tip and oriented parallel and

perpendicular to the instrument axis. A schematic of the stereo vision tracking iOCT system is illustrated in Figure 2-5.

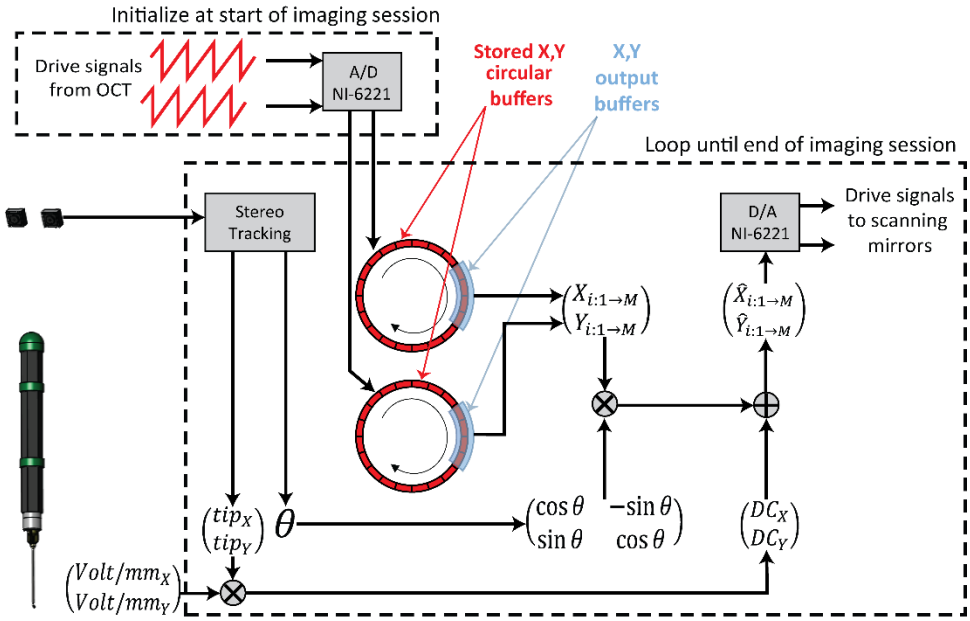

Figure 2-5 - Schematic of stereo vision tracked iOCT. Drive signals from iOCT were sampled for 1 s and stored in circular buffers. Output buffers were continuously read from circular buffers at ~30 Hz. The output samples were rotated and translated by the computed instrument pose from the stereo vision system by applying voltage and phase offsets. Finally, tracked scanner trajectories were output to each corresponding galvanometer scanner.

2.3. Results

2.3.1. Performance of stereo vision setup

The setup described in Section 2.3 was used to assess the lateral resolution error in the stereo vision system. Since the stereo vision system reports measurements relative to the coordinate system of the left camera, a coordinate transformation from the camera coordinate system to that of the three-axis stage was performed. The coordinate transformation consisted of a three-dimensional translation and rotation. The translation vector was computed directly by using the starting position of the stage as the origin. Half of the collected points were used to compute the rotation matrix by $X_{motor} = R \times X_{stereo}$, where Xmotor and

Xstereo were 3-by-M matrices that represented the position of the stage and measured position of the LED, respectively. Here, M represented the number of points collected and R was a 3-by-3 rotation matrix that was the product of rotation matrices about the x-, y-, and z-axis:

$$R_X(\theta)=\begin{pmatrix}1 & 0 & 0\\ 0 & \cos\theta & -\sin\theta\\ 0 & \sin\theta & \cos\theta\end{pmatrix},\quad R_y(\theta)=\begin{pmatrix}\cos\theta & 0 & \sin\theta\\ 0 & 1 & 0\\ -\sin\theta & 0 & \cos\theta\end{pmatrix},\quad R_Z(\theta)=\begin{pmatrix}\cos\theta & -\sin\theta & 0\\ \sin\theta & \cos\theta & 0\\ 0 & 0 & 1\end{pmatrix}$$

$$R=R_X\times R_y\times R_Z. \qquad \textbf{(2-10)}$$

A least squares optimization (Mathworks, Matlab) was used to solve for R. The rotation angles $\begin{pmatrix}\theta_x & \theta_y & \theta_z\end{pmatrix}^T$ were recovered from R using a Rodrigues transform and plotted to verify convergence (Figure 2-6).

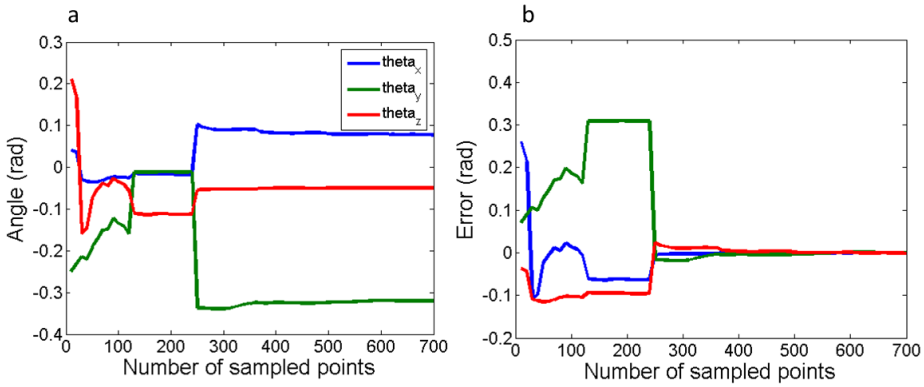

Figure 2-6 - Convergence of coefficients of rotation angles between camera and world coordinates. (a) Calculated rotation angles and (b) error of the calculated angles relative to final converged values.

The rotation matrix converged to the following:

$$R=\begin{pmatrix}0.9726 & 0.0325 & -0.3039\\ -0.0635 & 1.0235 & -0.0540\\ 0.3331 & 0.1006 & 0.9551\end{pmatrix}. \qquad \textbf{(2-11)}$$

Figure 2-7 shows the x-axis trajectory before and after coordinate transformation. The error in the calculated positions relative to those reported by the motor controller is shown in Figure 2-7 (c) and (d). In our stereo vision setup, the lateral resolution was defined as 3 times the standard deviation, which was less than 180 μm for each axis.

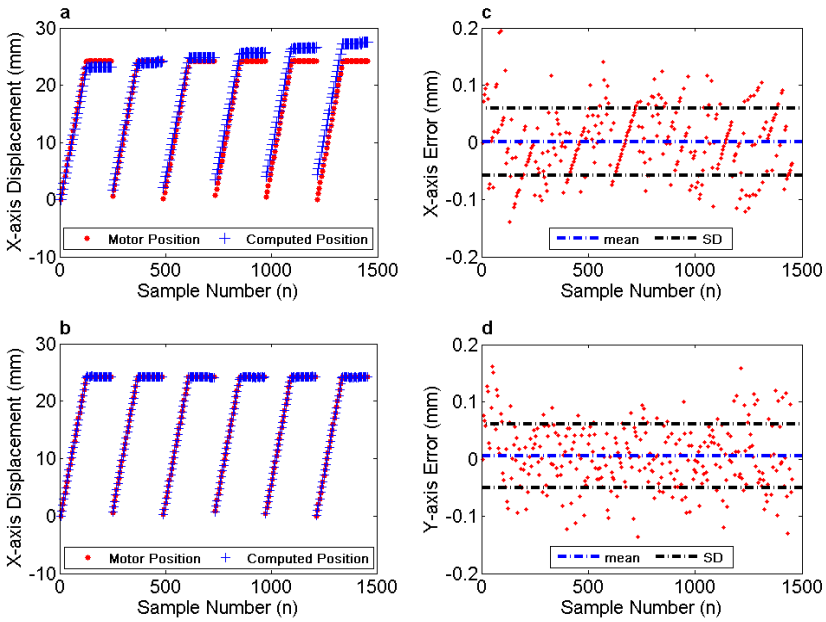

Figure 2-7 - x- and y-axis triangulation error of a single IR LED. The traveled trajectory along the x-axis over 6 z-plans at 4 mm increments (a) before and (b) after coordinate transformation. The flat regions correspond to motion in y-axis only. Similar curves were obtained for y-axis (not shown). Triangulation error in (b) x-axis (mean = 0.001 mm, SD = 0.058 mm) and (d) y-axis (mean = 0.005 mm, SD = 0.055 mm).

To evaluate errors in measured orientation, a surgical instrument modified with active markers was mounted on a rotational stage. The stage was manually rotated through 180^{o} at 10^{o} increments 4 times, twice clockwise and twice counter-clockwise. Measurements from this experiment show that orientation accuracy is well within the desired range (Figure 2-8).

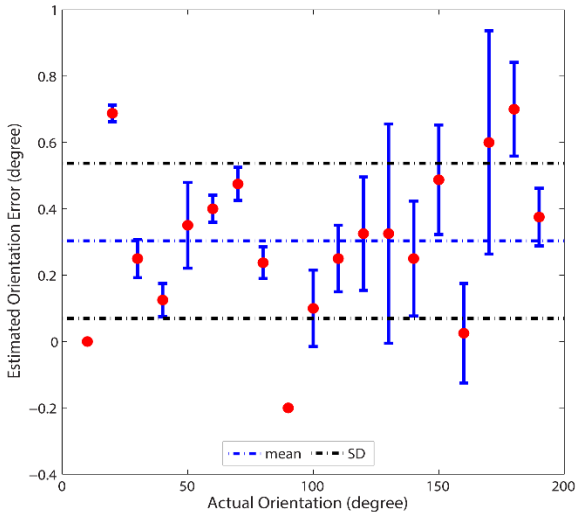

Figure 2-8 - Orientation error measured by manual rotation of a surgical instrument instrument through 180o clockwise and counterclockwise. Mean error = 0.3^o , SD = 0.23^o

2.3.2. Freehand motion error

To assess how tracking errors scaled to the calculated working-tip position during freehand motion, a 0.5 mm mechanical pencil was fitted with LEDs and used in place of the surgical instrument. The tracking system was used to compute the pencil tip as it wrote on paper. The writing was then scanned and compared with the computed tip coordinates to analyze the tracking error. The computed tip trajectory, actual writing, and measured error are shown in Figure 2-9. Two experiments were performed, one using raw calculated tracking coordinates and the other with filtered tracking coordinates. In the filtered version, a moving average filter was used to filter out noise due to pixel jitter introduced by sub-pixel sampling on the camera. Moving average filtering averaged adjacent tracking coordinates and, therefore, reduced the temporal resolution of the tracking system. While the filtered coordinates were smoother than the raw ones, the tracking errors for both experiments were comparable.

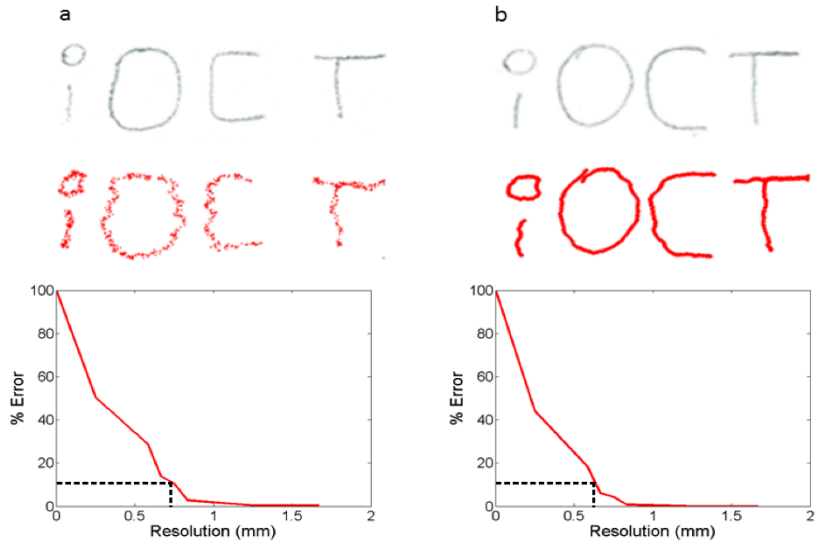

Figure 2-9 - Freehand motion error. Pencil writing (grey) and calculated working-tip coordinates (red) for (a) raw and (b) moving average filtered tracking results. Error plots show relative error between actual and computed positions for different tracking accuracies. Dotted black lines show resolution at 10% error.

Freehand motion was also used to demonstrate automated tracking and control systems running in real-time. A green laser was used as an iOCT aiming beam. A two-axis galvanometer scanner was driven by alternating sawtooth scan trajectories to simulate the cross-hair scan pattern used for subsequent instrument tracking studies. Figure 2-10 shows the iOCT scan-field tracking the mechanical pencil at various positions and orientations.

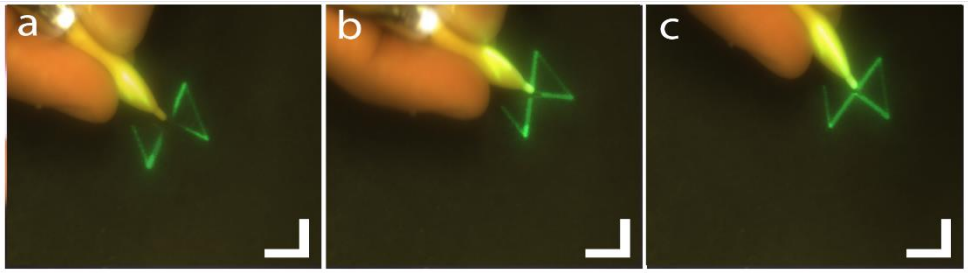

Figure 2-10 - Freehand motion tracking(a) Green laser tracking instrument tip at different (b) positions and (c) orientations. Scale bar: 10 mm.

2.3.3. iOCT integration

We integrated our stereo vision tracking system with our previously described prototype iOCT system [48,71]. The iOCT was programmed to scan a cross-hair pattern with a length of 5 mm sampled with 1024 x 500 pixels (axial x lateral) at 36 kHz line-rate.

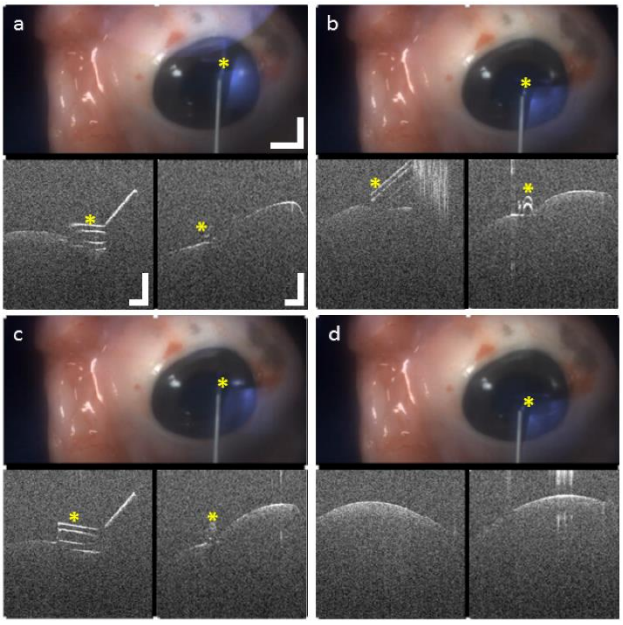

Figure 2-11 - 20 G silicone soft-tip on enucleated porcine eye(a)-(c) Corneal compressions and scraping with the tip visible in both cross-sections. (d) Tip out of field in both cross-sections due to bending of the non-rigid instrument tip. Scale bar: 5 mm, OCT scale bar: 0.5 mm.

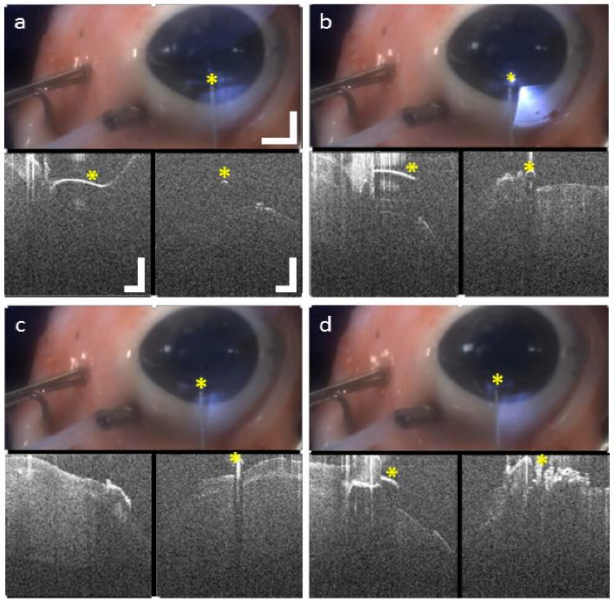

Figure 2-12 - 27 G blunt canula on enucealated porcine eye(a) Scraping corneal surface and (b) near edge of a corneal wound. (c) Instrument out of field in one cross-section due to tracking error. (d) Canula initiates corneal dissection at wound site. Scale bar: 5 mm, OCT scale bar: 0.5 mm.

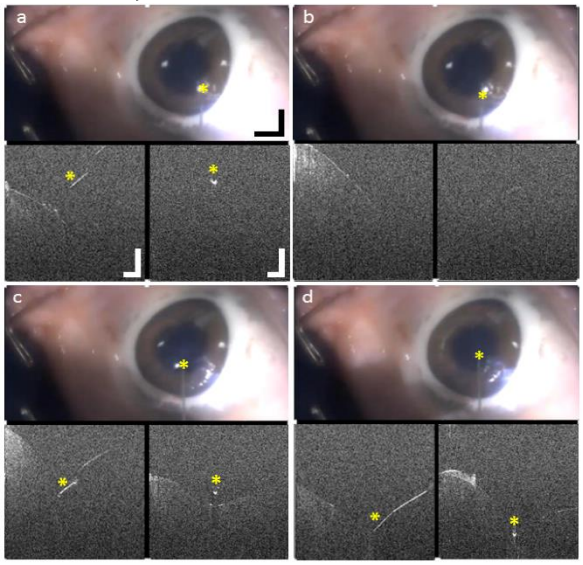

Figure 2-13 - 27 G needle tip on enucleated porcine eye(a) Needle approaching cornea and (b) out of field both cross-sections due to tracking error. (c) Needle starts perforating the cornea and (d) needle visualized inside the cornea after perforation. Scale bar: 5 mm, OCT scale bar: 0.5 mm.

2.4. Discussion

The design considerations for our automated instrument tracking iOCT system were motivated by the need for live visualization of tissue-instrument interactions during ophthalmic surgical maneuvers. The

results from our current proof-of-concept tracking system demonstrate the utility of automated instrument tracking for imaging surgical dynamics by relaxing constraints on both data acquisition speed and volumetric visualization methods. However, additional system enhancements may be made to further improve tracking speed and accuracy for future stereo vision tracking implementations.

2.4.1. Resolution requirements

The tracking resolution of our stereo vision system was described in Section 2.3 and set to accommodate continuous tracking of 40 G ophthalmic surgical instruments with 150 μm tip diameter. Our single LED tracking results showed lateral tracking accuracies of <60 μm (Figure 2-7), thus satisfying our design criterion. However, during tracking of ophthalmic surgical instrument tips under freehand operation, we observed tracking errors of <1 mm for ~90% of tracked frames (Figure 2-9), which only allows for continuous tracking of >21 G instrument tips. When tracking smaller diameter instruments, tracking errors resulted in the instrument moving out of field in OCT cross-sections (Figure 2-12 (c), Figure 2-13 (b)). This discrepancy in tracking accuracy is because any errors in triangulating the positions of body and free-tip LEDs scale when used to calculate working-tip positions. Similarly, the mathematical model used to calculate the working-tip position is another source of position and orientation errors. From the model described in Section 2.4, we see that errors when calculating $\vec{u}$ would result in a directional vector that is not parallel with the instrument axis. This error would then propagate to the calculated working-tip position when projecting the triangulated free-tip LED position by the instrument length along $\vec{u}$. Both of these sources of error may be addressed by increasing the separation distance between body LEDs. However, body LED positions are limited by ergonomic constraints that may differ between surgical instruments and surgeons. An alternative solution would be to explore different mathematical models that relax the collinearity constraint on the body LEDs, which would provide a more robust computational method. Furthermore, a quantitative comparison of different triangulation methods with regard to computational

efficiency and triangulation accuracy, within the context of this tracking problem would also provide better insight into whether a more accurate triangulation algorithm may be employed. Finally, since both of these error sources are limited by the sampling resolution of the stereo vision cameras in our current setup, increasing the pixel density of the cameras would improve triangulation accuracy and allow for a more compact configuration of active markers by decreasing the minimum separation distance required between body LEDs.

The relatively large variance in the calculated orientation error (Figure 2-8) is likely due to repeatability errors of the manually actuated rotation stage used (Thorlabs, PR01 high-precision rotational mount with 5 arcmin resolution). Even so, the error range is well within the design specifications. The non-zero mean in the orientation error measurements is a result of manual alignment errors between the zero degree position of the rotational stage and coordinate system of the tracking system. Since all subsequent orientation changes were calculated as an offset from an arbitrarily set starting position, a non-zero mean orientation error is not attributable to system performance.

Our stereo vision tracking system is designed to calculate the working-tip position based on the assumption that the tip is coaxial with the instrument axis (Section 2.4). Thus, instruments with curved or non-rigid tips are more challenging to track continuously. As shown in the *en face* video frame of Figure 2-11 (d), bending of the flexible silicone soft-tip during corneal compression results in the instrument moving out of frame in the tracked iOCT cross-sections. These tracking challenges may be addressed by integrating image processing of the documentation camera video feed with our stereo vision setup to further refine tracked instrument working-tip positions. Similarly, real-time processing of iOCT cross-sections may provide closed-loop feedback to the tracking system to ensure instruments are always within the iOCT FOV. However, both of these solutions would increase computational overhead and system complexity.

The active markers used in this study were designed to be compact, easy to build, and detachable so that they could accommodate different surgical instrumentation. Moreover, the use of off-the-shelf surface-

mount IR LEDs significantly reduced fabrication costs with the intention of demonstrating an inexpensive and disposable tracking add-on that may be easily integrated into the ophthalmic surgical framework. In our study, the active markers were wired to a power supply, however, the LEDs used were rated at 130 mW (electrical power), which would allow for continuous wireless battery-powered operation for over an hour with a 1000 mAh battery. Similarly, the stereo vision cameras in our setup were battery powered and communicated wirelessly with our computer via Bluetooth. These design considerations demonstrate the potential for simple clinical translation of our tracking technology.

2.4.2. tracking posterior segment surgical maneuvers

Our current stereo vision tracking system was only tested during anterior segment surgical maneuvers. Tracking in the posterior segment is confounded by an additional 4-f imaging relay formed by the optics of the eye and a widefield aspheric ophthalmic lens used to magnify retina features under ophthalmic surgical microscopy. It may be possible to measure the refractive power of the eye and pupil position relative to the iOCT field to compensate for position offsets in the calculated tip position. Alternatively, if image processing of the documentation video feed is integrated with the tracking system (Section 4.1), then the stereo vision system can be used to approximate the instrument tip position, limit the search-space, and reduce the computational complexity of any video feed image processing algorithms used.

2.5. Conclusion

Automated tracking of surgical instruments in microscope-integrated iOCT can provide real-time feedback for image-guided ophthalmic surgery. This may help guide surgery decision-making, enhance clinical outcomes, and enable novel surgical techniques requiring precision access to specific tissue layers and microstructures. We demonstrated a stereo vision instrument tracking implementation that allowed automated tracking of a wide range of surgical instrumentations. Our proof-of-principle system was

agnostic to both the underlying iOCT technology and surgical microscopy system used, which will facilitate integration with commercially available iOCT systems and benefit clinical translation. Our current stereo vision system achieved a lateral tracking resolution that was able to continuously track >21 G surgical instrument tips, but the use of higher pixel density cameras and alternative triangulation algorithms may further improve tracking accuracies. We presented a design for active tracking markers using IR LEDs that allowed for simple and cost-effective fabrication and is disposable, sterilizable, and wireless. Finally, our stereo vision tracking system addressed critical barriers to the development of iOCT-guided surgical maneuvers and may be translatable to applications in microsurgery outside of ophthalmology.

Chapter 3

3. OCT-integrated imaging system for tracking in the posterior and anterior segment

Parts of the following chapter appear in J. D. Malone, M. T. El-Haddad, I. Bozic, L. A. Tye, L. Majeau, N. Godbout, A. M. Rollins, C. Boudoux, K. M. Joos, S. N. Patel, and Y. K. Tao, "Simultaneous multimodal ophthalmic imaging using swept-source spectrally encoded scanning laser ophthalmoscopy and optical coherence tomography," Biomed. Opt. Express 8, 193–206 (2017).

To the address the limitations of our previous design, three main system modifications were needed: 1) extended OCT imaging depth, 2) co-registration between the tracking and the OCT FOVs through a shared optical design, and 3) accommodation of a wider range of instrument geometries likely requires an *en face* view of the surgical FOV. Therefore, a direct application of our stereo vision tracking system to retinal surgery was not feasible. Additionally, as described earlier, processing of the documentation camera video feed is confounded by illumination variability. This is particularly significant in retinal microsurgery where intraocular endo-illumination is not uniform and, thus, visibility of registration fiducials may change dynamically.

We performed two preliminary studies: 1) extended imaging depth SD-OCT with axial tracking and visualization of up to 6.4 mm in depth, and 2) a multimodal Spectrally-Encoded Scanning Laser Ophthalmoscopy (SESLO) and SS-OCT system (SS-SESLO-OCT) for simultaneous *en face* and cross-sectional imaging. We concluded that a high-speed SS-SESLO-OCT system may address all the limitations described here. Moreover, the use of SS-OCT enabled higher spectral sampling density and provided a longer imaging range compared to SD-OCT, which may eliminate the need for axial tracking.

In the first part of this aim, we propose a wide-field, high-speed SS-SESLO-OCT system design for intraoperative imaging and instrument tracking. In the second part, we will design a microscope-integrated scan-head for SS-SESLO-OCT to demonstrate the feasibility of intraoperative translation.

3.1. Depth-extended SD-OCT

Several OCT systems with dynamically controlled reference arm position have been developed to compensate for the relative axial motion in the sample arm during imaging [62,64,114]. Information about axial motion is obtained from processing of A- or B-scans and is used in a closed-loop control system to dynamically set the optical path-length of the reference arm. This has been achieved with scanning galvanometer mirrors in Fourier-domain optical delay lines (FDODLs) [115,116], or motorized linear-translation stages in time-domain optical delay lines (TDODLs). In FDODL, the reference beam is dispersed and focused on a scanning mirror that acts as a voltage controlled phase ramp in the Fourier domain [115], which maps to path-length delays in the spatial domain. FDODLs typically possess sub-millisecond step-response time compared to few tens of milliseconds in TDODLs, but provide a smaller axial range.

3.1.1. System design

We built an OCT system with dynamic depth-ranging reference arm that utilized a combined FDODL and TDODL design for depth-tracked OCT imaging during surgery. This design provided >100 mm of controllable path-length delay, making the system potentially suitable for applications outside ophthalmology. Tracking was done based on real-time image processing of the acquired B-scans, giving high resolution feedback for the control loop. Custom software was developed to display an extended imaging range of 6.4 mm in depth, to provide enhanced visualization of local and global deformations in

compressive motions. The depth-tracking system was integrated with our lateral instrument-tracking system from aim 1 to demonstrate the feasibility of automated 3D tracking and control of the OCT FOV.

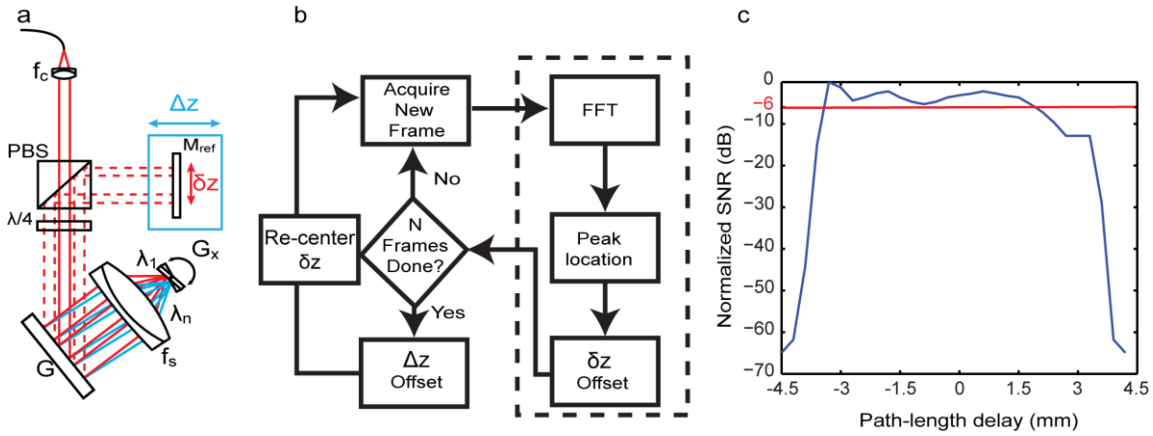

Figure 3-1 - Dynamic-delay reference arm(a) Schematic of the optical setup. Collimated light from the source is dispersed at the diffraction grating and focused by the scan lens onto the face of the galvanometer. Tilting the galvanometer is equivalent to applying a phase ramp in the Fourier domain resulting in a path-length delay in the spatial domain. Reflected light from the galvanometer is re-collimated after the grating. The polatization optics along with Mref allow the excursion to be double-passed, which results in amplifying the effected delay from a single scan angle. Mref is mounted on a motorized stage that provides extra time-domain delay. f: collimating and scan lenses; PBS: polarizing beam splitter; $\lambda/4$: quarter-wave plate; G: 300 lpmm reflective grating; Gx: scanning galvanometer mirror; Mref: reference mirror; Δz, δz: Path-length delays from TDODL and FDODL, (b) depth tracking and control algorithm, Each B-scan is processed to track the peak intensity in the central 35% A-scans and actuate the reference arm accordingly. N was set such that δz was re-centered every second. (c) SNR falloff with FDODL shifts showing a 6-dB range of

Our depth ranging system consisted of a reference arm with a galvanometer based FDODL [115,116]. The optical path-length delay due to the FDODL is proportional to the galvanometer scan angle according to the following relation,

$$\Delta l_g \ \alpha \ \frac{4\sigma l_f \lambda_o}{p}, \tag{17}$$

where l_g is the path-length delay, σ is the scan angle of the galvanometer, l_f is the focal length of collimating lens, λ_o is the center wavelength of the light source, and p is the grating pitch (Figure 3-1). The diffraction grating used had a line density of 300 lpmm (GR25-0608, Thorlabs). The focal length of the scan lens was 80 mm (AC504-080-B, Thorlabs). The SD- OCT imaging system used an SLD light source centered at 870 nm (M-T-HP, Superlum Broadlighters) with 150 nm bandwidth, and the line scan camera

(spL4096-140km, Basler AG) allowed A-scans acquisition with 1024-pixel density at 125 kHz. The galvanometer used (6210H, Cambridge Technology) had a 0.1 ms small-angle step-response. The scan range was ultimately limited by the one-inch polarization optics, which yielded a range of 5.2 mm for the optical path-length delay (Figure 3-1 (a),(c)). The reference mirror (Mref) was mounted on a DC motorized moving stage (DDSM100, Thorlabs Inc.) which had a 100 mm travel range at up to 500 mm/s and acted as a TDODL.

Axial displacements were estimated based on image processing of the acquired B-scans. The central 35% A-scans in each B-scan were averaged, and an error was computed as the difference between the calculated peak location and its desired location within the B-scan. The error measurement was then used as a feedback signal to the control software, which generated a proportional signal to the FDODL to compensate for the measured error. A hand-off between the FDODL and the TDODL occurs over one-second intervals, allowing the FDODL to re-center (Figure 3-1 (b)). This was done to compliment the tracking range of the FDODL and maintain continuous availability of the full FDODL rapid delay range. Custom software was developed to provide an extended-depth B-scan display.

The depth tracking system was integrated with our lateral tracking system. The lateral tracking system maintained a 0.8 mm resolution in 90% of the acquired frames. Three-dimensional tracking with OCT was demonstrated on a cornea phantom to show its utility for image-guided surgery.

3.1.2. Ex vivo evaluation

Three-dimensional tracking was demonstrated on a cornea phantom with lateral and compressive motions (Figure 3-2). The tracking system maintained the instrument tip in field both laterally and in depth. Since depth-tracking stabilizes the sample within the axial FOV of the OCT, only local tissue deformations were visualized. Custom software was developed to show a 6.4 mm extended display which provided enhanced visualization of the global deformations over the surface of the phantom, 4x the original display

range (Figure 3-2 (d),(e)). Tracking resolution was set by the 5 µm axial resolution of the OCT system. The control system bandwidth was ultimately limited by the processing speed of the B-scans. Each B-scan contained 512 A-scans that were acquired at 125 kHz. However, processing, display, and actuation were done at 12 Hz. Additionally, there was a 2-frame lag between calculating the error signal and actuating the reference arm, accounting for a <84 ms latency in the tracking system. Both the system bandwidth and the latency can be enhanced by using multi-core or GPU processing.

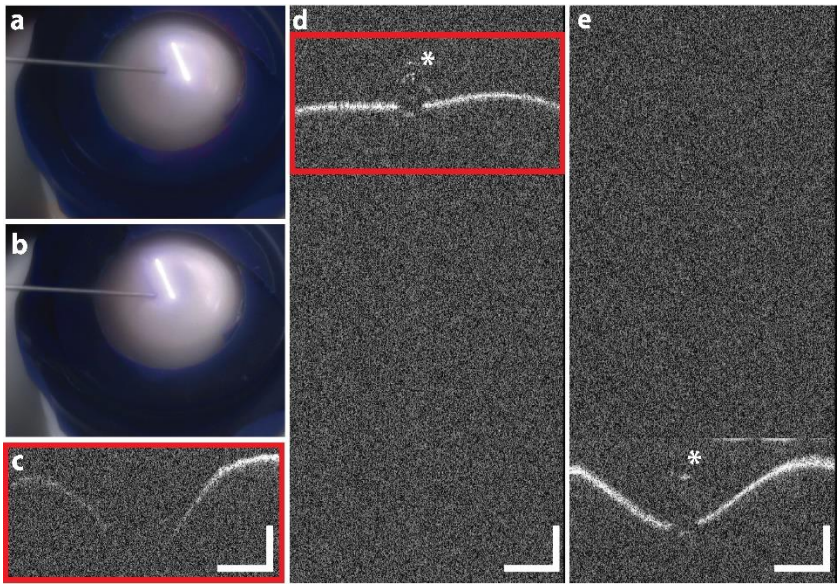

Figure 3-2 - Three-dimensional trackingwith a silicone soft-tip on a cornea phantom (a) small and (b) large compressions at different lateral positions, (c) actual axial FOV of the OCT system without depth-tracking, (d) and (e) 4x-extended OCT display with depth tracking corresponding to video frames (a) and (b), respectively. The asterisks point to the instrument tip, and the red rectangle provides a visual comparison between the actual and the extend OCT FOV. Scale bars: 0.5 mm

3.1.3. Conclusion

A dynamic-delay reference arm may be useful in the intraoperative ophthalmic surgical guidance. The use of a FDODL allows for fast, high-resolution tracking over a few millimeters. Incorporating a TDODL allows for arbitrarily long range imaging depth. This dynamic reference arm design can be integrated into a 3D instrument tracking system for automated real-time visualization of surgical maneuvers. However, the use of a dispersive element and polarization optics require a mechanically-stable environment.

3.2. Simultaneous SESLO and OCT imaging

SLO is a high-resolution *en face* imaging technology that has conventionally been implemented using confocal point-scanning [117] or quasi-confocal line-scanning [118] systems and has advantages of increased contrast and rejection of out-of-focus artefacts as compared to conventional widefield fundus photography. Recently, spectrally-encoded imaging methods [119] were used to implement a spectrally-encoded confocal scanning laser ophthalmoscope (SECSLO) [120] that was then integrated with a spectral domain OCT system for multimodal serial acquisition of *en face* SLO and cross-sectional OCT fundus images for image guidance, registration, and removal of motion artefacts [121]. However, spectrally-encoded imaging suffers from speckle noise because each spectrally-encoded channel is effectively monochromatic. In this study, we demonstrate retinal imaging using a swept-source spectrally-encoded scanning laser ophthalmoscope and OCT (SS-SESLO-OCT) at 1060 nm. SESLO illumination and detection were performed using the single-mode core and multimode inner cladding of a double clad fiber coupler, respectively, to preserve lateral resolution while improving collection efficiency and reducing speckle contrast at the expense of confocality [122,123].

3.2.1. System design

Multimodal SS-SESLO-OCT (Figure 3-3) was implemented using a shared 100 kHz swept-source centered at 1060 nm with 100 nm bandwidth (SSOCT-1060, Axsun Technologies). The source was split using a 70:30 coupler, and the 30% output was coupled to a single-mode patch cable fusion spliced to the double clad fiber input of a double clad fiber coupler (DCFC, Castor Optics) and used as the illumination for the SESLO imaging arm. The SESLO illumination was collimated and dispersed using a 1200 lpmm transmissive grating (Wasatch Photonics) to achieve a maximum of 1616 resolvable points along the spectrally-encoded imaging axis. The 70% output from the source was split using an 80:20 coupler between the transmissive reference and sample arms of an ophthalmic OCT system, respectively. The sample arm

of the OCT was collimated, scanned with the slow axis galvanometer scanner and combined with the SESLO optical path at an intermediate image plane using a D-shaped pick-off mirror (Thorlabs). The combined SESLO-OCT path was then relayed to a second galvanometer scanner (OCT fast axis and SESLO scan axis) and a ~0.9x scan-ophthalmic lens relay, and imaged on to the retina. The pick-off mirror was used to ensure optimal light throughput of both imaging modalities. The mirror was coated to within 50 µm of the substrate edge, which set the separation between SESLO and OCT paths, which was further reduced to ~25 µm on the retina by a 0.45x relay. SESLO backscattering was relayed through 0.5 m of multimode fiber (~ 8000 modes, 89x speckle contrast reduction expected) and detected using a free-space InGaAs amplified photodetector (FPD510-F, MenloSystems) and 37 dB amplifier (ACA-2, Becker & Hickl). The OCT was detected using a fiber-coupled InGaAs balanced amplified photodetector (PDB481C-AC, Thorlabs), and both SESLO and OCT signals were digitized simultaneously on a dual channel 1.8 GS/s ADC (ATS9360, AlazarTech). A laser-provided linear-in-k clock was used as the digitizer sampling clock and had a 6-dB imaging range of 3.7 mm. Custom software performed real-time data acquisition, processing, display, and archiving. Image post-processing was performed using Matlab (Mathworks) and ImageJ (NIH).

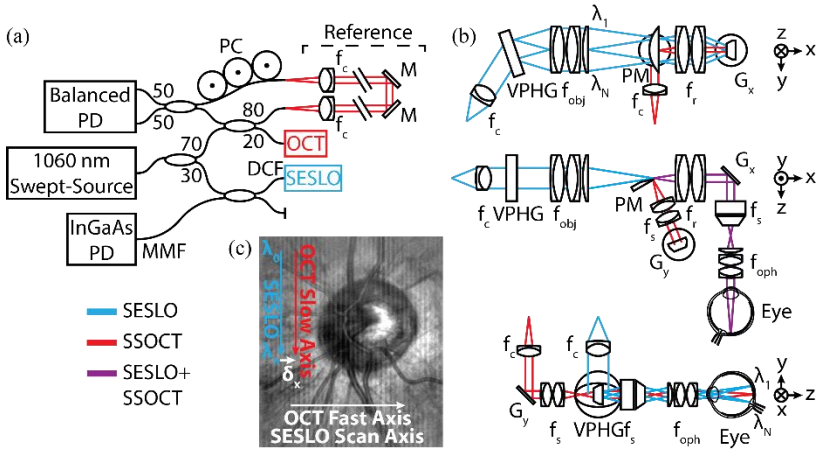

Figure 3-3 - SS-SESLO-OCT engine and imaging optics schematics(a) A 1060 nm swept-source is shared between the SESLO and OCT via a 30:70 coupler, respectively. SESLO illumination is relayed by the single-mode core and detected by the multimode inner cladding of a prototype DCFC. (b) Cross-sectional views of the imaging optics (SESLO, blue; OCT, red; shared, purple). SESLO and OCT optical paths share a scanning mirror (Gx, SESLO scan axis and OCT fast axis) and are combined using a pick-off mirror. (c) Representative

***in vivo* retinal SESLO image centered on the optic nerve showing: SESLO encoded, SESLO scan, OCT fast, and OCT slow axes. The SESLO and OCT FOVs are offset in the fast axis by ~25 µm at the retina (δx). DCF, double-clad fiber; f, collimating, objective, ophthalmic, relay, and scan lenses; Gx,y, galvanometer scanners; M, mirror; MMF, multimode fiber; PC, polarization controller; PD, photodiode; PM, D-shaped pickoff mirror; VPHG, grating.**

3.2.2. Comparison of SECSLO and SESLO imaging performance

SECSLO and SESLO images of a scattering phantom were compared to verify lateral resolution is preserved in SESLO despite using multimode collection through the inner cladding of a DCF. A USAF 1951 resolution test chart was imaged through a uniformly scattering layer at the focal plane of the shared scan lens (fs in Figure 3-3 (b)) to quantify lateral resolution performance (Fig. 19). A single-mode optical circulator was inserted between the SESLO arm of the 70:30 coupler and DCFC to enable SECSLO (Figure 3-4 (a), (b)) and SESLO (Figure 3-4 (c),(d)) imaging of the same resolution phantom. As expected, we observed a >3.5x increase in collection efficiency through the DCF as a result of an increased NA (DCF core: 0.14; DCF inner cladding: 0.2) and diameter (DCF core: 4 µm; DCF inner cladding: 105 µm). However, when comparing lateral resolution both SECSLO (Figure 3-4 (b), arrows) and SESLO (Figure 3-4 (d), arrows) were able to resolve identical elements.

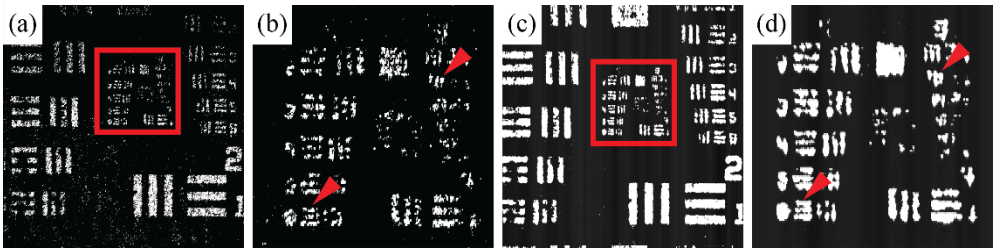

Figure 3-4 - Comparison of SECSLO and SESLO imaging performance. Images of USAF 1951 test chart through a uniformly scattering layer acquired using (a), (b) a single-mode optical circulator and (c), (d) a DCFC show identical smallest resolvable elements (horizontal: Group 5 Element 6, 8.77 µm; vertical: Group 6 Element 2, 6.96 µm). Images were acquired at the focal plane of the final scan lens (fs in Figure 3-3 (b)). Anisotropic lateral resolution is a result of dominant chromatic aberration in the vertical (spectrally-encoded) dimension.

3.2.3. Speckle contrast reduction

Using the SECSLO and SESLO setup, we imaged a uniformly scattering layer to quantify speckle contrast reduction when using multimode collection. In addition to the single-mode circulator and DCF configurations, we also inserted a 250 m MMF patch cord between the DCFC MMF output and SESLO detection photodiode to increase modal dispersion for additional speckle contrast reduction [122]. Speckle contrast was calculated as the ratio of the standard deviation of the intensity to the mean. Any contribution from additional noise sources (electronic, detector, RIN, etc.) was removed by calculating speckle contrast on 30-frame averaged scattering data. We do not expect any significant reduction in speckle contrast as a result of frame averaging because the solid scattering phantom imaged produced static speckle patterns. Multimode collection (DCFC) reduced speckle contrast by 3.68x as compared to single-mode (SMF). By increasing the number of propagating modes and modal dispersion using a MMF patch cord, speckle reduction was increased to 5.37x.

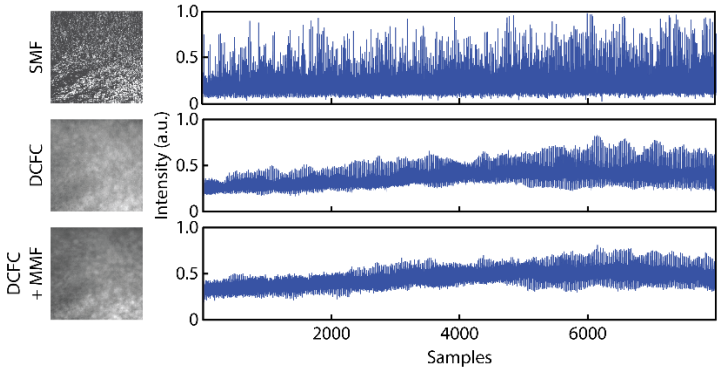

Figure 3-5 - SESLO speckle reduction using multimode collection *En face* image and corresponding intensity profiles of a uniformly scattering phantom imaged using single-mode illumination and collection through an optical circulator (SMF), single-mode illumination and multimode collection through a DCFC, and single-mode illumination and multimode collection through a double-clad fiber coupler and a 250 m multimode patch cord (DCFC + MMF).

3.2.4. *In vivo* imaging

In vivo human retinal imaging (Figure 3-6) shows the central 10o SS-SESLO-OCT field-of-view (FOV) at the optic nerve sampled at 1376 x 500 x 500 pix. (spectral x lateral x lateral). Raw SESLO frames (Figure

3-6 a)) and OCT cross-sections (Figure 3-6 (d)) were acquired at 200 frames-per-second. SESLO images were bandpass filtered to remove residual laser sweep modulation and detector noise, and two-dimensional rigid body registration was performed (DFT registration) [10] prior to averaging (Figure 3-6 (b)). *En face* projection of OCT data (Figure 3-6 (c)) shows overlapping FOV, higher contrast and resolution as a result of confocal detection, depth-resolved features, and more motion artefacts (asterisks and slow scanning axis, Figure 3-6 (e)) as compared to SESLO.

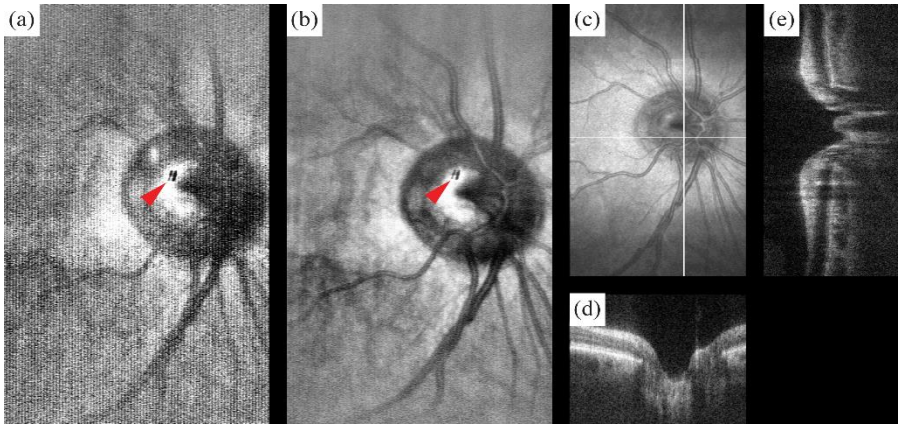

Figure 3-6 - *In vivo* SS-SESLO-OCT human retinal imaging . (a) Raw SESLO sampled with 1376 (spectral) x 500 pix. acquired at 200 fps and (b) 5-frame average (see Visualization 1). (c) Inherently co-registered volumetric OCT dataset with representative (d) fast and (e) slow axis cross-sectional images. (d) B-scans were acquired simultaneously with each SESLO frame. OCT volume was sampled with 1376 x 500 x 500 pix. (spectral x A-scan x B-scan) with a total acquisition time of 2.5 s. Arrow, specular reflection artifact.

3.2.5. Conclusion

SS-SESLO-OCT is a novel method for multimodal ophthalmic imaging. Our system design is compact and uses a shared light source, imaging optics, and digitizer, which reduces overall system complexity, ensures inherent spatio-temporal co-registration between SESLO and OCT FOVs, and facilitates clinical translation. *En face* SESLO images acquired concurrently with OCT cross-sections enable lateral motion tracking and three-dimensional volume registration with broad applications in intraoperative instrument tracking, multivolume OCT averaging, image mosaicking, and widefield angiography.

The uniformly-illuminated SESLO FOV addresses one of the main challenges for intraoperative retinal imaging for surgical instrument tracking. We believe this may enable faster and more reliable processing using computer vision-based algorithms. Additionally, SS-OCT provided an imaigng range of >3.7 mm. This can be extended by using a faster k-clock which may eliminate the need for complex reference arm designs and axial tracking algorithms.

Chapter 4

4. Spectrally Encoded Coherence Tomography and Reflectometry (SECTR): simultaneous *en face* and cross-sectional imaging at 2 gigapixels-per-second

The following chapter is adapted from M. T. El-Haddad, I. Bozic, and Y. K. Tao, "Spectrally encoded coherence tomography and reflectometry: Simultaneous *en face* and cross-sectional imaging at 2 gigapixels per second," J. Biophotonics 11, e201700268 (2018).

4.1. Introduction

Non-invasive biological imaging is crucial for understanding *in vivo* structure and function. Optical coherence tomography (OCT) and reflectance confocal microscopy (RCM) are two of the most widely used optical modalities for exogenous contrast-free high-resolution three-dimensional imaging in non-fluorescent scattering tissues. OCT utilizes low-coherence interferometry to reject of out-of-focus light and measure depth-resolved backscattering profiles [1]. The high sensitivity and use of multiplexed detection in current-generation OCT [49–51,124] enable high-speed raster-scanned imaging with priority cross-sections acquired at several hundreds to thousands of frames-per-second (fps) and three-dimensional tomograms acquired at tens of volumes-per-second [5,24,53,54]. RCM provides high-contrast *en face* images of sample backscattering at up to 30 fps [125,126]. Whereas spectrally multiplexed detection in OCT allows simultaneous acquisition of all scatterer reflectivities in depth, tomographic imaging in RCM is achieved by serially stepping the focal plane with a minimum axial slice thickness determined by the confocal parameter [127]. Coherence-gated rejection of multiply scattered light and the high detection sensitivity of OCT also provide advantages for deep tissue imaging with up to 1-2 mm of penetration depth in densely scattering tissues [128] as compared to <300 μm in RCM [128–131]. However, despite the aforementioned advantages of OCT, RCM plays an important role in applications requiring high frame-rate *en face* imaging with minimal computational overhead, or in applications where subcellular imaging resolution is more favorable than penetration

depth [128,132–134]. Additionally, while the superior contrast of fluorescence confocal microscopy has led to its broad adoption in basic sciences [135], the ability of RCM to resolve cellular and subcellular tissue structures without the need for exogenous contrast has made the modality uniquely suited for *in vivo* clinical diagnostic imaging [136,137].

Sample motion during *in vivo* imaging can significantly degrade image quality and fidelity. During volumetric acquisition, motion artifacts result in inaccurate three-dimensional reconstruction and limit the accuracy of quantitative data analysis. Higher imaging speeds reduce the effects of motion-induced artifacts, but suffer from inherent tradeoffs in signal-to-noise ratio (SNR), sampling density, and field-of-view (FOV). OCT systems with multi-MHz line-rates enable acquisition of densely sampled volumes over large FOVs [5,54,138]. However, at these line-rates, sufficiently high bandwidth spectral digitization is only achievable using broadband oscilloscopes, which precludes real-time image-processing and display.

Computational methods for volumetric motion correction that optimize a global error function over several serially acquired datasets have been previously published [139–142]. While this approach has been shown to remove motion artifacts in OCT volumes, it requires repeated volumetric sampling with orthogonal scan trajectories, the accuracy of the results depends on the number of repeated volumes, and use of overlapping mutual information results in a composite motion-corrected dataset that may not accurately represent the anatomic dimensions of the sample [139]. Thus, there remains a need for robust methods for post-acquisition sample motion correction. A recent approach demonstrated motion-corrected OCT using Lissajous scanning patterns that provided smooth, inherently overlapping trajectories [143]. While this eliminated the need for repeated orthogonal acquisitions, the requisite scanning protocol precluded real-time visualization of the acquired data and limited the utility for functional OCT extensions such as OCT angiography.

Other published approaches for motion-tracking and correction combine complementary spatial information from multiple imaging modalities for motion estimation and compensation. While combined OCT-RCM has been demonstrated for retinal imaging and motion-correction in post-

processing [70], the video frame-rates of traditional RCM systems preclude imaging and tracking of high-speed sample motion and dynamics. Higher speed RCM can achieve several hundred frames-per-second imaging rates by using spinning disc or polygonal scanners [144–146]. However, these systems trade off FOV and sampling density and require bulky optics and complex scanning mechanisms, which are poorly suited for clinical translation.

Spectrally-encoded confocal microscopy (SECM) [119,147,148] addresses several key limitations of traditional RCM by parallel detection of sample backscattering using line-illumination. Wavelength-multiplexing lateral positions enables wide-field imaging at high frame-rates through simple fiber-optic based systems. Combined OCT-SECM has been demonstrated for volumetric co-registration using complementary *en face* and cross-sectional images for real-time *in vivo* aiming, and post-acquisition sample motion-tracking and compensation [120,149]. These previous-generation systems were limited by illumination and detection complexity, often requiring multiple light-sources and digitizers, each dedicated to one modality, or free-space bulk-optics spectrometers. Most importantly, SECM image quality was degraded by speckle noise as a result of interference effects from dense scatterers within each monochromatic spectrally-encoded focal volume.

We present spectrally-encoded coherence tomography and reflectometry (SECTR), a novel high-speed multimodal imaging system for simultaneous *en face* and cross-sectional imaging that overcomes limitations of traditional OCT-RCM. Spectrally-encoded reflectometry (SER) uses partially-coherent detection through a double-clad fiber (DCF) [122,150,151] to increase collection efficiency and reduce speckle-noise contrast at the expense of axial resolution as compared to conventional RCM. In addition, the DCF allows for single-mode illumination and multimode detection, which extends the confocal parameter without sacrificing lateral resolution [149]. Reflectance imaging using a large depth-of-focus is particularly advantageous for motion-tracking because it axially compounds different features from multiple depths into a single *en face* frame for image registration. However, while DCFs have been utilized in both fluorescence and reflectance imaging applications [122,123,152–154], the benefits of DCF in applications with strict low-incident-power

limits, such as ophthalmic imaging, have been limited because inner-clad back-coupling of end-face reflections results in a large background signal, thereby reducing the available detection dynamic range and SNR [149,155,156]. In SECTR, we introduce a novel fiber termination scheme that mitigates end-face reflections by more than an order-of-magnitude, enabling direct-detection of *en face* sample scattering through a DCF.

We also reduce the system complexity of previously described multimodality imaging systems to benefit translation of our technology for research, commercial, and clinical applications. In SECTR, OCT and SER share a swept-laser source, a scan mirror, a digitizer, imaging optics, and triggering and clocking electronics. The resulting system allows for multimodality imaging of inherently spatiotemporally co-registered fields with a net throughput of 2 gigapixels-/4 gigabytes-per-second. High-speed volumetric OCT provides depth-resolved micron-resolution visualization of subsurface features-of-interest with high SNR, whereas complementary *en face* SER provides anatomical landmarks that enables aiming, sample positioning, motion-tracking, and multi-volumetric mosaicking of ultrawide-field datasets.

As a proof-of-concept, we combined SECTR with imaging optics optimized for wide-field imaging in the posterior retina and anterior chamber of the human eye. *In vivo* ophthalmic imaging allows for comprehensive assessment of imaging system performance and utility because 1) incident light levels are limited by established maximum permissible exposure (MPE) standards and, thus, requires high imaging dynamic range and SNR; 2) the fast dynamics of micro-saccadic eye movements, which are on the order of 100-200 Hz [157], may be used to evaluate the temporal resolution and spatial accuracy of SER motion-tracking; and 3) OCT is a well-established ophthalmic imaging technology with broad applications in diagnostics and therapeutic guidance. At the maximum sampling rate, 5 megapixel *in vivo* OCT and SER images were simultaneously and continuously acquired at 200 fps. Using complementary OCT and SER feature points, we also demonstrate multi-volumetric registration and widefield mosaicking. Our results show that SECTR addresses unmet needs in *in vivo* imaging and motion-tracking to provide anatomically accurate, densely-sampled volumetric datasets of sample

scattering over large FOVs. We believe the utility of our imaging platform extends beyond ophthalmic imaging and is broadly applicable for wide-field optical imaging with high temporal resolution.

4.2. Methods

4.2.1. Engine

A 200 kHz, 63% duty cycle swept-laser source (SSOCT-1060, Axsun) was optically buffered through a 500 m fiber spool (HI1060, Corning) to achieve 100% duty cycle at 400 kHz sweep-rate (Figure 4-1 (a)). The laser output was split into two copies and one coupler output was relayed through the fiber spool, which corresponded to a half sweep period delay. Both the original and delayed copies of the sweep were then recombined using a 50:50 coupler, effectively doubling the sweep-rate. The buffering stage input was asymmetrically split by a 53:47 fiber coupler (AC Photonics), to compensate for losses in the fiber spool. Polarization controllers were used in both arms of the buffering stage to minimize polarization mode dispersion and achieve an optimal OCT point-spread function (PSF) [158]. The unbuffered laser had a 3-dB optical bandwidth of 105 nm centered at 1060 nm, which was reduced to approximately 83 nm useable bandwidth after buffering because of spectral overlap between original and buffered sweeps.

One output from the buffering stage was split between the OCT and a Mach-Zehnder interferometer (MZI) for k-clock generation using a 90:10 coupler, and the OCT output was split into reference and sample arms using a 70:30 coupler, respectively. The reflective reference arm included a broadband fiber circulator (AC Photonics), and polarization controllers used to match sample and reference polarization to maximize OCT SNR.

The second output from the buffering stage was split between the SER and a fiber Bragg grating (FBG) for optical triggering using a 95:5 coupler. SER illumination was coupled to a DCF by fusion-splicing the 95% coupler output to the single-mode input of a prototype DCF coupler (DC1060LEB,

Castor Optics/Thorlabs). Here, the core of the DCF was used for single-mode SER illumination and the inner-cladding was used for multimode detection.

4.2.2. Optomechanical layout

SECTR reduces the size and complexity of traditional multimodal OCT and RCM systems and ensures spatiotemporal registration by using a shared galvanometer mirror (OCT fast-axis and SER scan-axis) and imaging relay (Figure 4-1 (b)). SER illumination from the single-mode core of the DCF was collimated to a 9.5 mm spot using two achromatic doublets with a combined focal length of 25.2 mm, and dispersed through a 1379 lines/mm polarization independent transmission grating (PING-Sample-420, Ibsen Photonics). The grating was imaged onto the face of the shared galvanometer scanner (Gx) through a 1.9x demagnifying 4-f relay (Figure 4-1 (b), fobj and fr), and then demagnified again by a shared 2.6x 4-f relay (Figure 4-1 (b), fs and foph) to a 1.9 mm spot at the pupil plane. OCT illumination was collimated using an 18 mm focal length triplet collimator (TC18-1064, Thorlabs) to a 5.2 mm spot, scanned by the OCT slow-axis galvanometer (Gy), and demagnified across a 1.3x (Figure 4-1(b), fs and fR) and the shared 2.6x (Figure 4-1 (b), fs and foph) 4-f relay to a 1.6 mm spot at the pupil. OCT and SER beams were combined at the focal planes of their respective relay telescopes across two adjacent faces of a custom prism mirror (Figure 4-1(b), PM). The mirror was designed with an apex angle of 157.5o to colinearly combine the reflected output of OCT and SER optical paths oriented at 45o angular separation. The prism mirror was used in place of a beamsplitter to maximize optical throughput, and the OCT and SER paths were focused onto opposite sides of the apex to minimize spatial separation between their respective fields (340 µm at the image plane).

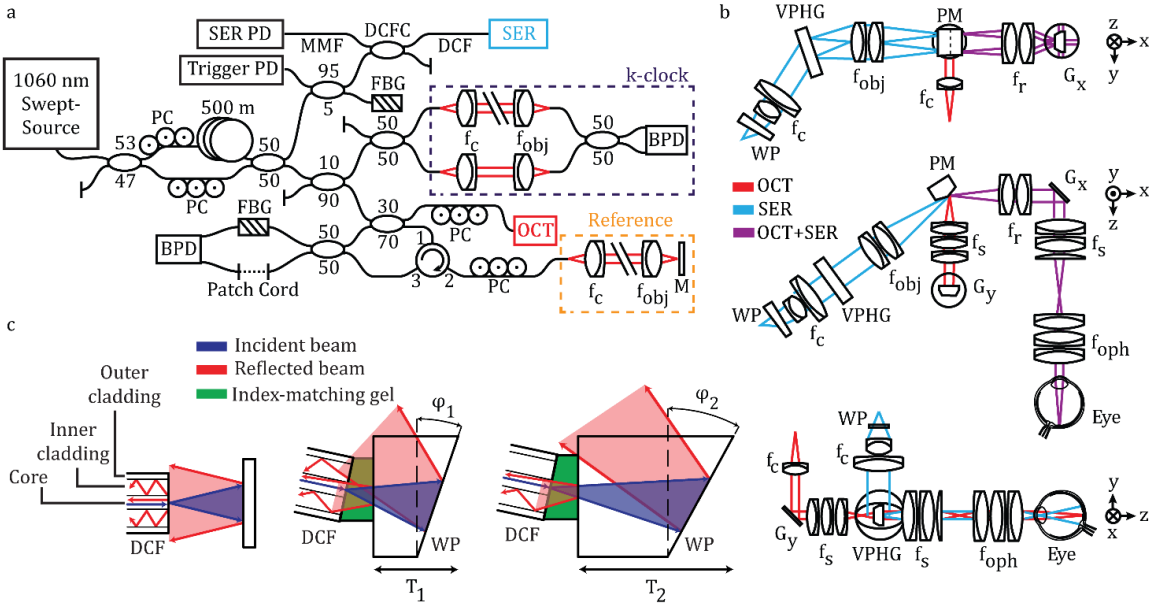

Figure 4-1 - SECTR system schematic. (a) A 1060 nm swept-laser source was optically buffered and split between OCT and SER arms. One output of the buffering stage was split for OCT and k-clock, and the path was subsequently split between a reflective reference and sample arms. The second output of the buffering stage coupled SER illumination to a DCF coupler for single-mode illumination and multimode detection through the core and inner-cladding of the DCF, respectively. FBGs in the SER and OCT arms were used to generate a wavelength-specific trigger and remove phase-noise from laser sweep jitter, respectively. (b) Orthogonal cross-sections showing SECTR beam paths and imaging optics (OCT, red; SER, blue; shared OCT+SER, purple). OCT and SER paths were combined by a prism mirror and shared a galvanometer scanner (Gx: OCT fast-axis and SER scan axis). (c) Schematics showing back-coupling of end-face reflections in a DCF from the fiber-air interface and a downstream air-glass interface (left). Both reflections were reduced by coupling the DCF to a wedge-prism (WP) with thickness, T1, and wedge angle, φ1, (middle) and were minimized for T2 and φ2 (right). BPD, balanced photodiode; f, collimating, objective, ophthalmic, relay, and scan lenses; Gx, y, galvanometer scanners; M, mirror; MMF, multimode fiber; PC, polarization controller; PD, photodiode; PM, prism mirror; VPHG, grating.

4.2.3. Suppression of DCF end-face reflection back-coupling

The major limitation of illumination and collection through the core and inner-cladding of DCFs, respectively, is the strong fiber end-face reflection that dominates sample backscattering in direct-detection modalities such as RCM and SER (Figure 4-1 (c)). Conventional fiber termination methods, such as angled physical contact, preferentially couple end-face reflections into the clad and result in higher background signals for DCFs as compared to flat-polished terminations. We mitigate end-face reflections by index-coupling a flat-polished DCF to the flat face of a wedge prism (Figure 4-1 (c), middle and right). By optimizing the wedge prism thickness and angle, we spatially offset the dominant glass-air interface reflection to minimize coupling into the DCF inner-clad (Figure 4-1 (c), right).

ZEMAX simulations showed a minimum required wedge prism base thickness of 1 mm and angle of 10o for a DCF with 0.14 core numerical aperture and 105 µm inner-clad diameter. Using a wedge prism with 3 mm base thickness and 11.2o angle (PS812-B, Thorlabs), we measured a 12.5x reduction in back-coupled end-face reflections (Figure 4-2).

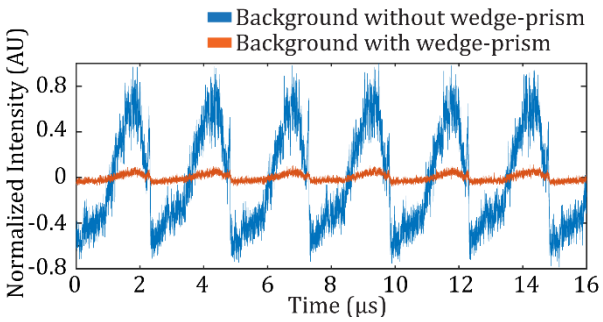

Figure 4-2 - Plot of background signal shows >12.5x reduction in the mean intensity due to back-coupled fiber end-face reflections.

4.2.4. Optical performance and sampling requirements

SECTR design was optimized and performance was simulated using ZEMAX, and the Pomerantzeff eye model was used to evaluate optical performance at the retina [159]. On-axis OCT and the central 23o SER field spot-sizes were diffraction-limited with an Airy radius of 13 and 10.5 µm, respectively (Fig. 2). In addition to spot-size, SER resolution along the spectrally-encoded dimension was also dependent on the number of resolvable spots (Nr) at the grating. For a 9.5 mm collimated spot, our grating resolved a maximum of 1831 spectral channels across the full 105 nm bandwidth of our unbuffered laser sweep. Spectral overlap after optical buffering reduced the useable bandwidth, and consequently reduced the number of resolvable spots to 1447. Thus, at 400 kHz buffered sweep-rate, a >1.16 GHz clock was required to critically sample the SER signal.

4.2.5. Triggering and clocking

SECTR imaging was synchronized to the laser sweep-rate using an optical trigger. Five percent of the SER arm from the buffering stage was coupled to a 1017.06±0.08 nm FBG (O-E Land) with 95% reflectivity. The reflection from the FBG was detected with a 250 MHz InGaAs PIN photodiode

(FPD510-F, MenloSystems) and amplified with a 1.6 GHz 37 dB electronic amplifier (ACA-2, Becker & Hickl) to provide a wavelength-specific trigger for a shared high-speed digitizer. The auxiliary channel of the digitizer was configured to output an electronic TTL signal synchronized to the optical trigger and used to trigger galvanometer scan waveforms generated with a digital-to-analog converter (PCI-6221, National Instruments).

An external MZI was used to generate a second optical clock for linear-in-k sampling of each laser sweep. The MZI path-length mismatch was set to generate a 600 MHz

fringe frequency that was detected on a 1.6 GHz balanced photodiode (APD481-AC, Thorlabs), high-pass filtered (SHP-400+, Mini-Circuits), and conditioned using an analog comparator (ADCMP565, Analog Devices). The comparator output was then electronically doubled [160] and the output signal was amplified (ZKL-2+, Mini-Circuits), band-pass filtered between 395-700 MHz (SHP-400+ and SLP-750, Mini-Circuits), and frequency-doubled (FK-5-S, Mini-Circuits). Finally, the signal was band-pass filtered between 1000-1400 MHz (SHP-950+ and SLP-1650+, Mini-Circuits), resulting in a stable 1.2 GHz k-clock for linear-in-wavenumber and Nyquist sampling of OCT and SER signals. However, due to data-alignment and triggering constraints inherent to the digitizer used, each 400 kHz sweep was sampled with 2560 samples-per-sweep instead of the maximum 3000 samples-per-sweep, which resulted in a combined OCT and SER throughput of 2 gigapixels-per-second (Supplementary Note 5).

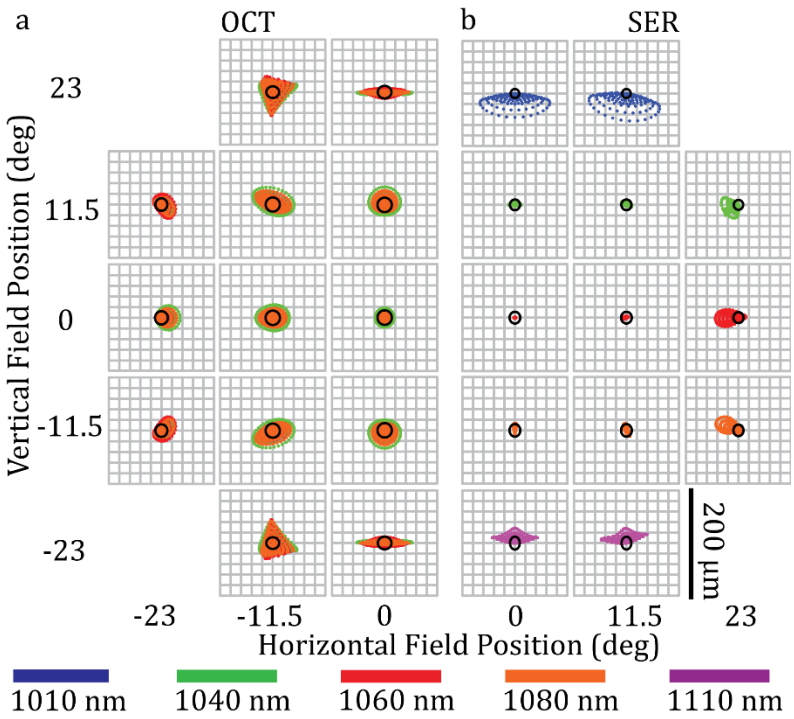

Figure 4-3 - SECTR ZEMAX spot diagram. Spot matrix for (a) OCT and (b) SER showing the full circular FOV simulated at the retina. The FOV was symmetric and only half-fields are shown for each modality. (a) OCT spots were diffraction-limited on-axis, whereas (b) SER spots were diffraction- and near diffraction-limited within the central 23o of the field. The Airy radius was 13 and 10.5 µm for OCT and SER, respectively.

4.2.6. Detection, acquisition, and phase-alignment

SECTR signals were acquired using a 12-bit dual-channel 4 GS/s digitizer (AT-9373, AlazarTech). The OCT signal was detected using a 1.6 GHz balanced photodiode (APD481AC, Thorlabs). A 1083.08±0.123 nm FBG with 99.94% reflectivity (O-E Land) was coupled to one input of the balanced photodiode to generate a reference peak in the detected OCT interferogram [161]. In post-processing, this peak was used to spectrally align both OCT and SER samples to measure trigger fluctuation, compensate for inherent sweep-to-sweep jitter, and eliminate coherent noise artifacts from OCT data [160,162]. Coaxial cable lengths for the OCT and k-clock were matched to avoid depth-dependent degradation of the OCT axial PSF due to phase errors [160].

Backscattered SER light was collected through the inner cladding of the DCF and detected through the multimode arm of the DCF coupler using a 2.2 GHz amplified photodiode (RIP1-JJAF,

Voxtel). The photodiode output signal was amplified with a 20 dB electronic amplifier (ZFL-500, Mini Circuits) and sampled using one channel of the high-speed digitizer. SER data was acquired simultaneously with OCT on the second channel of the shared digitizer. Multimode collection using the DCF increased optical throughput by >3.5x and reduced speckle contrast by >3.6x as compared to single-mode [149].

C++ software was developed for acquisition, processing, display, and data archival at a total data throughput rate of 4 GB/s. Data was streamed to a high-speed RAM disk (800 MHz DDR3), which allowed up to 10 seconds (40 GB) of continuous acquisition. Circular buffering was not performed to avoid data loss; acquisition time was limited by the available RAM disk space. The data was sub-sampled, processed, and displayed live at 17 fps for real-time aiming and alignment. A background frame was obtained with each acquisition to subtract the DC spectral shape of the source from the OCT and the SER frames. Numerical dispersion compensation was performed on each OCT frame [124].

4.2.7. Multi-volumetric mosaicking

A custom semi-automatic algorithm was developed for multi-volumetric registration of overlapping retinal datasets into an ultrawide-field mosaic. SECTR frames were pre-processed to correct for bulk-motion in the axial and lateral planes, using OCT and SER data, respectively. OCT cross-sections were then flattened to eliminate tilt and curvature variations in retinal layers and enable volumetric mosaicking.

Global non-rigid transformations between the SER frames, corresponding *en face* OCT projections, and overlapping volumetric datasets were automatically calculated using spline transformations based on automatically-extracted anatomical landmarks [163]. Vascular features were first enhanced using a Gabor kernel at various orientations. A skeletonized map of the vasculature was then generated and convolved with a dictionary of predefined 3x3 neighborhood kernels to automatically identify the branching points, which were used as landmarks for the non-rigid registration. The only manual step in our processing algorithm was the addition of choroidal vasculature

branching points and intersections between retinal and choroidal vascular projections to improve the registration accuracy. All SECTR volumes were registered to one central volume.

Accuracy of the mosaicking output was quantified using cross-correlation of the overlapping regions of the adjacent volumetric datasets. In locations with more than two overlapping volumes, a global coefficient was calculated as the arithmetic mean of all the calculated coefficients.

4.3. Results

4.3.1. Optical performance

SECTR optical performance was evaluated by imaging a USAF-1951 resolution test chart at the intermediate image plane before the ophthalmic lens (Figure 4-1 (b), foph). ZEMAX simulated lateral resolution in this plane for OCT and SER were 37 and 30 µm, respectively. Imaging results showed that OCT could resolve 35 µm features and SER could resolve 39 µm and 28 µm features in its spectrally-encoded and scanned dimensions, respectively (Figure 4-4).

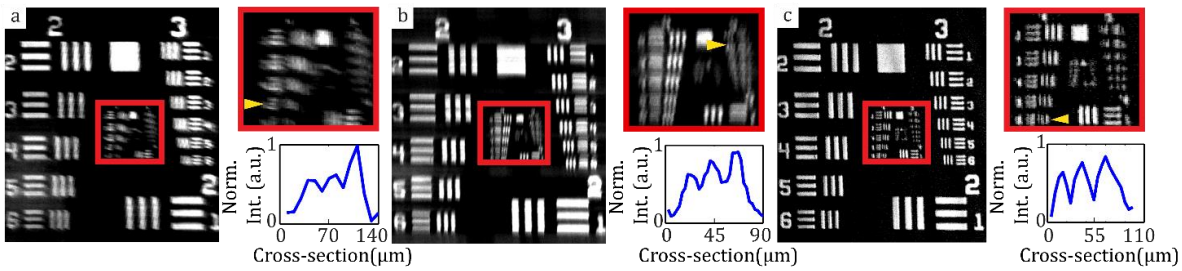

Figure 4-4 - SECTR lateral resolution characterization. (a) *En face* OCT volume projection and magnified region showing contrast cross-section (inset) of group 4, element 6 (arrow, 35 µm). (b), (c) Two SER images were acquired at offset image planes to compensate for slight astigmatism at the focus. SER images and contrast cross-sections with the (b) spectrally-encoded and (c) scanned dimensions in focus showing group 4, element 5 (arrow, 39 µm) and group 5, element 2 (arrow, 28 µm), respectively. Anisotropic SER lateral resolution is a result of dominant chromatic aberration.

4.3.2. OCT sensitivity and axial resolution

OCT had a measured SNR of 96 dB with 1.3 mW of incident power. The -6 dB fall-off depth was 7.5 mm and full imaging range was 9.56 mm when sampled using the 1.2 GHz k-clock (Figure 4-5 (a)). The axial resolution, measured using a calibrated reflector, was 11.2 µm full-width at half-maximum

(FWHM) at 500 µm from the zero delay in air and did not degrade significantly over the full imaging range (Figure 4-5 (b), (c)).

4.3.3. *In vivo* human ophthalmic imaging

In vivo SECTR imaging was demonstrated in a healthy volunteer under an IRB-approved protocol. The optical power incident at the pupil was 1.3 mW for OCT and 2.65 mW for SER, which was well below the American National Standards Institute (ANSI) MPE limits for combined point-scanning and extended source illumination at 1060 nm light [164] and less than that used in previously published systems [6,149].

A >45o (15 mm diameter) FOV on the posterior retina (Figure 4-6) and anterior segment (Figure 4-7) was imaged simultaneously with OCT and SER. OCT volumes were sampled with 2560 x 2000 x 1400 pix. (spectral x lateral x lateral) in 7 s, and corresponding SER images were sampled with 2560 x 2000 pix. (spectral x lateral) at 200 fps. High frame-rate SER images provided *en face* views of anatomic structures for aiming and fixation and showed sample motion dynamics from saccades (retina) and pupil dilation (iris). Retinal OCT cross-sections clearly showed tissue layers, the fovea, and the optic nerve. The cornea, iris, and anterior lens capsule were also clearly resolved on anterior segment OCT. Comparison of respective anatomic landmarks between *en face* OCT volume projection and SER images showed spatiotemporal co-registration of overlapping FOVs (Visualizations 1 and S2).

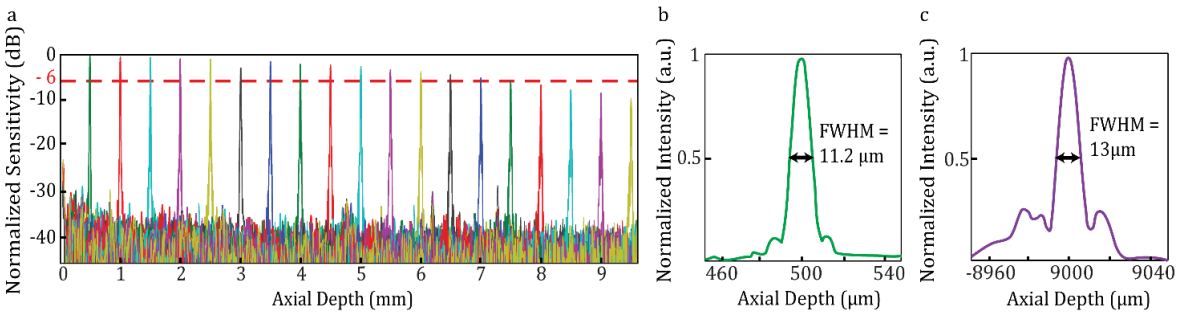

Figure 4-5 - OCT fall-off plot showing SNR and axial point spread function measurements. (a) A -6 dB fall-off depth of 7.5 mm and full imaging range of 9.56 mm were measured when imaging with a 1.2 GHz k-clock. (b) The FWHM of the axial PSF in air was between 11-13 µm across the full imaging range.

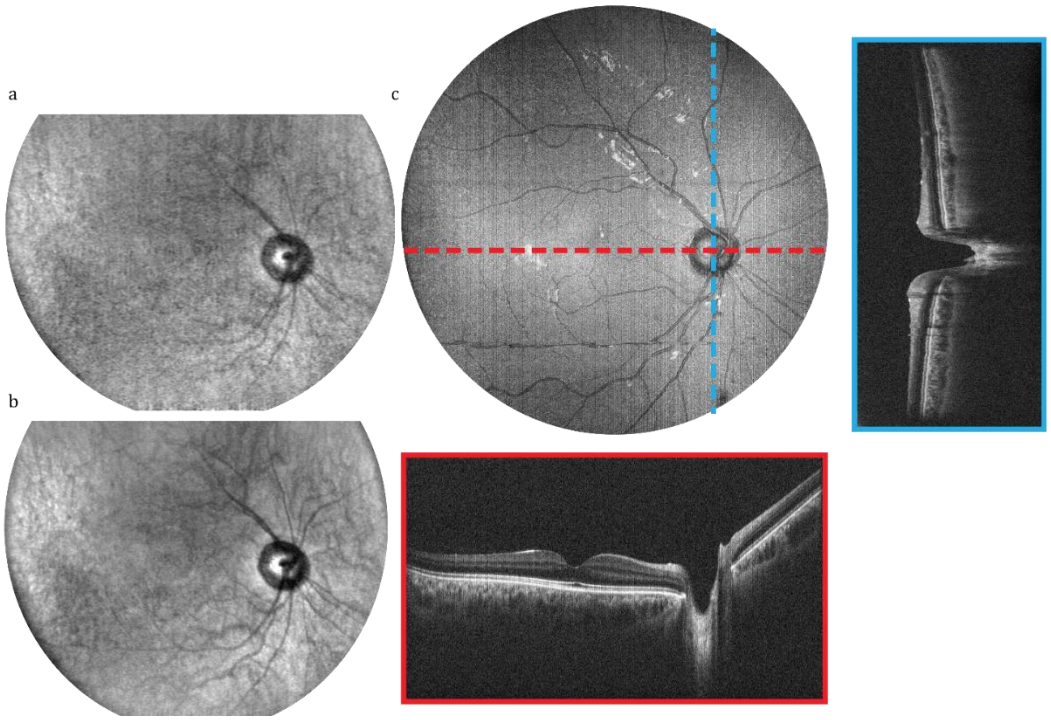

Figure 4-6 - ***In vivo*** **SECTR imaging of the posterior retina with >45o (15 mm) FOV in a healthy volunteer (a) Raw and (b) 5-frame average of 2560 x 2000 pix. (spectral x lateral) SER images acquired at 200 fps. (c)** ***En face*** **OCT volume projection with representative 5-frame averaged fast- and slow-axis cross-sections (red and blue, respectively). OCT volume was sampled with 2560 x 2000 x 1400 pix. (spectral x lateral x lateral) in 7 s.**

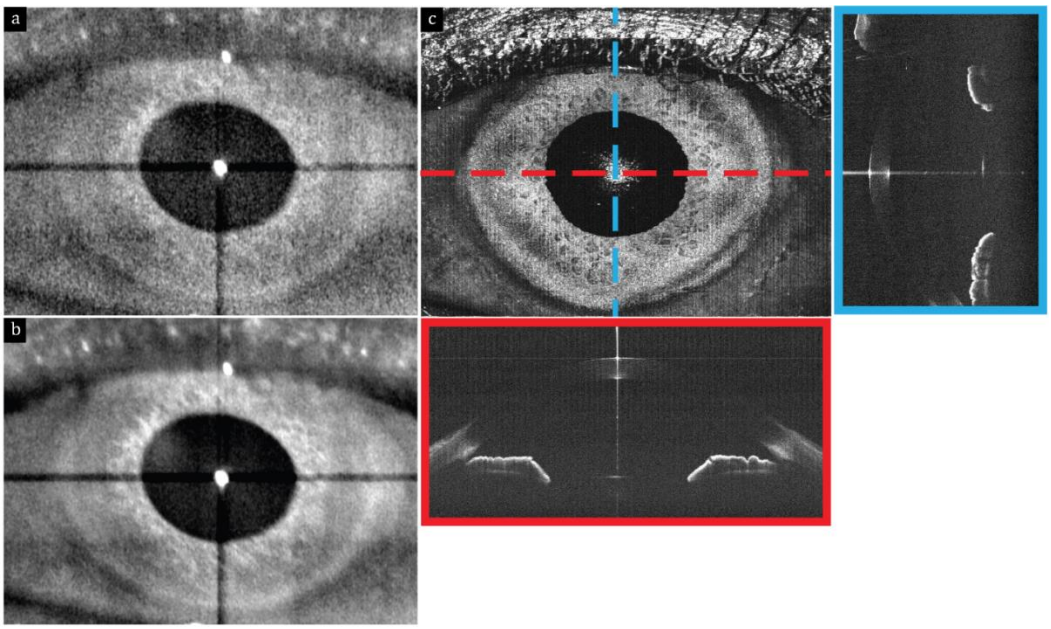

Figure 4-7 - ***In vivo*** **SECTR imaging of the anterior chamber in a healthy volunteer (a) Raw and (b) 5-frame average of 2560 x 2000 pix. (spectral x lateral) SER images acquired at 200 fps. (c)** ***En face*** **OCT volume projection with representative fast- and slow-axis cross-sections (red and blue, respectively) showing the entire corneal curvature, structures in the pupil, and the anterior lens capsule. OCT volume was sampled with 2560 x 2000 x 1400 pix. (spectral x lateral x lateral) in 7 s.**

4.3.4. Ultrawide-field volumetric mosaicking

Video-rate visualization of *en face* SER provided real-time feedback for multi-field aiming and acquisition, and allowed for accurate positioning of the sample to achieve desired overlap for mosaicking (Figure 4-8 (a)). Nine datasets were acquired at various retinal eccentricities with 50% overlap between the adjacent fields, and mosaicked in post-processing. Figure 4-8shows sub-fields and multi-volumetric mosaics of corresponding SER and OCT data from overlapping SECTR volumetric datasets, respectively. *En face* sub-fields (Figure 4-8 (a), (d)) are shown after registration and non-rigid transformation. Multi-volumetric mosaics (Figure 4-8 (b), (e)) show artifact-free ultrawide-field images over a 90o FOV.

Cross-correlation coefficient maps were used to verify the mosaicking accuracy (Figure 4-8 (c), (f)). In both cases, the cross-correlation value was between 0.94 and 0.97 over the entire FOV. Figure 4-9 shows an enlarged *en face* OCT projection, of the multi-volumetric mosaic, together with representative fast- and slow-axis cross-sections.

En face visualizations of the retinal pigment epithelium (RPE) and the choroid layers show shadowing from retinal (Figure 4-10 (a)), and choroidal (Figure 4-10 (b)) vasculature, respectively, and provide qualitative measures for mosaicking accuracy.

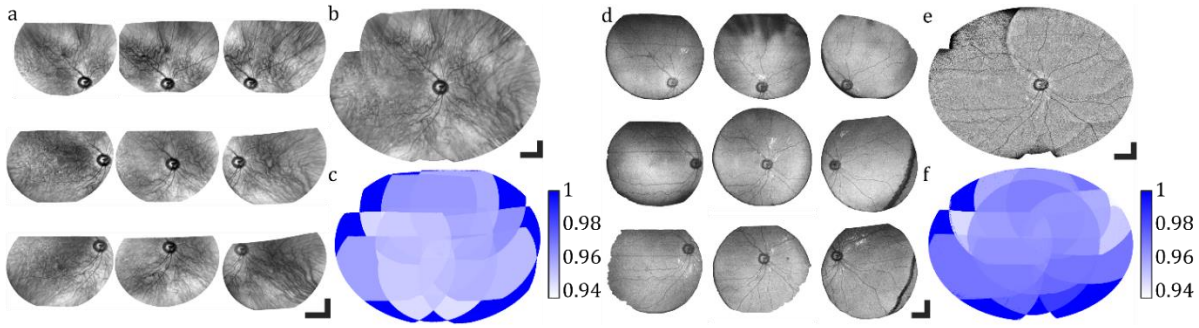

Figure 4-8 - SECTR multi-volumetric mosaicking (a) SER and (d) OCT sub-fields after multi-volumetric and non-rigid transformation (b) SER and (e) OCT wide-field multi-volumetric mosaics. (c), (f) Validation map representing cross-correlation coefficients after mosaicking. Scale bars: 10°.

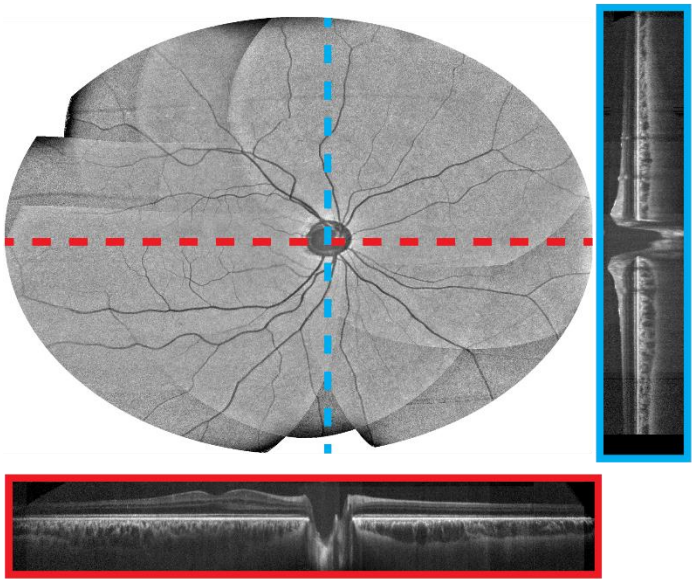

Figure 4-9 - Multi-volumetric mosaic of the posterior retina with a 90° FOV. *En face* OCT volume with representative fast- and slow-axis cross-sections (red and blue, respectively) after flattening, registration, and mosaicking.

4.4. Discussion

4.4.1. SER optical performance

Optical performance characterization showed astigmatism in the SER focal plane (Figure 4-4). To compare lateral resolution with ZEMAX simulations, the USAF-1951 resolution test chart was imaged at slightly offset image planes, each optimized for lateral resolution in either the spectrally-encoded or raster-scanned dimension. In *in vivo* imaging, the ophthalmic lens (Figure 4-1 (b), foph) was positioned to optimize overall image quality. The astigmatism was not inherent to the optical design but rather a result of bulk-optics alignment error between the two SER imaging relays (Figure 4-1 (b), fc-fobj and fr-fs).

In addition to astigmatism, our results also showed differences between SER lateral resolutions in the spectrally-encoded and raster-scanned dimensions. This was attributed to dominant chromatic aberration, which maps to spherical aberration in SER. This effect was magnified in the characterization plane because the system was designed for optimal performance in the eye. Characterization of imaging performance in an intermediate image plane without the ophthalmic lens

(Figure 4-1 (b), foph) and eye removes significant longitudinal chromatic aberration that was not otherwise compensated. Thus, *in vivo* results have expectedly better resolution.

4.4.2. Data throughput considerations

At the optimal source duty cycle, the required sampling rate would increase to approximately 2 GHz, which approaches the speed limit of state-of-the-art digitizers. In addition, an 8-lane PCI-express 3 bus is limited to <7 GB/s of data throughput and fundamentally limits digitizer readout speeds at full bit-depth. However, data throughput limitations may be overcome by reducing imaging bit-depth, which has been previously shown to not significantly impact swept-source OCT SNR [165]. Another potential limitation to higher clock-rates is the capacity to store data. In this demonstration, SECTR data were streamed to computer memory that was benchmarked at >10 GB/s throughput. However, expanding memory to increase total acquisition duration becomes prohibitively expensive. RAID0 striping of high-speed solid-state drives (SSDs) or PCI-express SSDs, which are capable of sustained write-speeds of >4 GB/s, may be a cost-effective alternative fast storage solution.

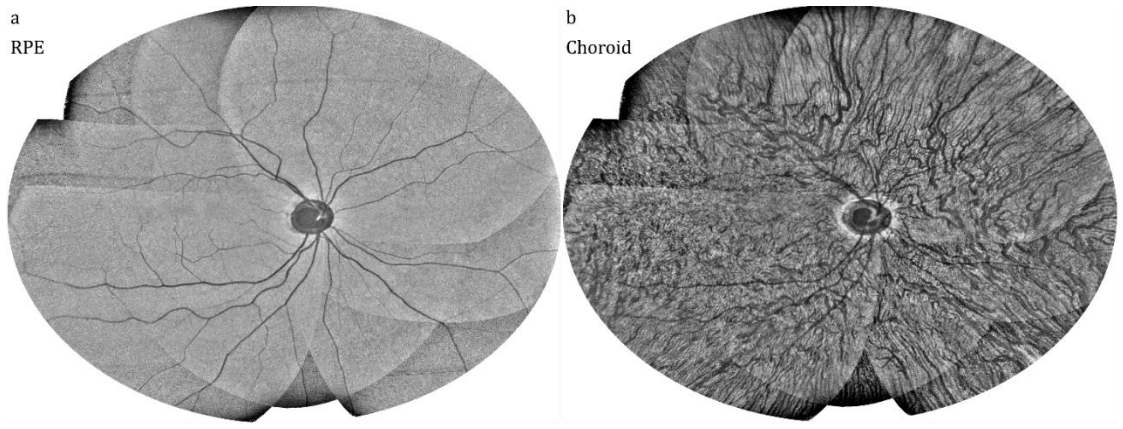

Figure 4-10 - *En face* multi-volumetric OCT mosaics at different retinal layers (a) 20-frame average in depth around the RPE and (b) 25-frame average in depth in the choroid.

4.4.3. Ultrawide-field volumetric mosaicking

Three-dimensional acquisition using SECTR enables aiming, motion-tracking (Figure 4-11) and multi-volumetric registration and mosaicking, as demonstrated in our preliminary results. Partially-coherent SER detection provides more anatomical features and allows for more accurate and robust registration as compared to coherent detection.

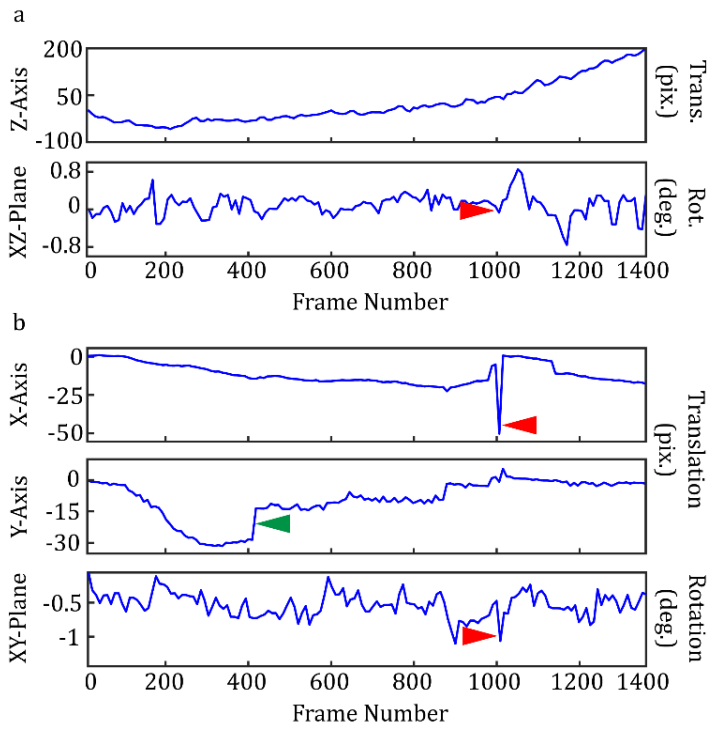

Figure 4-11 - Motion-tracking results from raw (a) OCT and (b) SER frames. A saccade in the x-axis (red arrows) was observed as OCT rotational and SER translational/rotational motions. A saccade in the y-axis (green arrow) was orthogonal to the OCT fast-axis and only observed on SER.

The described algorithm for segmentation and flattening of the RPE was robust against variations in the retinal curvature and tilt throughout the acquired volumes. However, folding of mirror image artifacts in the OCT FOV resulted in RPE segmentation errors. Moreover, as explained in Section 2.7, the limited number of automatically extracted anatomical landmarks limited the mosaicking accuracy. While the inclusion of manually-extracted landmarks improved the final registration results, it increased the overall processing time, and was prone to placement errors. The cross-correlation maps demonstrated good registration and mosaicking performance. However, the accuracy of our method may be further improved by the introduction of new landmarks, such as

inflection points along the retinal and choroidal vasculature. Additionally, complete automation of the landmark extraction step may minimize landmark placement errors and reduce overall processing time.

4.5. Conclusion

We demonstrated novel multimodality wide-field imaging, and multi-volumetric registration and mosaicking using SECTR. Future developments in swept-source laser, digitizer, and storage technology may be directly implemented to improve SECTR imaging resolution and speed. To the best of our knowledge, this is the fastest implementation of simultaneous *en face* and cross-sectional multimodality imaging to date, and the technology has broad potential applications in *in vivo* imaging in research, commercial, and clinical settings.

Chapter 5

5. Non-contact characterization of compound optical lenses using reflectance confocal microscopy, low-coherence interferometry, and computational raytracing

The ability of an optical system to produce a true image of an object is fundamentally limited by conflicting requirements of minimizing aberrations and distortions while maximizing the numerical aperture (NA). Aberrations and distortions are direct results of lens geometry and glass material. Thus, it is common practice in optical design to utilize multiple different optical elements to balance these effects. Commercial optical components such as collimators, beam expanders, and objectives, enable rapid prototyping and assembly of imaging systems based on a desired performance specification. While convenient, these components often employ proprietary designs. This precludes accurate system-level simulation using computer-aided design tools, and may lead to suboptimal performance. In some cases, published patents may provide information about the optical model, however these may be outdated or inaccurate, requiring further optimization to match the experimentally observed performance [166–168]. Even when optical models are available, manufacturing inaccuracies present another source of potential design errors. These inaccuracies may arise from deviations from the specified relative geometry between elements in a compound lens such as tilt, decenter, orientation and relative offsets; or from errors in the glass materials.

There is currently no non-destructive method for complete characterization of geometry and glass materials of multi-element optical lenses. Alternatively, information about an optical element for design purposes may be obtained in the form of aberrations and distortions using wavefront sensing techniques [169]; or in the form of a ray-transfer matrix using optical ray-tracing [170–172]. Quantitative aberration information is useful in guiding the optical design, but is challenging to directly include in a simulated model. The ray-transfer matrix is a powerful method for modeling optical systems, yet it does not provide phase information, and is only valid in the paraxial approximation. Furthermore, using either approach, the obtained measurements are only valid for the characterized configurations including wavelengths, fields, and propagation direction. Therefore,

estimating the full prescription of an unknown optic is essential for overcoming the aforementioned limitations.

Coherence-gated imaging methods such as low coherence interferometry (LCI), and optical coherence tomography (OCT) provide axial-priority imaging in transparent and semi-transparent media with resolutions down to 1 um and sensitivities exceeding 100 dB [1]. LCI and OCT have been previously demonstrated for surface profilometry [173–175], measurement of internal thicknesses of optical assemblies and biological samples [1,176], and estimation of internal curvatures [175,177]. However, since the measured path lengths are proportional to the group velocity of the illumination wavelength bundle in the propagation medium, the optical properties of the medium need to be known a priori. Alternatively, several groups demonstrated simultaneous measurement of thickness and refractive index using OCT by introducing an additional measurement of the focal plane shift within the sample by a technique termed "focus-tracking" [178–184]. Since LCI-based techniques utilize broadband sources, many of these methods relied on approximating the phase refractive index (np) and the group refractive index (ng), which limited the accuracy of the obtained measurements. This approximation may be avoided by introducing additional measurements to separate np and ng through estimation or direct measurement of the dispersion parameter [184–190]. However, these measurements were typically performed in transmission, and assumed a homogenous sample, and thus were not suitable for characterization of compound optical elements. Furthermore, methods relying on focus-tracking only traced the intersection between the marginal and the chief ray, and assume a locally flat surface.

Here, we present a method for complete characterization of compound optical lenses using reflectance confocal microscopy (RCM), low-coherence interferometry (LCI), and computational ray-tracing. We show the measurement of external and internal surface radii, internal glass and air-gap thicknesses, and estimation of glass materials from a finite set of commercially available types. We validate the method on a set of 6 commercial achromatic doublet lenses (Table 1), and

demonstrate characterization of a commercial scan lens comprising four doublets. We believe this method addresses a unique gap in the design of optical imaging systems and manufacturing of optical components.

	Lens	Glass	R1	R2	R3	T	Phase Index (np) @ 830 nm	Abbe (vd)	SPHA	CLA	BFL
1	AC127-025-A	N-BAF10 SF10	18.8	-10.6	-68.1	5 2	1.6591 1.7099	47.11 28.53	8.81	-1.90	21.39
		H-ZBAF5 ZF4	18.86	-10.72	-68.23	5.007 1.996	1.6601 1.7098	47.28 28.32	9.33	-1.78	21.35
2	AC127-075-A	N-BK7 SF2	41.3	-34.0	-137.1	2.5 1.5	1.5102 1.6336	64.17 33.82	0.14	-0.62	73.10
		S-APL SF2	41.43	-34.12	-137.62	2.573 1.583	1.5112 1.6336	69.56 33.82	0.16	-0.41	72.97
3	ACN254-050-A	N-BAF10 N-SF6HT	-34.0	32.5	189.2	2 4.5	1.6591 1.7826	47.11 25.36	-16.42	3.95	-52.98
		K-LaKn7 Q-SF6S	-33.99	31.99	188.09	2.067 4.411	1.6599 1.7806	51.72 25.53	-16.09	2.59	-52.88
4	ACN254-100-A	N-BAK4 SF5	-52.0	49.9	600.0	2 4	1.5608 1.6574	55.97 32.25	-1.16	1.76	-103.88
		H-BAK7GT BAH32	-51.92	50.58	600.95	2.024 4.063	1.5608 1.6572	56.06 39.28	-1.42	3.06	-103.45
5	AC254-060-A	E-BAF11 FD10	41.7	-25.9	-230.7	8 2.5	1.6606 1.7097	48.36 28.32	8.34	-2.28	54.15
		H-ZBAF16 P-SF69	41.70	-26.0	-230.64	7.910 2.499	1.65611 1.704	48.43 29.23	10.25	-2.69	53.56

							6				
6	AC254-200-A	N-SSK5 LAFN7	77.4	-87.6	291.1	4 2.5	1.6484 1.7335	50.88 34.95	0.29	-0.54	194.31
		H-ZBAF50 H-LAF3B	77.54	-87.47	289.93	4.0771 2.513	1.6484 1.7314	50.87 44.90	0.31	-1.93	193.99

Table 5-1 - Comparison between specification and estimated prescriptions for the characterized lens elements. Lenses were tested in ZEMAX with a collimated polychromatic beam spanning the laser source spectrum. The beam diameter was set to 95% of the full aperture, and the focus was found by minimizing the root-mean-squared spot size in the image plane. Measurements for R1 and R3 were obtained in air while R2 measurements were performed through 1 glass element and corrected. Manufacturer tolerances were +/- 200 µm for thicknesses, 1% for radius, and +/- 1% for focal length.

5.1. External radius measurement

The system used to obtain all the measurements is shown in Figure 5-1(a). Light from a broadband laser was split by an 80:20 fiber-coupler. A free-space Michelson interferometer was setup using a 50:50 beam splitter cube and the back-reflected signal was detected and analyzed by a custom spectrometer. A variable pupil was placed in the reference arm to switch between LCI and RCM, and the fiber core acted as the confocal pinhole for RCM. The lens-under-test (LUT) was mounted on a 3-axis motorized stage assembly.

To obtain a radius measurement, the surface was first sampled by translating lens in the lateral plane along orthogonal (X-Y) axes. The data were processed to transform the acquired spectral information to the spatial domain. The lens surface was then segmented by taking the location of the peak along each axial line resulting in a point cloud representation of the surface. The point cloud was fit to a sphere by least-squares minimization to obtain the radius and the center of curvature.

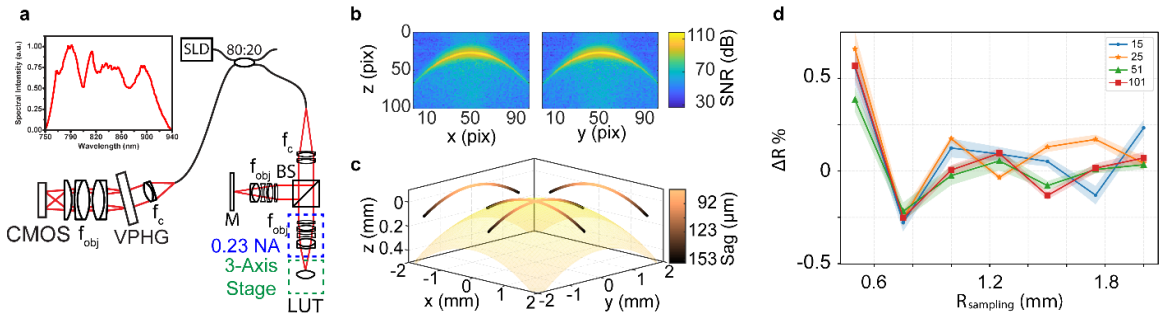

Figure 5-1 - System schematic and reference sphere calibration data (a) The laser source output was split by an 80:20 fiber coupler, and the 20% arm was used in a free-space Michelson interferometer with 0.23 image space NA. The back-coupled signal was analyzed by a custom spectrometer and acquired by a CMOS line detector. (b) Representative cross-sections of the calibration sphere surface at 1.5 mm sampling radius (Rsampling) showing SNR drop-off with decenter, (c) segmented surface in physical units overlaid on the best-fit sphere. (d) Percentage error between the measured radius and the specification radius at different sampling densities (number of samples per cross-section), where each point represents the mean of 5 independent measurements and the shaded regions show the standard deviation. SLD, super luminescent diode; NA, numerical aperture; LUT, lens-under-test; VPHG, volume phase holographic grating; fc,obj, lenses.

For accurate mapping of the pixels in the axial dimension to physical units, a ceramic reference sphere with a diameter of 14.9851 mm and 300 nm accuracy (Carl Zeiss Industrial Metrology, LLC, USA) was profiled. Cross-sections along the X- and Y-axes and the corresponding segmented points and best-fit sphere are shown in Figure 5-2 (b), and (c). The sphere was sampled with varying radial distances from the sampling origin (Rsampling), and varying sampling densities defined as number of points per cross-section. The plot in Figure 5-2 (d) shows that the accuracy of the obtained radius measurements converges between $\pm$ 0.2% of the specification radius. Since the spherical surface is, by definition, a smooth function that can be approximated by a minimum of 3 points, it can be seen that increasing Rsampling has expectedly a much larger effect on measurement accuracy than increasing the sampling density.

This result implies that when measuring a surface, Rsampling should be maximized within the imaging NA. However, since the detected signal originates from purely specular reflections, there is a path-length mismatch between the incident and the reflected beams that is proportional to the angle of incidence relative to the surface normal. Thus, the measured sag from direct segmentation of the acquired LCI data includes an additive error term which results in underestimation of the radius of

curvature of an unknown surface in proportion to Rsampling. The measured SNR value along the unknown surface is proportional to this angle of incidence, and may be used to constrain the points to be included in the sphere-fit. We applied an SNR threshold to reject points that fell below a prespecified range from the global maximum. This threshold was relative since the maximum SNR depends on the sample reflectivity. The empirically determined SNR threshold was -27.5 dB.

The measurement method was validated on a total of 24 surfaces from 6 uncemented achromatic doublets with varying curvatures (Figure 5-2 (b)). Each point on the plot represents a mean of 5 independent measurements, and the error bars represent the standard deviation. All the measurements were well within 1% of the specification, in agreement with the manufacturing tolerance.

5.2. Internal radius and thickness measurement

LCI is sensitive to reflections from refractive index differences on the order of 10-5, making it suitable for the evaluation of the internal geometry of compound lenses. However, images of internal curvatures are distorted both by refraction and path-length scaling which are functions of the phase and group refractive index of the LUT elements, respectively. If the material optical properties are known, these distortions can be corrected in post-processing [177]. However, as explained in the previous section, these distortions were further confounded by errors due to the specular nature of the imaged surfaces. It was observed that correcting the distortions along the single-pass ray paths through the LUT elements was insufficient for direct sphere-fitting. Rather, the correction resulted in an aspheric surface with a vertex radius representing the true radius of curvature.

The measurement process was simulated using a computational ray-tracing model (Figure 5-2 (a)), where chief rays were propagated over the sampled area, refracted, and scaled based on the phase and group index of the propagation material at the center wavelength. The final positions of these rays represented the corrected surface which was fit to even powers of the radial distance from the optical axis [191].

$$Z = \sum_{n=1}^{8} a_n r^{2n} \tag{5-1}$$

$$R = \frac{1}{2a_1} \tag{5-2}$$

This method was tested on 12 surfaces from the doublet lenses in Table 5-1 - Comparison between specification and estimated prescriptions for the characterized lens elements., where 6 surfaces were imaged through 1 glass element each, and 6 were imaged through 2 lens elements. The errors between the estimated internal curvatures compared to their measured values in air are plotted in Figure 5-2 (c).

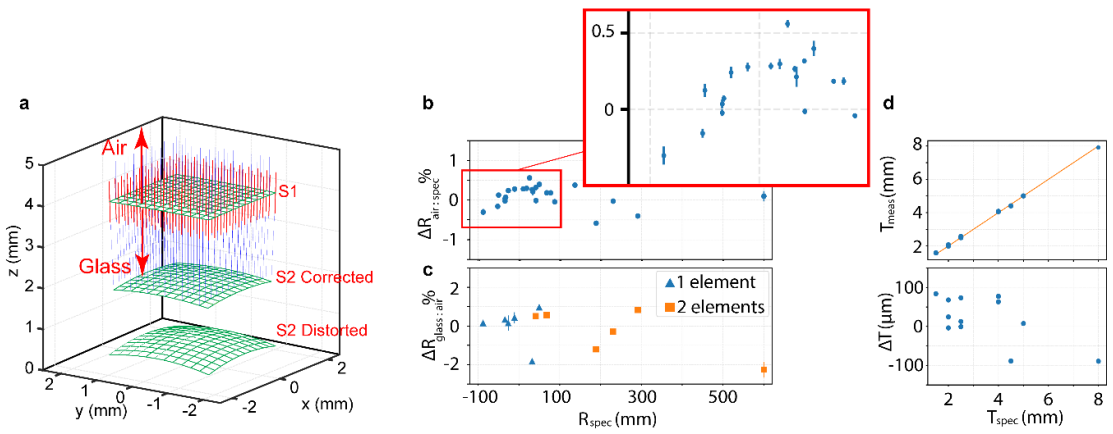

Figure 5-2 - Characterized geometry of the commercial doublets in Table 5-1 (a) Ray-tracing-based correction of surfaces imaged through glass elements, where the blue lines represent the chief rays at the sampling positions and the red lines represent the surface normal at the points of incidence. The rays are refracted at the first surface (S1) based on the glass phase index at the center wavelength and are propagated based on the measured optical distances between S1 and the distorted image of S2, and the group index of the glass at the center wavelength. The final ray positions are used to reconstruct the corrected S2. (b, c) Percentage error between all the surface radii imaged in air (Rair), and their respective specification (Rair:spec); and between radii imaged through 1 or 2 glass elements after ray-trace correction and their corresponding in-air values (Rglass:air). Each point represents the mean of 5 independent measurements, the error bars represent the standard deviation, and the inset shows a magnified view of the cluster of points between -100 and +100 mm. (d) Plots of measured thicknesses (Tmeas) against specification (Tspec) and the corresponding errors. Manufacturer tolerances were +/- 1% for radii, and +/- 200 µm for total thicknesses.

Thickness measurement was performed along the optical axis, and the only correction required was the scaling of the measured optical thickness by the group refractive index of the LUT materials (Figure 5-2 (d), (e)).

5.3. Glass material estimation

Estimation of the glass materials was performed by modeling the propagation of the illumination cone through the unknown LUT element (Figure 5-3 (a)). RCM measurements were first performed by closing the reference arm pupil. The lens was translated axially to measure the confocal axial response at the front and back surfaces of the unknown glass element (Figure 5-3 (b)). The position of the best focus at each surface was evaluated at the center wavelength, and determined as the intensity-weighted mean of the positions within 5% of the peak. The distance between the positions of the focal planes at both surfaces (confocal thickness) was smaller than the geometric thickness due to refraction of the marginal rays as a function of the phase refractive index, translation distance, and radius of curvature (Figure 5-3 (a)), where:

$$n_m \sin(\theta_m) = n_o \sin(\theta_o) = n_o \sin(\sin^{-1}(\mathrm{NA}) - \alpha) \tag{5-3}$$

$$x = R - R\cos(\alpha) \tag{5-4}$$

$$R\sin(\alpha) = (z_m - x)\tan\left(\sin^{-1}(\mathrm{NA})\right) \tag{5-5}$$

$$\theta_m = \tan^{-1}\left(\frac{(z_m - x)\tan\left(\sin^{-1}(\mathrm{NA})\right)}{\frac{t_m}{n_g} - x}\right) - \alpha \tag{5-6}$$

LCI measurements were then performed to obtain the corresponding optical thickness at 3 prespecified wavelengths spanning the illumination spectrum (λ = 769, 830, 885 nm). This was achieved by adjusting the reference arm such that the position of the stationary phase point at zero-delay was at the measurement wavelength [187]. Optical thickness measurement at these wavelengths included intrinsic information about material dispersion within the illumination bandwidth.

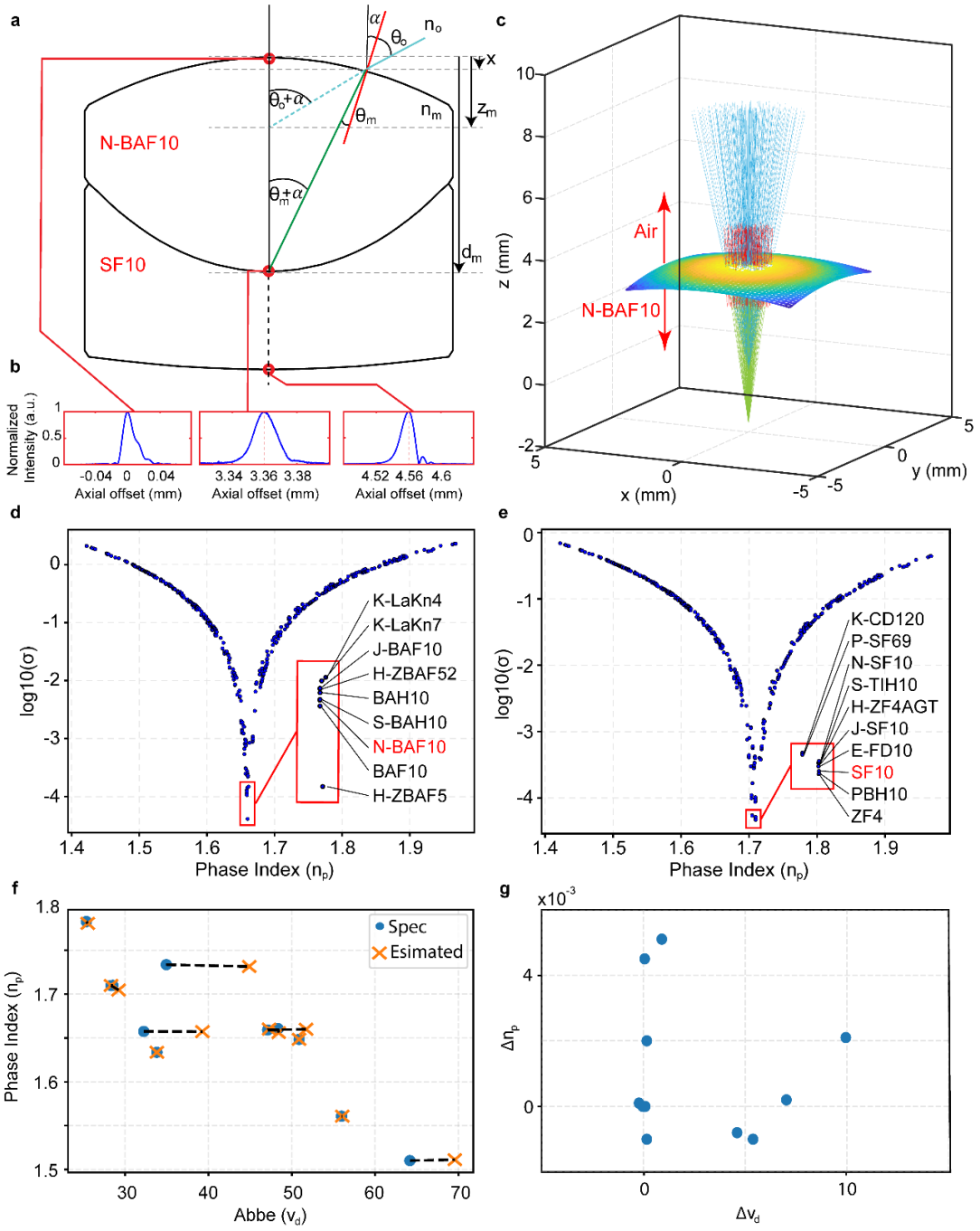

Figure 5-3 - Glass estimation (a) Geometric model of the focal plane shift inside a spherical lens. The solid blue line represents the incident marginal ray of the illumination cone, while the dotted blue line shows the unrefracted path, where the focus is initially at the upper surface of the lens element. The green line shows the refracted ray after the lower surface is brought into focus after the lens is translated axially by an offset (zm), and the red line represents the surface normal at the point of incidence. (b) Computational simulation of the measurement process in (a), where the full illumination cone is traced. (c) Representative confocal axial response measured at the 3 surfaces of an achromatic doublet (AC127-025-A). (d, e) Log-error plots corresponding to the glass elements in (c). The insets show a magnified view of the cluster of glass materials near the minima, as labeled in their respective catalogs. (f) a phase index – Abbe number diagram showing the correspondence between the specification glass and the

estimated glass for all 12 elements; corresponding pairs are connected by red dotted lines. (g) errors between estimated and specification glass Abbe number (vd) and phase index (np).

A computational ray-trace model of the propagation of the illumination cone through the lens element was created to simulate the measurement process (Figure 5-3 (c)). The position of the focus in this model was determined as the least-squares three-dimensional distance between the rays in the simulated ray-bundle. A database of the optical properties of the commercially available glass materials within the illumination bandwidth was built, with a total of 1340 materials [192]. The simulation was then evaluated exhaustively for each material in the database. The optimal glass estimate was identified by minimizing an error function (σ) representing the difference between the simulated and the measured quantities, where

$$\sigma = (d - d_s)^2 + 2(\Delta t - \Delta t_s)^2 , \tag{7}$$

and

$$\Delta t_s = d_s\big(n_g(\lambda_b) - n_g(\lambda_e)\big) , \tag{8}$$

$$d = \frac{t}{n_g(\lambda_o)} \tag{9}$$

Subscript s denotes a simulated quantity; and d, t, and ng denote geometric thickness, optical thickness, and group refractive index, respectively. λ_b, λ_o, and λ_e represent the wavelengths at the beginning, center, and end of the spectrum, respectively. Figure 5-3 (d), and (e) show plots of $\log(\sigma)$ of each material against the phase index at λ_o for the two materials of lens 1 in Table 1.

For each doublet lens in Table 1, measurements for the second element were acquired through the previous element and simulated as such. The phase index and Abbe numbers of the estimated and specification glass materials for all the lenses are plotted in Figure 5-3 (f), while the errors in the phase index and the abbe number are shown in Figure 5-3 (g).

5.4. Characterization of a commercial scan lens model

The method was further validated by characterizing a commercial broadband scan lens (Figure 5-4 (a)) (CSL-SL, Thorlabs Inc., USA). A blackbox ZEMAX model was publicly available for the lens, and was used for comparison with the obtained results. The working distance of the imaging relay in our setup was only sufficient to image through half the lens thickness. Thus, the characterization of each half was performed independently and the obtained results were combined into one prescription.

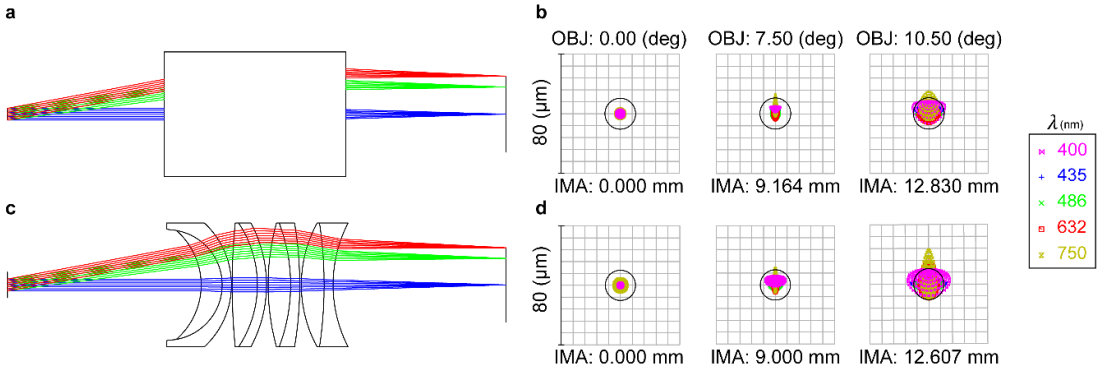

Figure 5-4 - ZEMAX ray-trace and spot diagrams at object space field angles of 0, 7.5, and 10.5 degrees and the corresponding image space positions for (a, b) black box model, and (c, d) characterized lens model of a commercial scan lens

This lens is designed for achromatic performance over the specification wavelengths (Figure 5-4 (b)). Based on this, for each lens element, a set of candidate glass materials were selected within the range of errors shown in Figure 5-3(f), and (g) around the global minimum. A hammer optimization for glass materials within these identified candidates was performed in ZEMAX to minimize chromatic aberration. The final characterized lens model is shown in Figure 5-4 (c). Since blackbox models do not provide aberration information, the spot diagrams and the final image space centroid positions are provided here for comparison of the characterization results (Figure 5-4 (b), (d)). The characterized image space NA and effective focal length were respectively 0.0291, and 68.74 mm; compared to 0.0286, and 70 mm in the blackbox model.

5.5. Discussion

This paper describes a self-contained system for full characterization of compound optical lenses. In the evaluation of curvatures, the use of a free-space interferometer was crucial to guarantee mechanical coupling between the reference and the sample arms and avoid measurement errors due to relative sub-coherence length vibrations. This is analogous to previously reported findings in confocal microscopy profilometry of highly reflective surfaces [193], where irregularities smaller than the optical resolution introduced spurious noise to the data that limited the achievable accuracy. The repeatability of the measurements was ultimately limited by the mechanical performance of the motorized stages. One limitation of our method was that spherical geometry was assumed for both external and internal curvatures. Thus, for aspheric surfaces, higher-order ray-propagation and correction models may be needed.

The overall accuracy of our reported results in both geometry and glass estimation was governed by the design parameters of the system, namely the NA and the working distance of the imaging relay, and the optical bandwidth of the illumination source. These system parameters are scalable based on application and desired accuracy. In manufacturing of compound lenses, the end goal may be accurate assessment of the final relative geometry of the different elements, while glass materials are known a priori. In this case, a lower NA imaging relay with a longer working distance is more favorable for rapid acquisition of full cross-sections of the lens assembly, which enables evaluation of tilt, decenter, and air-gap thicknesses. Furthermore, measurements with submicron accuracy may be achieved by utilizing laser sources with shorter coherence lengths. In research applications, such as biological microscopy, it is often desirable to design high resolution imaging systems involving commercial lens assemblies. In this case, accurate characterization of the glass materials is required, since it dictates the realized accuracy in both geometry and aberrations.

Previous efforts in measuring material properties analytically were mainly limited to surfaces that may be assumed locally flat within the illumination cone, traced the intersection of the marginal

ray with the chief ray, and in some cases assumed an approximate equality between group and phase refractive index. Our computational ray-tracing approach addresses all of these limitations, and provides several key advantages that make it well-suited for the problem of lens-characterization:

The ability to trace an arbitrary number of rays results in more accurate simulation of the focal shift, inherently accounts for the effects of geometric aberrations from both the imaging relay and LUT surfaces, and is easily extendable to arbitrary surface geometries.

The use of a finite set of glass types constrains the solution-space to a set of practically attainable prescriptions, and eliminates the need for approximate numerical solutions.

Measuring the optical thickness at 3 different wavelengths provides an indirect measure of dispersion, further constraining the set of possible solutions within the characterization bandwidth.

From Table 1, it can be seen that the resulting aberrations were within 2 waves from specification. These deviations were found to be mainly due to errors in the identified glass materials. Additionally, the glass estimation method tended to overestimate the Abbe number. This is likely attributable to the fact that glass materials are less dispersive in the NIR than in the VIS regime. The glass estimation accuracy may be further enhanced by employing more constraints to the simulation based on the lens manufacturer or other prior knowledge (Figure 5-4), or by using two or more light sources. For example, if a lens was manufactured by Carl Zeiss, limiting the glass search to the Schott catalog would be a reasonable optimization and reduces the set of possible solutions by an order of magnitude. Alternatively, performing the measurements and the simulations for glass estimation at two or more center wavelengths may provide a robust constraint for accurate glass identification, provided that the separation between the center wavelengths is enough such that the difference in the refractive index dominates the measurement noise. This may be achieved by utilizing supercontinuum sources and a set of suitable bandpass filters and spectrometers.

5.6. Conclusion

We presented a self-contained system for complete characterization of compound optical lenses using RCM, LCI, and computational ray-tracing. The method was validated on a compound commercial scan lens with comprising 4 doublet lenses. Our approach for glass estimation addresses several limitations in previously reported methods for measurement of optical properties of materials, and is translatable to arbitrary surfaces. Furthermore, the system performance is scalable based on the utilized light sources, and the optical design of the imaging relay in the sample arm. We believe this system may have applications in research settings, by facilitating optimal designs involving commercial lenses with unknown prescriptions, as well as in manufacturing of optical components by verifying the relative geometry of the different elements within an assembly.

5.7. Methods

The laser source used was a superlum SLD with 830 nm center wavelength and 170 nm bandwidth. The 3-axis stage assembly comprised an XY fast-scanning stage (MLS203-2, Thorlabs Inc., USA), and an additional stage for the Z-axis (MTS25-Z8, Thorlabs Inc., USA), mounted by a custom 3D printed adaptor.

Chapter 6

6. Resolution-enhanced and throughput-optimized microscope-integrated iSECTR for *in vivo* imaging

6.1. Introduction

Progressive ocular diseases usually require surgical management at advanced stages, which involves precision manipulation of delicate semi-transparent structures in the eye. Limited visualization of these tissue layers remains a critical barrier to improving clinical outcomes and developing novel surgical techniques. While recent clinical intraoperative optical coherence tomography (iOCT) studies have shown imaging of surgical vignettes [23,24,72], these seconds long visualizations of specific pathologic features do not provide dynamic information about anatomical deformations resulting from surgical manipulation, which are relevant for predicting postoperative visual function, nor do they allow for comprehensive analysis of the clinical value of iOCT-guided surgical decision-making. While increases in imaging speed has enabled iOCT imaging of surgical dynamics at ~5 volumes-per-second [194], several critical barriers need to be overcome before the technology can be broadly disseminated and clinically adopted: (1) Static field-of-views (FOVs) require manual instrument-tracking and limits imaging to single surgical maneuvers (e.g., single retinal membrane sweep); (2) high frame-rates are achieved by sparse sampling, which limits FOV size and constrains the spatial extent of imageable surgical maneuvers; and (3) small iOCT FOV also limits the number of fiducials and ability to co-register data with microscopy. Thus, the surgeon is forced to estimate the location of features-of-interest, identified using iOCT, on the microscopy field while still performing surgical maneuvers using conventional white-light visualization. We previously addressed these limitations in image-guided ophthalmic microsurgery by developing microscope-integrated multimodal intraoperative swept-source spectrally encoded scanning laser ophthalmoscopy and optical coherence tomography (iSS-SESLO-OCT) [27]. Complementary *en face* images enabled orientation and co-registration with the widefield surgical microscope view

while OCT imaging enabled depth-resolved visualization of surgical instrument positions relative to anatomic structures-of-interest. In addition, we demonstrated novel integrated segmentation overlays for augmented-reality surgical guidance.

Unfortunately, our previous system lacked the resolution and optical throughput for *in vivo* retinal imaging and necessitated removal of cornea and lens. These limitations were predominately a result of optical aberrations from imaging through a shared surgical microscope objective lens, which was modeled as a paraxial surface. Here, we present an optimized intraoperative spectrally encoded coherence tomography and reflectometry (iSECTR) system. We use a novel lens characterization method to develop an accurate model of surgical microscope objective performance and balance out inherent aberrations using iSECTR relay optics. Using this system, we demonstrate *in vivo* multimodal ophthalmic imaging through a surgical microscope.

6.2. Methods

6.2.1. iSECTR Engine

iSECTR was interfaced with a 200 kHz 1050 ± 50 nm source (OCT-1060, Axsun Technologies) buffered to 400 kHz at 100% duty cycle for concurrent spectrally encoded reflectometry (SER) and OCT imaging. Digitization was performed for SER and OCT simultaneously on dual input channels of a 4 GS/s digitizer (ATS9373, Alazartech) at 1.4 GS/s per channel. SER and OCT were detected using a 580 MHz APD (RIP1-JJAF, Voxel) and 1.6 GHz InGaAs dual-balanced photodiode (PDB480C-AC, Thorlabs), respectively.

6.2.2. Ophthalmic surgical microscope objective characterization

The ophthalmic surgical microscope objective doublet was characterized using OCT [195]. Briefly, a combination of OCT cross-sectional imaging of surface curvatures (Figure 6-1 (a), (b)) and

focus tracking was used to estimate the glass thicknesses, refractive index, and intermediate curvature of the doublet. The resulting optical model (Figure 6-1 (c)) and corresponding optical aberrations (i.e., spherical) was integrated with existing optics for a SECTR scan-head to design an intermediate surgical microscope relay telescope to both magnify the SECTR spot-size and balance out aberrations from the objective lens. Retina imaging performance through iSECTR and surgical microscope optics was optimized using the Polan's eye model [196].

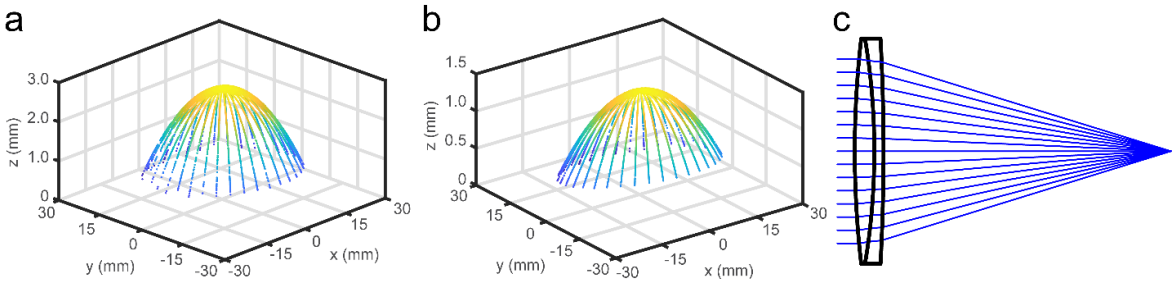

Figure 6-1 - Microscope objective lens characterization (a), (b) Point-cloud data of upper and lower surfaces of the objective lens measured using OCT. (c) Model of objective with estimated intermediate curvature and glass types.

6.2.3. Scan-head design

Spectrally encoded reflectometry (SER) and OCT in SECTR share a galvanometer scanner (SER scan-axis and OCT fast-axis) to ensure co-registration between SER and OCT field-of-views (FOVs) and concurrent acquisition of an *en face* SER image with each OCT cross-section (Figure 6-2 (a), (b)). Here, SER and OCT paths were combined collinearly across a D-shaped mirror (DM) and folded using a custom double-pass scan lens (fdp). The SECTR scan-head was coupled to a 5.76x magnifying relay (Figure 6-2 (c)), folded into a custom rapid-prototyped scan-head, and mounted to a Zeiss VISU 200 ophthalmic surgical microscope (Figure 6-2 (d)). iSECTR and surgical microscope FOVs were combined across a dichroic mirror in Fourier plane behind the objective lens. Total increase in axial length of the surgical microscope was 55.59 mm. During retinal imaging, the combination of surgical microscope objective and binocular indirect ophthalmomicroscope (BIOM) reduction and relay lenses form a 13.1x demagnifying relay. SER and OCT were designed for a 1.76

and 1.69 optical mm spot-size at the pupil, respectively. Multimodal ophthalmic imaging was performed with 2.36 and 0.95 mW of optical power at the pupil for SER and OCT, respectively.

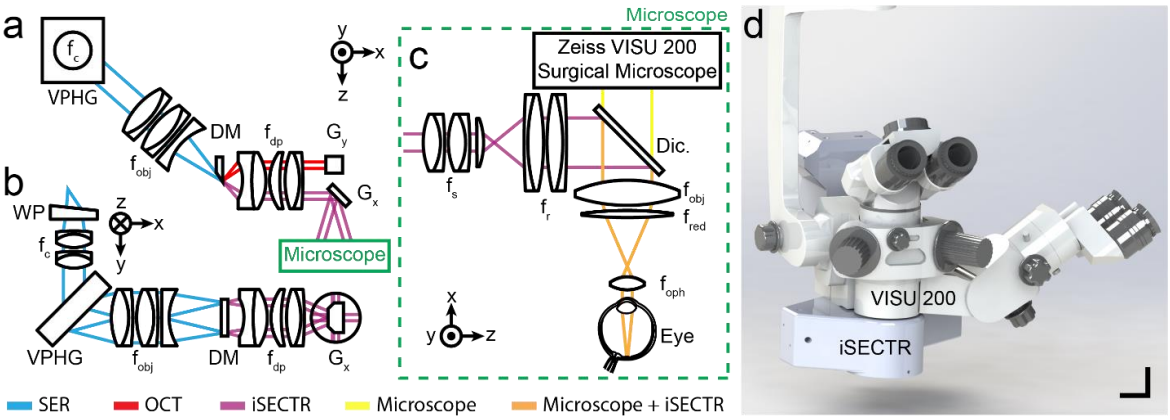

Figure 6-2 - Intraoperative SECTR (a), (b) Schematic of SECTR scan-head optics, (c) surgical microscope relay for multimodal retinal imaging through a BIOM, (d) CAD rendering of enclosure showing iSECTR scan-head attached to an ophthalmic surgical microscope, and (e) detection engine. BPD, dual-balanced photodiode; DCF, double clad fiber; Dic, dichroic mirror; DM, D-shaped mirror; f, collimating, double-pass, objective, ophthalmic, relay, scan lenses; FBG, fiber Bragg grating; G, galvanometer; M, mirror; MMF, multimode fiber; PC, polarization controller; PD, photodiode; VPHG, grating; WP, wedge prism. Scale bar: 25 mm

6.3. Results

6.3.1. Anterior segment *in vivo* human imaging

Ophthalmic imaging using iSECTR was performed on a healthy volunteer (Figure 6-3). *En face* SER and cross-sectional OCT images were acquired at 350 fps with 2560 x 1000 pix. (spectral x lateral). OCT volumes of 1000 B-scans were acquired in 2.86 s. Anterior segment SER (Figure 6-3 (a)) and OCT volume data (Figure 6-3 (b), (c)) showed co-registered lateral FOVs out to the limbus. In cross-section, iSECTR had sufficient range to visualize both the anterior cornea and lens.

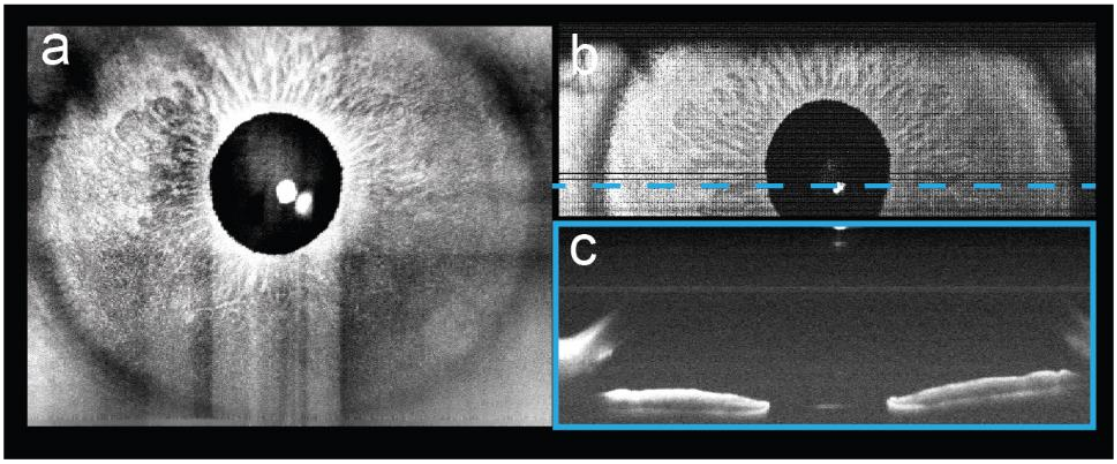

Figure 6-3 - *In vivo* iSECTR imaging of anterior segment (a) Single SER frame and (b) maximum intensity projection of volumetric OCT dataset with (c) a representative cross-section showing cornea, iris, and lens.

6.3.2. *In vivo* human retinal imaging

Human retinal imaging was also performed on a healthy volunteer with the same imaging parameters as anterior segment imaging. In the fundus, retinal and choroidal vasculature were readily visible on SER (Figure 6-4 (a), (b)) and provided complementary contrast to the OCT volume projection (Figure 6-4 (c)-(e)).

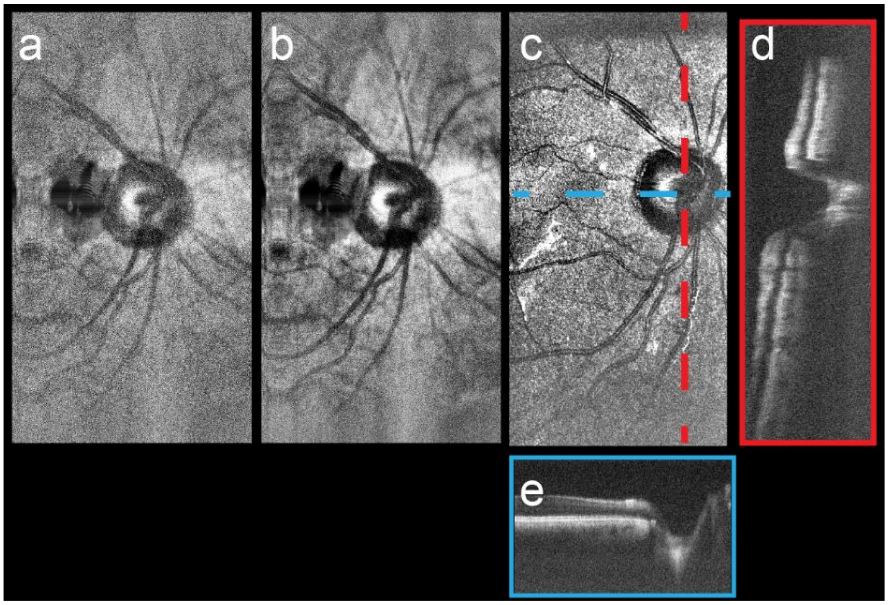

Figure 6-4 - In vivo iSECTR imaging of human retina . (a) Single and (b) 4-frame average of SER and (c)-(e) corresponding OCT data of the retina.

6.4. Conclusion

We presented optimized designs for multimodal ophthalmic imaging with iSECTR integrated with a surgical microscope. This was done using advanced lens characterization methods for improved optical performance simulations and throughput. Also, Clinical translation of iSECTR will benefit real-time instrument and FOV tracking for image-guided ophthalmic surgery.

7. Deep-learning based automated instrument tracking and adaptive-sampling of intraoperative OCT for video-rate volumetric imaging of ophthalmic surgical maneuvers

7.1. Introduction

Intraoperative optical coherence tomography (iOCT) enables volumetric imaging of surgical maneuvers. While previous studies have demonstrated the utility of iOCT for verifying completion of surgical goals, images were acquired over static field-of-views (FOVs) or required manual tracking of regions-of-interest (ROIs) [24]. The lack of automated instrument-tracking remains a critical barrier to real-time surgical feedback and iOCT-guided surgery [67,197].

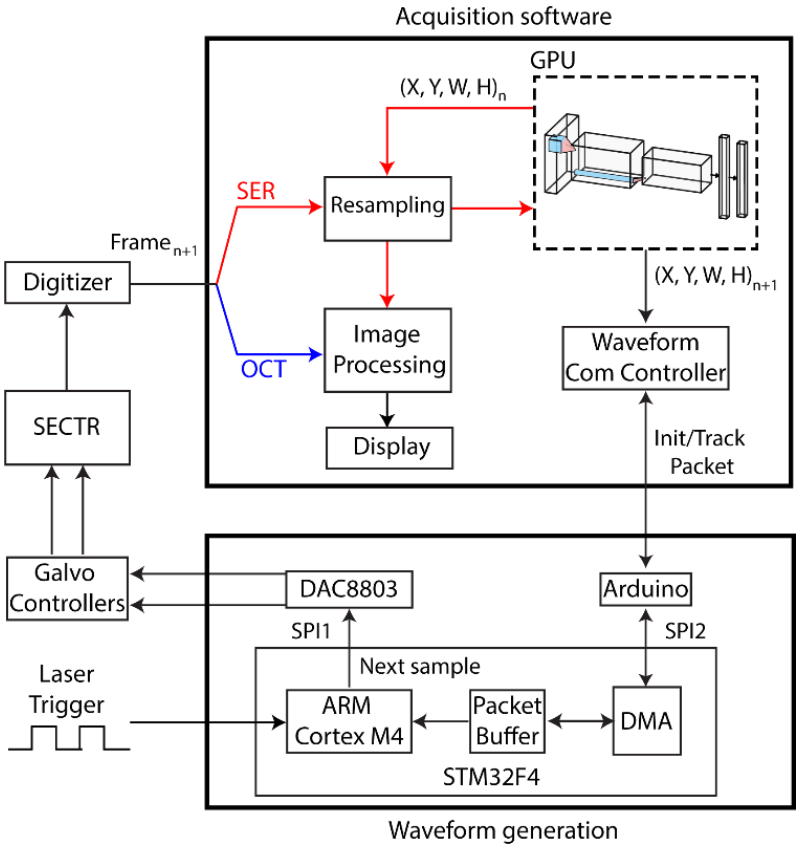

Figure 7-1 - Automated instrument-tracking framework and waveform generation hardware. SER frames are sent to the neural network for localization of the surgical instrument. Bounding box output from the neural network is processed in the software and positional information is sent to an Arduino microcontroller. The Arduino arbitrates communication of the tracking data between the PC and an ARM based microcontroller, which generates the scan waveform on a sample-by-sample basis based on the tracking information and gated by the laser trigger. Finally, the waveform data is sent to a DAC chip

to drive the galvanometer controllers. A resampling step on each acquired frame is performed using tracking information from the previous frame prior to processing by the neural network. n, frame number; GPU, graphical processing unit; W, width; H, heigh; DMA, direct memory access; SPI, serial peripheral interface; DAC, digital to analog converter.

Our group previously proposed to address this limitation by implementing active stereo-vision based instrument tracking [25]. However, accurate automatic instrument-tracking was limited to the anterior segment. More recently, groups have demonstrated instrument-tracking using volumetric OCT data [198,199]. While these methods allowed for highly-accurate tracking and pose estimation, the maximum tracking rate was confounded by OCT acquisition speeds and fundamental trade-offs between sampling density and FOV

We previously presented spectrally-encoded coherence tomography and reflectometry (SECTR), which provides simultaneous imaging of spatiotemporally co-registered orthogonal imaging planes (*en face* and cross-sectional) at several gigapixels-per-second [200]. We also demonstrated the potential applications of intraoperative SECTR (iSECTR) for visualization surgical dynamics [201,202] .

Here, we present automated surgical instrument-tracking and adaptive-sampling of OCT using a combination of deep-learning and SECTR. A GPU-accelerated deep neural network was trained using SER images for detection and localization of 25G internal limiting membrane (ILM) forceps at up to 50 Hz. Positional information was used for acquisition of adaptively sampled SER frames and OCT volumes, which were densely-sampled at the instrument tip and sparsely-sampled elsewhere to retain tracking features over a large FOV. We believe this method addresses critical barriers in the utility of iOCT for real-time surgical guidance and offers advantages over previous approaches by 1) reducing the instrument tracking problem to 2D space, which is simpler and more computationally efficient than 3D tracking or pose-estimation and allows direct leveraging of the recent advances in computer-vision software and hardware; and 2) decoupling tracking speed and performance from OCT system and acquisition parameters.

7.2. Methods

SECTR imaging was performed using a swept-source laser with 1050 nm and 105 nm bandwidth [200]. System line-rate was 400 kHz and imaging throughput was 2.3 gigasamples/s.

An open-source CUDA/C++ implementation of a state-of-the-art GPU-accelerated convolutional neural network (CNN) for object detection [203,204] was used for processing the SER frames. A training dataset was acquired showing various maneuvers using an ILM forceps on a custom retinal phantom. The dataset comprised 900 manually-labeled SER frames that showed fast and slow surface scraping, opening and closing of the ILM tip, instrument disappearance, and various amounts of blurring due to defocus/axial translation. The training software included built-in data augmentation through random contrast changes, cropping, and resizing. The network was compiled as a dynamically-linked library and integrated with custom C++ acquisition software (Figure 7-1).

During live acquisition, each SER frame was resampled based on previous bounding box information, and passed to independent display and tracking threads. In the tracking thread, the resampled frame was processed by the CNN to obtain the updated bounding box if the instrument was present. The bounding box coordinates were translated to data packets for the galvanometer drive waveform generation subsystem and transmitted over RS-232 using a USB-Serial interface. The computer was running Windows 10 on an octa-core Xeon E5 CPU, 64 GB RAM, and a NVIDIA GeForce GTX 1060 GPU with 3GB of memory.

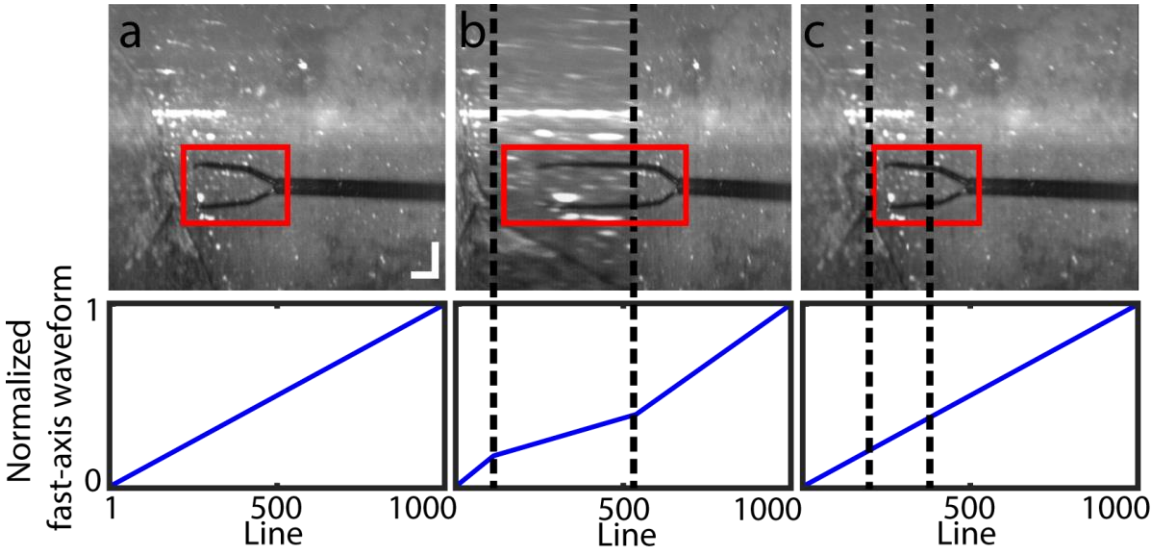

Figure 7-2 - Instrument detection and localization from raw SER frames. (a) Raw SER frame showing the bounding box output by the neural network. (b) Adaptively sampled SER frame, where the sampling density is quadrupled at the instrument tip and reduced elsewhere. (c) Resampled frame from (b) to correct distortion. Scale bar: 1 mm

An ARM-based microcontroller board (STM32F4-Discovery, STMicroelectronics) was used to calculate and output a new waveform sample for each laser trigger. The generated scan pattern was a saw-tooth with sinusoidal fly-back, and the calculation was performed based on the imaging and tracking parameters sent from the PC. An Arduino microcontroller arbitrated communication between the PC and the ARM board over serial-peripheral interface (SPI), and direct-memory access (DMA) was used on the ARM board to save CPU cycles. The calculated samples were then sent to a 14-bit digital-to-analog converter (DAC8803, Texas Instruments) over a separate SPI channel, and the generated signals were used to drive the galvanometer scanners.

7.3. Results

We demonstrated adaptive-sampling and real-time automated tracking of a 25G ILM forceps manipulating a membrane over a multi-layered retinal phantom (Figure 7-3). The acquired data show the instrument continuously within the FOV despite out-of-plane motion. The achieved tracking rate

was 55 Hz which was sufficient for real-time updates. Volumes were acquired with 1664x1000x18 pix. (spectral x lateral x lateral) at a volume rate of 18 Hz.

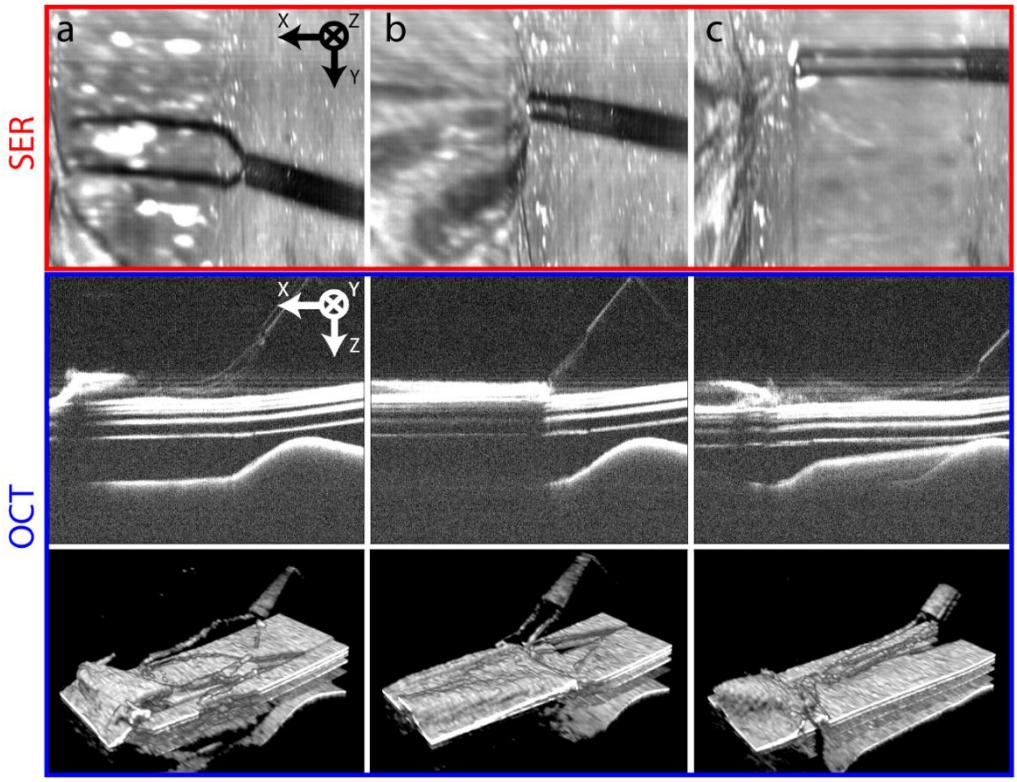

Figure 7-3 - Automated tracking and adaptive sampling results. Representative SECTR data showing adaptive-sampling and automated instrument-tracking of ILM forceps manipulating a membrane in a multilayered retinal phantom. SER frames show the instrument moving in both X- and Y-axes, with dense-sampling at the instrument tip. The instrument is continuously localized within the OCT FOV on corresponding cross-sections and volumetric renderings.

7.4. Conclusions

We presented a method for automated tracking of ophthalmic surgical instruments by combining SECTR with deep-learning and adaptive-sampling. The proposed solution addresses critical limitations in clincal translation of intraoperative OCT and offers several advantages over previous methods. The inherent co-registration between SER and OCT simplifies tracking and reduces it to a 2D detection problem. In this method, tracking speed is limited only by the GPU and tracking algorithm. This decouples tracking performance from OCT system and acquisition parameters and enables acquisition of densely sampled volumes at surgical instrument tips or other arbitrary ROIs

during dynamic surgical maneuvers. However, training on each expected instrument with rigorous quantitative evaluation of the CNN performance is still required. Additionally, utilizing a long short-term memory (LSTM) network architecture may further enhance the overall performance by leveraging the sequential nature of the tracking problem.

Chapter 8

8. Summary and Future Directions

This dissertation described methods and enabling technologies for the development of next-generation systems for intraoperative image-guidance in ophthalmology, addressing critical barriers to large-scale adoption of OCT in the ophthalmic surgical suite. Chapter 2 outlined a stereo-vision based tracking and control system which enabled continuous visualization of surgical maneuvers in the anterior segment. Constraining the tracking problem to the anterior segment allowed identification of potential limitations and provided insights for the development of imaging and tracking systems that were suitable for imaging in the posterior segment as well. The identified issues were mainly related to the limited depth provided by the utilized SDOCT system, and the lack of a well-defined transformation between the stereo-vision and the SDOCT FOVs which was confounded by the patient optics when imaging in the posterior segment.

To address these limitations, several solutions were explored as described in Chapter 3, namely extended-depth SDOCT, and swept-source multimodal imaging. The design of a custom reference arm with electronically-controllable delay enabled dynamic ranging within a closed-loop system guided by the position of the features-of-interest within the acquired B-scans. This was integrated with our stereo-vision tracking system and provided visualization of 3D-tracked surgical maneuvers. While this was still limited to imaging in the anterior segment, one main advantage was that the system was completely agnostic to the underlying OCT technology. Thus, this approach may be utilized as an extension for commercial systems that may still be currently in use.

Alternatively, preliminary experiments with multimodal imaging using SSOCT and SESLO proved to be a more promising approach due to the inherent spatiotemporal co-registration between both modalities. This co-registration was equally well-defined in both anterior and posterior segment imaging. Furthermore, the combination of swept-source illumination, point detection, and high-speed

digitizers was advantageous since it provided longer imaging range in OCT with a simple and more mechanically stable reference arm design that was amenable to clinical translation. This was further developed in Chapter 4. The technology was renamed to SECTR and provided wide-field multimodal imaging at more than 2 gigapixels/s over a retinal FOV of 45°. The performance of this system was verified and validated for *in vivo* human imaging. The combination of orthogonal scan-priority imaging planes facilitated 3D motion-tracking on a frame-by-frame basis. This provided several benefits in reconstruction of anatomically accurate volumetric datasets, and mosaicking of multiple adjacent datasets over an ultrawide FOV (> 90°). Therefore, we believe SECTR may have applications in clinical diagnostics and therapeutic planning, in addition to surgical guidance.

One of the main challenges in the development of intraoperative SECTR (iSECTR) was integration with the proprietary optics of the surgical microscope. The lack of a computer model for the microscope objective precluded optimization of the iSECTR optics for throughput and resolution. This was especially detrimental to the SER signal owing to its being a direct-detection modality. To that end, Chapter 5 outlined a method for non-destructive characterization of compound lenses using RCM, LCI, and computational ray-tracing. The method was validated on 6 commercial doublets and achieved an accuracy of < 2 waves in both spherical and chromatic aberrations within the characterization bandwidth. This method was utilized in Chapter 6 to reverse-engineer an estimated ZEMAX prescription for the surgical microscope objective, and *in vivo* multimodal imaging of the human retina using microscope-integrated iSECTR was successfully demonstrated.

In Chapter 7 we demonstrated automated instrument tracking and adaptive sampling in iSECTR. The multimodal imaging approach of iSECTR reduced the instrument-tracking problem to 2D and decoupled it from the underlying OCT acquisition rate. This enabled us to leverage machine-learning based object-detection algorithms for real-time tracking of the surgical instruments from SER frames. This was coupled with a custom-designed waveform generation hardware system that enabled real-time waveform modifications on a sample-by-sample basis. Finally, we demonstrated adaptively-

sampled iSECTR acquisition where the sampling density was maximized near the instrument tip, and sparse everywhere else. Adaptive sampling, as such, enabled acquisition of small, densely-sampled volumes around the instrument tip, while maintaining wide-field SER imaging for robust tracking, registration, and localization.

In the rest of this chapter, we describe potential future developments for enhanced visualization, resolution, and throughput in ophthalmic surgical guidance and diagnostic imaging. Finally, enhancements for more robust lens characterization systems and methods are proposed.

8.1. Augmented Reality in the surgical suite

Visualization of depth information intraoperatively is ergonomically challenging. Previous approaches included separate monitors or heads-up displays [71], custom stereoscopic optical relays of the OCT data through the eye-piece [57], and immersive integration with virtual-reality (VR) headsets [58]. However, most of the aforementioned approaches tend to be disruptive to the conventional surgical workflow, as the surgeon needs to switch their gaze between the microscope view and the OCT view, while simultaneously interpreting how these views correlate in 3D.

Recent advances in machine learning, computer vision algorithms, and processing hardware have enabled the development of novel approaches for automated segmentation of retinal layers with high fidelity [205–209]. Here, we propose a combination of iSECTR and machine learning based segmentation of retinal layers for augmented-reality (AR) style integration with the surgical microscope FOV. We believe this will provide an intuitive method for enhanced depth-perception intraoperatively with minimal interruption to the surgical workflow.

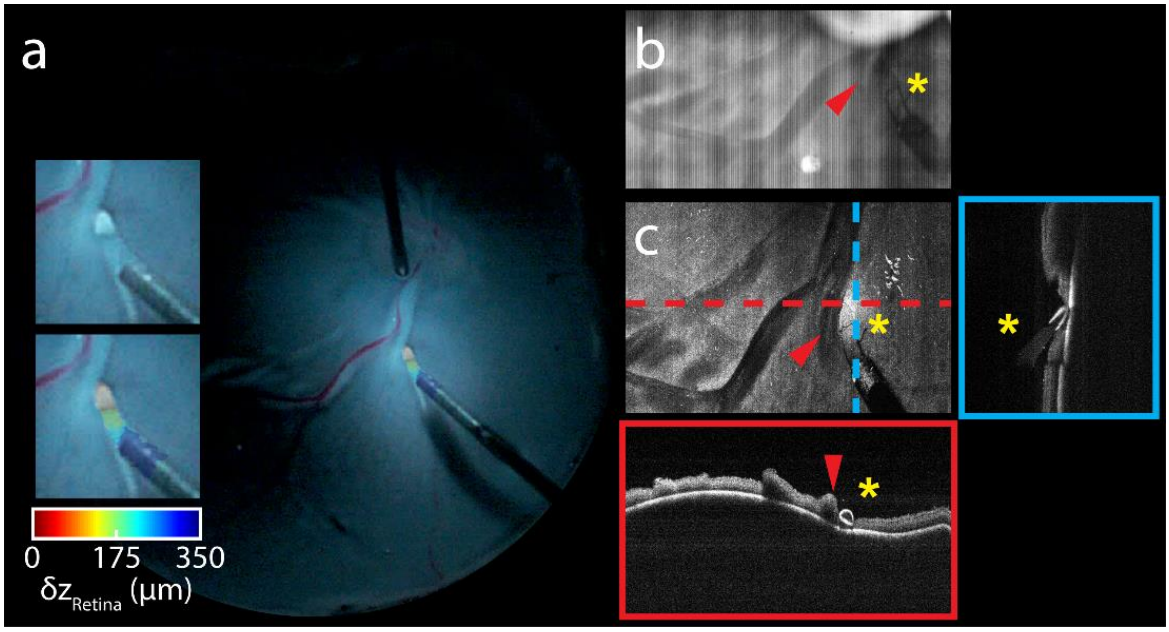

Figure 8-1 - iSECTR AR-integration with the surgical microsocope

As shown in Figure 8-1, manually segmented OCT cross-sections were used to encode the depth information as a color contrast on the microscope display. The depth information was calculated as the distance between the instrument tip and the retinal pigment epithelium (RPE). In a clinical system, this feature of interest may be customizable. The *en face* SER frames were used for automated registration and alignment of the OCT FOV to that of the surgical microscope. A block diagram of the acquisition, processing, and display pipelines is shown in Figure 8-2. The temporal throughput depends on the processing power, algorithmic efficiency, and acquisition rate. At the current SECTR acquisition rate (400 kHz), datasets sampled at 500 lines/B-scan and 20 frames/vol result in 40 Hz volumetric refresh rate, which is still faster than real-time.

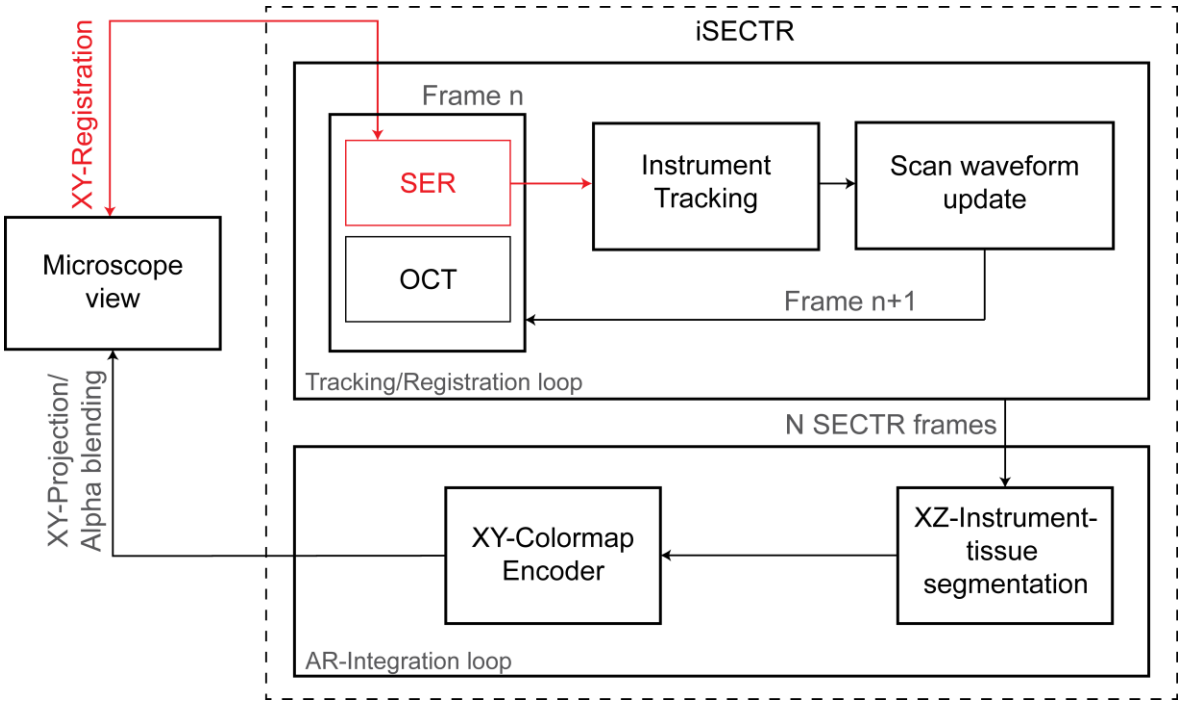

Figure 8-2 - iSECTR AR-integration block diagram. During acquisition, each SER frame is used to register SECTR FOV with the surgical microscope view, and for tracking of the surgical instrument. The scan waveform is updated the tracking information. After accumulation of N SECTR frames, the OCT cross-sections are segmented to extract quantitative depth information, which are encoded and projected on the microscope view in an augmented-reality fashion. N ≥ 1 for tracking single B-scans or volumes at the instrument tip.

The proposed approach will require several modifications to iSECTR acquisition hardware and software, which are described in the following sections.

8.1.1. Synchronized acquisition of surgical white-light microscopy and iSECTR frames

White-light frames from the surgical microscope may be acquired using a microscope-mounted camera. The acquisition needs to be synchronized to SER frames. This may be achieved by the same waveform generation system described in Chapter 7, by continuously arming a timer-counter interrupt in the microcontroller to fire after a specific number of laser triggers. The camera interface must provide sufficient bandwidth to match the SECTR data rates and avoid any inter-frame latency that may invalidate the registration results.

8.1.2. Parallel SER-microscope FOV registration and OCT segmentation

The SECTR processing pipelines need to be augmented. SER processing thread will include registration to the acquired microscope frames, and the OCT thread will include additional callbacks to a CNN-based segmentation process. Here, the registration and segmentation steps are potential bottlenecks, and may be offloaded to GPUs to minimize processing time. Thus, an additional GPU may be required such that one GPU will continuously run the instrument detection and tracking CNN, while additional GPU(s) will be responsible for the SER-Microscope registration and OCT segmentation.

8.1.3. Depth-map encoding and Augmented Reality overlays

Finally, the extracted depth information will be mapped to a visual overlay that may be integrated with the surgical microscope view. The AR overlays may be performed digitally, where the acquired white-light frame is modified before being sent to the display; relayed through the eye-piece; or optically projected on the surgical field. The latter approach, however, may be undesirable as it may raise phototoxicity concerns and may be more challenging to implement.

8.2. SECTR Design Optimizations

8.2.1. Split-polarization SECTR engine

The main design consideration when folding the SER and OCT beams together was minimization of both optical losses and the spatial separation between the origins of both modalities in the image space. To achieve this, a custom design prism mirror was used as explained in Section 4.2.2. While this provided optimal throughput compared to a beam-splitter, perfect overlap between the SER and OCT beams could not be achieved.

An alternative approach is to redesign the SECTR fiber-optic engine, such that output from the buffering stage is split in polarization. Polarized light delivered to either modality may then be folded downstream using a polarization-based beam splitter (PBS). This may achieve better overall optical throughput and overlap, simpler alignment, and is also amenable to polarization-based detection techniques to suppress specular reflection artifacts in the SER frames. One potential drawback to this approach may be an implicit SNR penalty due to tissue birefringence.

8.2.2. Custom fold-mirror design for enhanced signal collection in SECTR

One of the limitations in the current optical design of SECTR is that part of the detected SER signal was clipped at the fold-mirror. An alternative design is proposed in Figure 8-3. This design may further enhance the SNR compared to the current design. Here, a line-mirror is deposited on a round glass substrate. To minimize signal losses going through the glass, the material may be selected with low refractive index, and anti-reflection coating may be applied to both surfaces. The surfaces may also be designed such that they are mounted at an angle with respect to the incident SER beam, to avoid coupling of any residual back reflections.

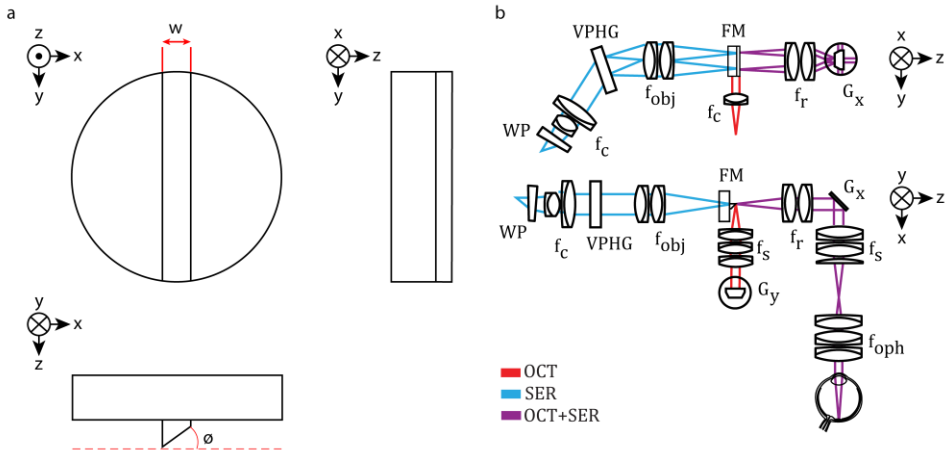

Figure 8-3 - Schematic of a novel SECTR fold-mirror design . (a) A round glass substrate is proposed for simple mounting and mechanical stability. The center of the substrate is silver coated with a width (w) equal to the expected OCT beam spot radius in the fold plane, and the cut angle (ϕ) and may be determined based on prespecified alignment requirements. (b) Representative schematics of SECTR utilizing the proposed fold mirror design

The mirror may also be designed at a custom angle with respect to the base, to accommodate a prespecified angle of incidence for the OCT beam, while allowing for simple on-axis alignment along the SER optical train.

8.3. Sub-diffraction-limited OCT imaging of the retina

Widefield and ultra-widefield imaging enabled by SECTR may be beneficial for ophthalmic diagnostic imaging by enabling the reconstruction of anatomically accurate densely sampled volumes, and providing access to the peripheral retina. However, lateral resolution in SECTR and most ophthalmic imaging systems is fundamentally limited by the aberrations of the eye [210].

The resolution may theoretically be enhanced by using beam diameters up to 7 mm at the pupil, leading to a diffraction-limited spot of approximately 2.5 µm at a wavelength of 840 nm [211]. However, the aberrations of the eye for entrance pupil sizes > 2 mm become dominant such that no gain in resolution is practically achieved [210]. Adaptive Optics SLO (AO-SLO) and AO-OCT systems enable diffraction-limited imaging for a fully dilated pupil using wavefront sensing to correct for the monochromatic optical aberrations [212–216]. However, AO systems require complex optical setups that are not yet clinically translatable [211].

Recent approaches employ computational aberration correction of line-field OCT or full-field OCT (FFOCT) volumes [211,217]. The aberration correction is performed either by correlating the local wavefront slope from low-resolution split-aperture reconstructions of the acquired image in the lateral plane [218], or by multiplying the acquired signal by a phase-conjugated aberration function which is iteratively optimized to maximize a sharpness metric [217]. While the latter is a more computationally intensive approach, it is simpler to implement and has been previously demonstrated in synthetic-aperture radar [219,220], and digital holography [221]. However, even with aberration correction, the diffraction-limited spot size is still insufficient to visualize cone photoreceptors in the fovea were the diameter may be as low as 1 µm [222–224].

Fourier Ptychographic Microscopy (FPM) is a recently proposed approach for increasing the space-bandwidth product of an optical system and achieve sub-diffraction-limited resolution [225,226]. The basic principle behind FPM is that the sample is illuminated at various angles, introducing phase diversity in the object space, which is conjugated to spectral shifts in the Frouier space. This effectively allows collection of different portions of the sample spectrum through the pass-band of the imaging system. An iterative computational optimization enables phase recovery which is required for coherent summation of the collected spectral bands. The resulting output from applying this technique is a super-resolved complex image of the sample with significantly more information than the diffraction limited image. However, the operation of FPM requires thin samples, such that purely coherent imaging may be assumed for the Fourier dualities to hold. Otherwise, multiply-scattered light distorts the phase, and precludes ptychographic reconstruction of the complex signal.

Here, we propose a combination of FPM, digital aberration correction, and full-field OCT (FFOCT) imaging for sub-diffraction-limited volumetric imaging of retinal structures. We hypothesize that, using FFOCT, the sample may be treated as a stack of thin samples, each corresponding to one coherence length in the axial dimension. This may facilitate application of FPM acquisition and reconstruction on each slice independently. More recently, FPM has been shown to enable recovery of the pupil function [227], which may be leveraged for aberration measurement and correction, and may be combined with the aforementioned correction methods.

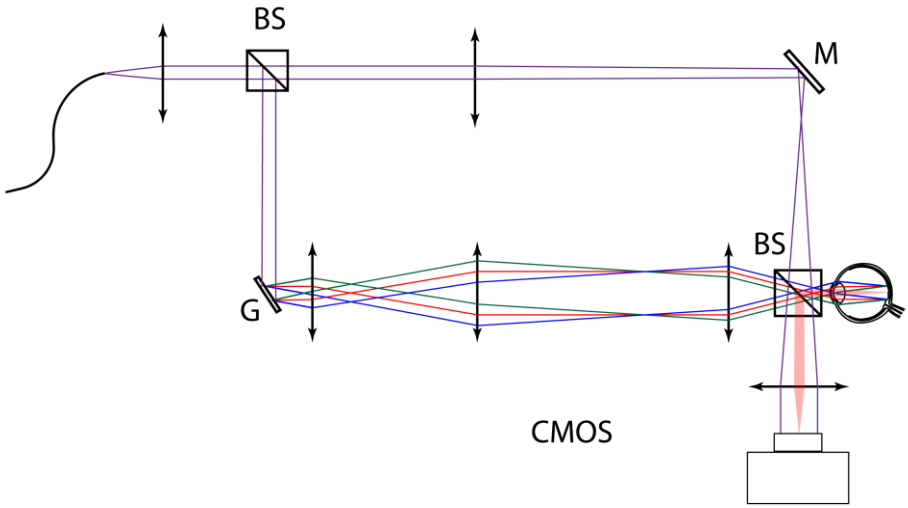

Figure 8-4 - Schematic of a FPM-FFOCT system. BS, beam splitter; M, fold mirror; G, galvanometer mirror

A schematic of the proposed FPM-FFOCT system is shown in Figure 8-4. To introduce phase diversity in the object space, a scanning galvanometer mirror may be placed in a conjugate plane. One challenge in this approach is that relatively high-speed acquisition is required to maintain the phase continuity along the acquired images in the lateral plane [211,217], which places strict requirements on the 2D detector. Hillman et al. utilized a Photron FASTCAM SA-Z, which was capable of acquiring frames with 896×368 pixel density at 60,000 frames/s [217]. The theoretical gain from this approach is at least 2x enhancement over the diffraction-limited resolution for a fully dilated pupil, for approximately 1.25 μm spot size at 840 nm. Further enhancement in resolution may be achieved by utilizing visible-light OCT [228,229].

8.4. Robust lens characterization with higher-order ray-tracing and wavelength diversity

The lens characterization method outlined in Chapter 5 had several limitations that were mainly due to the nature of the illumination source used, and the assumption of the spherical geometry of

the lens surfaces. Here, we describe several approaches for more accurate geometry and glass estimation, and for generalization to arbitrary surface profiles.

8.4.1. Higher-order ray-trace model

The measured LCI signal during profilometry of the different lens surfaces originates from purely specular reflections. This implies that there is a path length mismatch between the incident and reflected ray paths that changes with decenter as a function of the surface curvature. In our current approach, an SNR cut-off value was used to reject points where the path-length mismatch exceeded a certain threshold. This enabled measurement of surfaces in air with < 0.5% error. However, in certain cases, such as aspheric surfaces, it may be necessary to include points over the entire aperture for accurate fitting. Moreover, in optical distortion correction for internal surfaces, only the incident path was accounted for which limited the accuracy of the method.

An alternative approach is to model both the incident and the reflected paths. In this approach, the surface radius cannot be obtained from direct fitting. Rather, the radius needs to be optimized such that the cumulative ray paths matches the measured sags on the LCI profiles. While this is more computationally intensive, it may result in more accurate surface metrology as well as facilitate profilometry of aspheric surfaces, or arbitrary surface geometries by optimizing for an unkonwn surface gradient.

8.4.2. Motion mechanisms with higher degrees-of-freedom

An alternative approach for acquiring surface profiles is moving the lens-under-test (LUT) relative to the sample arm beam by more advanced motion mechanisms that accommodate rotations about the X and Y axes, in addition to translations along X, Y, and Z. This may facilitate profilometry protocols that rely on tilts to maximize the signal at different decenter, effectively tracking the changes in the surface normal, or the surface gradient, rather than acquiring direct measurements of

the surface sag. This decouples the fitting performance from the axial resolution of the utilized LCI system, does not require complicated ray-tracing models for surfaces imaged in air since the signal is always maximized at normal incidence, and is directly applicable to arbitrary surface profiles.

Another advantage of this approach is that surface profiles can be acquired over the entire aperture and can accommodate higher resolution features than what is possible with direct sag measurement. However, the accuracy of this approach will be limited by the precision and mechanical stability of the motion mechanism employed. Additionally, internal surface profiles will still require prior knowledge of the upstream materials and correction for the optical distortions in post-processing, as explained in section 5.2.

8.4.3. Multiple characterization wavelengths for more accurate glass estimation

The current approach for glass estimation relies on measurements of the focal plane shift, and optical thickness at the center wavelength of the illumination source. While including measurements of the optical thickness at the beginning and the end of the illumination spectrum provided additional constraints for more accurate estimation, the accuracy may be greatly enhanced by including additional sources in the VIS regime. This may be achieved by using a supercontinuum source along with a set of suitable filters and spectrometers. The following table shows phase and group refractive index of a standard commercial glass material at 3 wavelengths in the VIS regime and the 3 wavelengths used in our current system.

λ (nm)	450	550	650	760	830	885
n_p	1.5253	1.5185	1.5145	1.5116	1.5102	1.5092
n_g	1.5666	1.5462	1.5353	1.5284	1.5255	1.5239

Table 8-1 - Phase and group index of Schott BK7 in the VIS and NIR regimes [192]

It is to be noted that the relatively small difference between the np(760) and np(885) precluded accurate measurement of the focal plane shift as a function of wavelength. However, it can be seen that the stronger dispersion in the VIS regime alleviates this issue. Additionally, it can be noted that

the differences in the group index over the VIS wavelengths are up to 30 μm while it is < 5 μm in the NIR regime. Finally, with the resolution axial advantage at lower wavelengths, this makes VIS superior and more robust against measurement noise compared to NIR. We believe this may lead to highly accurate glass estimations and enable characterization of more complicated lens assemblies.

BIBLIOGRAPHY

1. D. Huang, E. A. Swanson, C. P. Lin, J. S. Schuman, W. G. Stinson, W. Chang, M. R. Hee, T. Flotte, K. Gregory, and C. A. Puliafito, "Optical coherence tomography," Science **254**, 1178–1181 (1991).
2. S. Moon and D. Y. Kim, "Ultra-high-speed optical coherence tomography with a stretched pulse supercontinuum source," Opt. Express **14**, 11575–11584 (2006).
3. R. Huber, M. Wojtkowski, and J. G. Fujimoto, "Fourier Domain Mode Locking (FDML): A new laser operating regime and applications for optical coherence tomography," Opt. Express **14**, 3225–3237 (2006).
4. B. Potsaid, V. Jayaraman, J. G. Fujimoto, J. Jiang, P. J. S. Heim, and A. E. Cable, "MEMS tunable VCSEL light source for ultrahigh speed 60kHz - 1MHz axial scan rate and long range centimeter class OCT imaging," in (2012), Vol. 8213, pp. 82130M-82130M–8.
5. T. Klein, W. Wieser, L. Reznicek, A. Neubauer, A. Kampik, and R. Huber, "Multi-MHz retinal OCT," Biomed. Opt. Express **4**, 1890–1908 (2013).
6. D. J. Fechtig, B. Grajciar, T. Schmoll, C. Blatter, R. M. Werkmeister, W. Drexler, and R. A. Leitgeb, "Line-field parallel swept source MHz OCT for structural and functional retinal imaging," Biomed. Opt. Express **6**, 716 (2015).
7. Z. Chen, M. Liu, M. Minneman, L. Ginner, E. Hoover, H. Sattmann, M. Bonesi, W. Drexler, and R. A. Leitgeb, "Phase-stable swept source OCT angiography in human skin using an akinetic source," Biomed. Opt. Express **7**, 3032–3048 (2016).
8. J. Xu, S. Song, W. Wei, and R. K. Wang, "Wide field and highly sensitive angiography based on optical coherence tomography with akinetic swept source," Biomed. Opt. Express **8**, 420–435 (2016).
9. "Zeiss Opti Lumera 700 and Rescan 700 Technical Data," https://www.zeiss.com/meditec/us/products/ophthalmology-optometry/retina/therapy/surgical-microscopes/opmi-lumera-700.html#technical-data.

10. "Leica Intrasurgical OCT EnFocus Technical Specifications," http://www.leica-microsystems.com/products/optical-coherence-tomography-oct/details/product/enfocus/specification/.

11. "Haag-Streit iOCT," https://www.haag-streit.com/haag-streit-surgical/products/ophthalmology/ioct/#c12831.

12. H. Yoo, J. W. Kim, M. Shishkov, E. Namati, T. Morse, R. Shubochkin, J. R. McCarthy, V. Ntziachristos, B. E. Bouma, F. A. Jaffer, and G. J. Tearney, "Intra-arterial catheter for simultaneous microstructural and molecular imaging in vivo," Nat. Med. **17**, 1680–1684 (2011).

13. M. J. Gora, J. S. Sauk, R. W. Carruth, K. A. Gallagher, M. J. Suter, N. S. Nishioka, L. E. Kava, M. Rosenberg, B. E. Bouma, and G. J. Tearney, "Tethered capsule endomicroscopy enables less invasive imaging of gastrointestinal tract microstructure," Nat. Med. **19**, 238–240 (2013).

14. S. A. Boppart, W. Luo, D. L. Marks, and K. W. Singletary, "Optical coherence tomography: feasibility for basic research and image-guided surgery of breast cancer," Breast Cancer Res. Treat. **84**, 85–97 (2004).

15. R. A. McLaughlin, B. C. Quirk, A. Curatolo, R. W. Kirk, L. Scolaro, D. Lorenser, P. D. Robbins, B. A. Wood, C. M. Saunders, and D. D. Sampson, "Imaging of Breast Cancer With Optical Coherence Tomography Needle Probes: Feasibility and Initial Results," IEEE J. Sel. Top. Quantum Electron. **18**, 1184–1191 (2012).

16. S. J. Erickson-Bhatt, R. M. Nolan, N. D. Shemonski, S. G. Adie, J. Putney, D. Darga, D. T. McCormick, A. J. Cittadine, A. M. Zysk, M. Marjanovic, E. J. Chaney, G. L. Monroy, F. A. South, K. A. Cradock, Z. G. Liu, M. Sundaram, P. S. Ray, and S. A. Boppart, "Real-time Imaging of the Resection Bed Using a Handheld Probe to Reduce Incidence of Microscopic Positive Margins in Cancer Surgery," Cancer Res. **75**, 3706–3712 (2015).

17. J. S. S. MD, C. A. P. MD, J. G. F. PhD, and J. S. D. MD, *Optical Coherence Tomography of Ocular Diseases*, 3 edition (Slack Incorporated, 2012).

18. N. A. Nassif, B. Cense, B. H. Park, M. C. Pierce, S. H. Yun, B. E. Bouma, G. J. Tearney, T. C. Chen, and J. F. de Boer, "In vivo high-resolution video-rate spectral-domain optical coherence tomography of the human retina and optic nerve," Opt. Express **12**, 367–376 (2004).

19. P. N. Dayani, R. Maldonado, S. Farsiu, and C. A. Toth, "Intraoperative use of handheld spectral domain optical coherence tomography imaging in macular surgery," Retina Phila. Pa **29**, 1457–1468 (2009).

20. Y. K. Tao, J. P. Ehlers, C. A. Toth, and J. A. Izatt, "Intraoperative spectral domain optical coherence tomography for vitreoretinal surgery," Opt. Lett. **35**, 3315–3317 (2010).

21. R. Ray, D. E. Barañano, J. A. Fortun, B. J. Schwent, B. E. Cribbs, C. S. Bergstrom, G. B. Hubbard, and S. K. Srivastava, "Intraoperative microscope-mounted spectral domain optical coherence tomography for evaluation of retinal anatomy during macular surgery," Ophthalmology **118**, 2212–2217 (2011).

22. L. A. Branchini, K. Gurley, J. S. Duker, and E. Reichel, "Use of Handheld Intraoperative Spectral-Domain Optical Coherence Tomography in a Variety of Vitreoretinal Diseases," Ophthalmic Surg. Lasers Imaging Retina **47**, 49–54 (2016).

23. J. P. Ehlers, W. J. Dupps, P. K. Kaiser, J. Goshe, R. P. Singh, D. Petkovsek, and S. K. Srivastava, "The Prospective Intraoperative and Perioperative Ophthalmic ImagiNg with Optical CoherEncE TomogRaphy (PIONEER) Study: 2-year results," Am. J. Ophthalmol. **158**, 999–1007 (2014).

24. O. M. Carrasco-Zevallos, B. Keller, C. Viehland, L. Shen, G. Waterman, B. Todorich, C. Shieh, P. Hahn, S. Farsiu, A. N. Kuo, C. A. Toth, and J. A. Izatt, "Live volumetric (4D) visualization and guidance of in vivo human ophthalmic surgery with intraoperative optical coherence tomography," Sci. Rep. **6**, 31689 (2016).

25. M. T. El-Haddad and Y. K. Tao, "Automated stereo vision instrument tracking for intraoperative OCT guided anterior segment ophthalmic surgical maneuvers," Biomed. Opt. Express **6**, 3014–3031 (2015).

26. K. M. Joos and J.-H. Shen, "Miniature real-time intraoperative forward-imaging optical coherence tomography probe," Biomed. Opt. Express **4**, 1342–1350 (2013).

27. J. D. Li, J. D. Malone, M. T. El-Haddad, A. M. Arquitola, K. M. Joos, S. N. Patel, and Y. K. Tao, "Image-guided feedback for ophthalmic microsurgery using multimodal intraoperative swept-source spectrally encoded scanning laser ophthalmoscopy and optical coherence tomography," in (2017), Vol. 10053, pp. 100530I-100530I–6.

28. S. Han, M. V. Sarunic, J. Wu, M. Humayun, and C. Yang, "Handheld forward-imaging needle endoscope for ophthalmic optical coherence tomography inspection," J. Biomed. Opt. **13**, 020505-020505–3 (2008).

29. T. Asami, H. Terasaki, Y. Ito, T. Sugita, H. Kaneko, J. Nishiyama, H. Namiki, M. Kobayashi, and N. Nishizawa, "Development of a Fiber-Optic Optical Coherence Tomography Probe for Intraocular UseFiber-Optic OCT Development for Intraocular Use," Invest. Ophthalmol. Vis. Sci. **57**, OCT568–OCT574 (2016).

30. H. J. Böhringer, D. Boller, J. Leppert, U. Knopp, E. Lankenau, E. Reusche, G. Hüttmann, and A. Giese, "Time-domain and spectral-domain optical coherence tomography in the analysis of brain tumor tissue," Lasers Surg. Med. **38**, 588–597 (2006).

31. F. T. Nguyen, A. M. Zysk, E. J. Chaney, J. G. Kotynek, U. J. Oliphant, F. J. Bellafiore, K. M. Rowland, P. A. Johnson, and S. A. Boppart, "Intraoperative Evaluation of Breast Tumor Margins with Optical Coherence Tomography," Cancer Res. **69**, 8790–8796 (2009).

32. M. Mujat, R. D. Ferguson, D. X. Hammer, C. Gittins, and N. Iftimia, "Automated algorithm for breast tissue differentiation in optical coherence tomography," J. Biomed. Opt. **14**, 034040-034040–9 (2009).

33. C.-P. Liang, J. Wierwille, T. Moreira, G. Schwartzbauer, M. S. Jafri, C.-M. Tang, and Y. Chen, "A forward-imaging needle-type OCT probe for image guided stereotactic procedures," Opt. Express **19**, 26283–26294 (2011).

34. K. M. Kennedy, R. A. McLaughlin, B. F. Kennedy, A. Tien, B. Latham, C. M. Saunders, and D. D. Sampson, "Needle optical coherence elastography for the measurement of microscale mechanical contrast deep within human breast tissues," J. Biomed. Opt. **18**, 121510–121510 (2013).

35. O. Assayag, K. Grieve, B. Devaux, F. Harms, J. Pallud, F. Chretien, C. Boccara, and P. Varlet, "Imaging of non-tumorous and tumorous human brain tissues with full-field optical coherence tomography," NeuroImage Clin. **2**, 549–557 (2013).

36. D. Savastru, E. W. Chang, S. Miclos, M. B. Pitman, A. Patel, and N. Iftimia, "Detection of breast surgical margins with optical coherence tomography imaging: a concept evaluation study," J. Biomed. Opt. **19**, 056001–056001 (2014).

37. F. A. South, E. J. Chaney, M. Marjanovic, S. G. Adie, and S. A. Boppart, "Differentiation of ex vivo human breast tissue using polarization-sensitive optical coherence tomography," Biomed. Opt. Express **5**, 3417–3426 (2014).

38. S. Wang, J. Li, R. E. Pollock, I. V. Larina, and K. V. Larin, "Development of optical sensor for soft tissue sarcoma boundary detection using optical coherence elastography," in *IEEE SENSORS 2014 Proceedings* (2014), pp. 1877–1880.

39. A. M. Zysk, K. Chen, E. Gabrielson, L. Tafra, E. A. M. Gonzalez, J. K. Canner, E. B. Schneider, A. J. Cittadine, P. S. Carney, S. A. Boppart, K. Tsuchiya, K. Sawyer, and L. K. Jacobs, "Intraoperative Assessment of Final Margins with a Handheld Optical Imaging Probe During Breast-Conserving Surgery May Reduce the Reoperation Rate: Results of a Multicenter Study," Ann. Surg. Oncol. **22**, 3356–3362 (2015).

40. C. Kut, K. L. Chaichana, J. Xi, S. M. Raza, X. Ye, E. R. McVeigh, F. J. Rodriguez, A. Quiñones-Hinojosa, and X. Li, "Detection of human brain cancer infiltration ex vivo and in vivo using quantitative optical coherence tomography," Sci. Transl. Med. **7**, 292ra100-292ra100 (2015).

41. W. M. Allen, L. Chin, P. Wijesinghe, R. W. Kirk, B. Latham, D. D. Sampson, C. M. Saunders, and B. F. Kennedy, "Wide-field optical coherence micro-elastography for intraoperative assessment of human breast cancer margins," Biomed. Opt. Express **7**, 4139–4153 (2016).

42. M. Villiger, D. Lorenser, R. A. McLaughlin, B. C. Quirk, R. W. Kirk, B. E. Bouma, and D. D. Sampson, "Deep tissue volume imaging of birefringence through fibre-optic needle probes for the delineation of breast tumour," Sci. Rep. **6**, (2016).

43. P. Wijesinghe, D. D. Sampson, and B. F. Kennedy, "Computational optical palpation: a finite-element approach to micro-scale tactile imaging using a compliant sensor," J. R. Soc. Interface **14**, 20160878 (2017).

44. S. Radhakrishnan, A. M. Rollins, J. E. Roth, S. Yazdanfar, V. Westphal, D. S. Bardenstein, and J. A. Izatt, "Real-Time Optical Coherence Tomography of the Anterior Segment at 1310 nm," Arch. Ophthalmol. **119**, 1179–1185 (2001).

45. C. D. Lu, M. F. Kraus, B. Potsaid, J. J. Liu, W. Choi, V. Jayaraman, A. E. Cable, J. Hornegger, J. S. Duker, and J. G. Fujimoto, "Handheld ultrahigh speed swept source optical coherence tomography instrument using a MEMS scanning mirror," Biomed. Opt. Express **5**, 293–311 (2014).

46. Y. Huang, G. J. Furtmüller, D. Tong, S. Zhu, W. P. A. Lee, G. Brandacher, and J. U. Kang, "MEMS-Based Handheld Fourier Domain Doppler Optical Coherence Tomography for Intraoperative Microvascular Anastomosis Imaging," PLOS ONE **9**, e114215 (2014).

47. F. LaRocca, D. Nankivil, T. DuBose, C. A. Toth, S. Farsiu, and J. A. Izatt, "In vivo cellular-resolution retinal imaging in infants and children using an ultracompact handheld probe," Nat. Photonics **10**, 580–584 (2016).

48. Y. K. Tao, S. K. Srivastava, and J. P. Ehlers, "Microscope-integrated intraoperative OCT with electrically tunable focus and heads-up display for imaging of ophthalmic surgical maneuvers," Biomed. Opt. Express **5**, 1877–1885 (2014).

49. R. Leitgeb, C. K. Hitzenberger, and A. F. Fercher, "Performance of fourier domain vs. time domain optical coherence tomography," Opt. Express **11**, 889–894 (2003).

50. M. A. Choma, M. V. Sarunic, C. Yang, and J. A. Izatt, "Sensitivity advantage of swept source and Fourier domain optical coherence tomography," Opt. Express **11**, 2183–2189 (2003).

51. M. Wojtkowski, R. Leitgeb, A. Kowalczyk, T. Bajraszewski, and A. F. Fercher, "In vivo human retinal imaging by Fourier domain optical coherence tomography," J. Biomed. Opt. **7**, 457–463 (2002).

52. S. R. Chinn, E. A. Swanson, and J. G. Fujimoto, "Optical coherence tomography using a frequency-tunable optical source," Opt. Lett. **22**, 340–342 (1997).

53. J. U. Kang, Y. Huang, K. Zhang, Z. Ibrahim, J. Cha, W. P. A. Lee, G. Brandacher, and P. L. Gehlbach, "Real-time three-dimensional Fourier-domain optical coherence tomography video image guided microsurgeries," J. Biomed. Opt. **17**, 0814031–0814036 (2012).

54. W. Wieser, W. Draxinger, T. Klein, S. Karpf, T. Pfeiffer, and R. Huber, "High definition live 3D-OCT in vivo: design and evaluation of a 4D OCT engine with 1 GVoxel/s," Biomed. Opt. Express **5**, 2963–2977 (2014).

55. O. Carrasco-Zevallos, B. Keller, C. Viehland, L. Shen, B. Todorich, C. Shieh, A. Kuo, C. Toth, and J. A. Izatt, "4D microscope-integrated OCT improves accuracy of ophthalmic surgical maneuvers," in F. Manns, P. G. Söderberg, and A. Ho, eds. (2016), p. 969306.

56. C. Viehland, B. Keller, O. M. Carrasco-Zevallos, D. Nankivil, L. Shen, S. Mangalesh, D. T. Viet, A. N. Kuo, C. A. Toth, and J. A. Izatt, "Enhanced volumetric visualization for real time 4D intraoperative ophthalmic swept-source OCT," Biomed. Opt. Express **7**, 1815–1829 (2016).

57. L. Shen, O. Carrasco-Zevallos, B. Keller, C. Viehland, G. Waterman, P. S. Hahn, A. N. Kuo, C. A. Toth, and J. A. Izatt, "Novel microscope-integrated stereoscopic heads-up display for intrasurgical optical coherence tomography," Biomed. Opt. Express **7**, 1711–1726 (2016).

58. L. Shen, B. Keller, O. Carrasco-Zevallos, C. Viehland, P. K. Bhullar, G. Waterman, A. N. Kuo, C. A. Toth, and J. A. Izatt, "Oculus Rift® as a Head Tracking, Stereoscopic Head Mounted Display for Intra-Operative OCT in Ophthalmic Surgery," Invest. Ophthalmol. Vis. Sci. **57**, 1701–1701 (2016).

59. I. Kozak, P. Banerjee, J. Luo, and C. Luciano, "Virtual reality simulator for vitreoretinal surgery using integrated OCT data," Clin. Ophthalmol. Auckl. NZ **8**, 669–672 (2014).

60. J. P. Ehlers, J. Goshe, W. J. Dupps, P. K. Kaiser, R. P. Singh, R. Gans, J. Eisengart, and S. K. Srivastava, "Determination of Feasibility and Utility of Microscope-Integrated Optical Coherence Tomography During Ophthalmic Surgery: The DISCOVER Study RESCAN Results," JAMA Ophthalmol. **133**, 1124–1132 (2015).

61. M. El-Haddad and Y. Tao, "Real-time dynamic depth tracking for arbitrarily long range OCT imaging and surgical instrument tracking using a Fourier domain optical delay line," Invest. Ophthalmol. Vis. Sci. **56**, 4089–4089 (2015).

62. G. W. Cheon, Y. Huang, J. Cha, P. L. Gehlbach, and J. U. Kang, "Accurate real-time depth control for CP-SSOCT distal sensor based handheld microsurgery tools," Biomed. Opt. Express **6**, 1942–1953 (2015).

63. C. Song, P. L. Gehlbach, and J. U. Kang, "Active tremor cancellation by a “Smart” handheld vitreoretinal microsurgical tool using swept source optical coherence tomography," Opt. Express **20**, 23414–23421 (2012).

64. C. Song, D. Y. Park, P. L. Gehlbach, S. J. Park, and J. U. Kang, "Fiber-optic OCT sensor guided “SMART” micro-forceps for microsurgery," Biomed. Opt. Express **4**, 1045–1050 (2013).

65. H. Yu, J.-H. Shen, R. J. Shah, N. Simaan, and K. M. Joos, "Evaluation of microsurgical tasks with OCT-guided and/or robot-assisted ophthalmic forceps," Biomed. Opt. Express **6**, 457–472 (2015).

66. E. A. Swanson and J. G. Fujimoto, "The ecosystem that powered the translation of OCT from fundamental research to clinical and commercial impact [Invited]," Biomed. Opt. Express **8**, 1638–1664 (2017).

67. O. M. Carrasco-Zevallos, C. Viehland, B. Keller, M. Draelos, A. N. Kuo, C. A. Toth, and J. A. Izatt, "Review of intraoperative optical coherence tomography: technology and applications [Invited]," Biomed. Opt. Express **8**, 1607–1637 (2017).

68. H. Hoerauf, C. Wirbelauer, C. Scholz, R. Engelhardt, P. Koch, H. Laqua, and R. Birngruber, "Slit-lamp-adapted optical coherence tomography of the anterior segment," Graefes Arch. Clin. Exp. Ophthalmol. **238**, 8–18 (2000).

69. L. D. Benito-Llopis, J. S. Mehta, R. I. Angunawela, M. Ang, and D. T. H. Tan, "Intraoperative Anterior Segment Optical Coherence Tomography: A Novel Assessment Tool during Deep Anterior Lamellar Keratoplasty," Am. J. Ophthalmol. **157**, 334-341.e3 (2014).

70. F. LaRocca, D. Nankivil, S. Farsiu, and J. A. Izatt, "Handheld simultaneous scanning laser ophthalmoscopy and optical coherence tomography system," Biomed. Opt. Express **4**, 2307–2321 (2013).

71. J. P. Ehlers, S. K. Srivastava, D. Feiler, A. I. Noonan, A. M. Rollins, and Y. K. Tao, "Integrative Advances for OCT-Guided Ophthalmic Surgery and Intraoperative OCT: Microscope Integration, Surgical Instrumentation, and Heads-Up Display Surgeon Feedback," PLoS ONE **9**, (2014).

72. N. D. Pasricha, C. Shieh, O. M. Carrasco-Zevallos, B. Keller, J. A. Izatt, C. A. Toth, and A. N. Kuo, "Real-Time Microscope-Integrated OCT to Improve Visualization in DSAEK for Advanced Bullous Keratopathy," Cornea **34**, 1606–1610 (2015).

73. B. Todorich, C. Shieh, P. J. DeSouza, O. M. Carrasco-Zevallos, D. L. Cunefare, S. S. Stinnett, J. A. Izatt, S. Farsiu, P. Mruthyunjaya, A. N. Kuo, and C. A. Toth, "Impact of Microscope-Integrated OCT on Ophthalmology Resident Performance of Anterior Segment Surgical Maneuvers in Model Eyes," Invest. Ophthalmol. Vis. Sci. **57**, OCT146–OCT153 (2016).

74. "Zeiss Cirrus HD OCT Technical Data," https://www.zeiss.com/meditec/us/products/ophthalmology-optometry/glaucoma/diagnostics/optical-coherence-thomography/oct-optical-coherence-tomography/cirrus-hd-oct.html#specifications.

75. S. Binder, C. I. Falkner-Radler, C. Hauger, H. Matz, and C. Glittenberg, "FEASIBILITY OF INTRASURGICAL SPECTRAL-DOMAIN OPTICAL COHERENCE TOMOGRAPHY:," Retina **31**, 1332–1336 (2011).

76. P. Steven, C. L. Blanc, E. Lankenau, M. Krug, S. Oelckers, L. M. Heindl, U. Gehlsen, G. Huettmann, and C. Cursiefen, "Optimising deep anterior lamellar keratoplasty (DALK) using intraoperative online optical coherence tomography (iOCT)," Br. J. Ophthalmol. **98**, 900–904 (2014).

77. S. Shimmura and K. Tsubota, "Deep anterior lamellar keratoplasty," Curr. Opin. Ophthalmol. **17**, 349–355 (2006).

78. P. Hahn, J. Migacz, R. O'Donnell, S. Day, A. Lee, P. Lin, R. Vann, A. Kuo, S. Fekrat, P. Mruthyunjaya, E. A. Postel, J. A. Izatt, and C. A. Toth, "Preclinical evaluation and intraoperative human retinal imaging with a high-resolution microscope-integrated spectral domain optical coherence tomography device," Retina Phila. Pa **33**, 1328–1337 (2013).

79. J. P. Ehlers, Y. K. Tao, S. Farsiu, R. Maldonado, J. A. Izatt, and C. A. Toth, "Visualization of Real-Time Intraoperative Maneuvers with a Microscope-Mounted Spectral Domain Optical Coherence Tomography System," Retina Phila. Pa **33**, 232–236 (2013).

80. M. T. El-Haddad, K. M. Joos, S. N. Patel, and Y. K. Tao, "Multimodal swept-source spectrally encoded scanning laser ophthalmoscopy and optical coherence tomography at 400 kHz," in (2017), Vol. 10053, pp. 1005305-1005305–5.

81. D. K. Sardar, G.-Y. Swanland, R. M. Yow, R. J. Thomas, and A. T. C. Tsin, "Optical properties of ocular tissues in the near infrared region," Lasers Med. Sci. **22**, 46–52 (2007).

82. D. Koo, H.-C. Park, P. L. Gehlbach, and C. Song, "Development and preliminary results of bimanual smart micro-surgical system using a ball-lens coupled OCT distance sensor," Biomed. Opt. Express **7**, 4816–4826 (2016).

83. C. Yeo, H. Park, S. Jang, P. L. Gehlbach, and C. Song, "Dual optical coherence tomography sensor guided, two-motor, horizontal SMART micro-scissors," Opt. Lett. **41**, 4723–4726 (2016).

84. J. P. Ehlers, Y. K. Tao, S. Farsiu, R. Maldonado, J. A. Izatt, and C. A. Toth, "Integration of a Spectral Domain Optical Coherence Tomography System into a Surgical Microscope for Intraoperative Imaging," Invest. Ophthalmol. Vis. Sci. **52**, 3153–3159 (2011).

85. G. Geerling, M. Müller, C. Winter, H. Hoerauf, S. Oelckers, H. Laqua, and R. Birngruber, "Intraoperative 2-Dimensional Optical Coherence Tomography as a New Tool for Anterior Segment Surgery," Arch. Ophthalmol. **123**, 253–257 (2005).

86. L. De Benito-Llopis, J. S. Mehta, R. I. Angunawela, M. Ang, and D. T. H. Tan, "Intraoperative anterior segment optical coherence tomography: a novel assessment tool during deep anterior lamellar keratoplasty," Am. J. Ophthalmol. **157**, 334-341.e3 (2014).

87. J. P. Ehlers, M. P. Ohr, P. K. Kaiser, and S. K. Srivastava, "NOVEL MICROARCHITECTURAL DYNAMICS IN RHEGMATOGENOUS RETINAL

DETACHMENTS IDENTIFIED WITH INTRAOPERATIVE OPTICAL COHERENCE TOMOGRAPHY:," Retina **33**, 1428–1434 (2013).

88. N. Hirnschall, S. Amir-Asgari, S. Maedel, and O. Findl, "Predicting the Postoperative Intraocular Lens Position Using Continuous Intraoperative Optical Coherence Tomography Measurements," Invest. Ophthalmol. Vis. Sci. **54**, 5196–5203 (2013).

89. R. B. Kucumen, E. Gorgun, N. M. Yenerel, and C. A. Utine, "Intraoperative Use of AS-OCT During Intrastromal Corneal Ring Segment Implantation," Ophthalmic Surg. Lasers Imaging Retina **43**, S109–S116 (2012).

90. L. B. Lee and S. K. Srivastava, "Intraoperative Spectral-Domain Optical Coherence Tomography During Complex Retinal Detachment Repair," Ophthalmic Surg. Lasers Imaging Retina (2011).

91. A. Miyakoshi, H. Ozaki, M. Otsuka, and A. Hayashi, "Efficacy of Intraoperative Anterior Segment Optical Coherence Tomography during Descemet's Stripping Automated Endothelial Keratoplasty," https://www.hindawi.com/journals/isrn/2014/562062/.

92. P. Steven, C. L. Blanc, K. Velten, E. Lankenau, M. Krug, S. Oelckers, L. M. Heindl, U. Gehlsen, G. Hüttmann, and C. Cursiefen, "Optimizing Descemet Membrane Endothelial Keratoplasty Using Intraoperative Optical Coherence Tomography," JAMA Ophthalmol. **131**, 1135–1142 (2013).

93. B. Keller, O. Carrasco-Zevallos, D. Nankivil, A. N. Kuo, and J. A. Izatt, "Real-Time Acquisition, Processing, and 3D Visualization of Anterior Segment Swept Source Optical Coherence Tomography (SSOCT) at 10 volumes (275 MVoxels) per second," .

94. J. P. Kolb, T. Klein, W. Wieser, W. Draxinger, and R. Huber, "Full volumetric video rate OCT of the posterior eye with up to 195.2 volumes/s," in *Optical Coherence Tomography and Coherence Domain Optical Methods in Biomedicine XIX* (International Society for Optics and Photonics, 2015), Vol. 9312, p. 931202.

95. A. R. Fuller, R. J. Zawadzki, B. Hamann, and J. S. Werner, "Comparison of real-time visualization of volumetric OCT data sets by CPU-slicing and GPU-ray casting methods," in *Ophthalmic Technologies XIX* (International Society for Optics and Photonics, 2009), Vol. 7163, p. 716312.

96. J. Probst, P. Koch, and G. Hüttmann, "Real-time 3D rendering of optical coherence tomography volumetric data," in P. E. Andersen and B. E. Bouma, eds. (2009), p. 73720Q.

97. R. J. Zawadzki, A. R. Fuller, S. S. Choi, D. F. Wiley, B. Hamann, and J. S. Werner, "Improved representation of retinal data acquired with volumetric Fd-OCT: co-registration, visualization, and reconstruction of a large field of view," in *Ophthalmic Technologies XVIII* (International Society for Optics and Photonics, 2008), Vol. 6844, p. 68440C.

98. Y. K. Tao, J. P. Ehlers, C. A. Toth, and J. A. Izatt, "Visualization of vitreoretinal surgical manipulations using intraoperative spectral domain optical coherence tomography," in (2011), Vol. 7889, pp. 78890F-78890F–10.

99. D. Burschka, J. J. Corso, M. Dewan, W. Lau, M. Li, H. Lin, P. Marayong, N. Ramey, G. D. Hager, B. Hoffman, D. Larkin, and C. Hasser, "Navigating inner space: 3-D assistance for minimally invasive surgery," Robot. Auton. Syst. **52**, 5–26 (2005).

100. Y. Li, C. Chen, X. Huang, and J. Huang, "Instrument Tracking via Online Learning in Retinal Microsurgery," in *Medical Image Computing and Computer-Assisted Intervention – MICCAI 2014* (Springer, Cham, 2014), pp. 464–471.

101. R. Sznitman, R. Richa, R. H. Taylor, B. Jedynak, and G. D. Hager, "Unified Detection and Tracking of Instruments during Retinal Microsurgery," IEEE Trans. Pattern Anal. Mach. Intell. **35**, 1263–1273 (2013).

102. R. Sznitman, K. Ali, R. Richa, R. H. Taylor, G. D. Hager, and P. Fua, "Data-Driven Visual Tracking in Retinal Microsurgery," in *Medical Image Computing and Computer-Assisted Intervention – MICCAI 2012* (Springer, Berlin, Heidelberg, 2012), pp. 568–575.

103. R. Richa, M. Balicki, E. Meisner, R. Sznitman, R. Taylor, and G. Hager, "Visual Tracking of Surgical Tools for Proximity Detection in Retinal Surgery," in *Information Processing in Computer-Assisted Interventions* (Springer, Berlin, Heidelberg, 2011), pp. 55–66.

104. E. Lugez, H. Sadjadi, D. R. Pichora, R. E. Ellis, S. G. Akl, and G. Fichtinger, "Electromagnetic tracking in surgical and interventional environments: usability study," Int. J. Comput. Assist. Radiol. Surg. **10**, 253–262 (2015).

105. J. B. West and C. R. Maurer, "Designing optically tracked instruments for image-guided surgery," IEEE Trans. Med. Imaging **23**, 533–545 (2004).

106. J. Ren, J. Wu, E. J. McDowell, and C. Yang, "Manual-scanning optical coherence tomography probe based on position tracking," Opt. Lett. **34**, 3400–3402 (2009).

107. D. Grest, T. Petersen, and V. Krüger, "A Comparison of Iterative 2D-3D Pose Estimation Methods for Real-Time Applications," in *Image Analysis* (Springer, Berlin, Heidelberg, 2009), pp. 706–715.

108. D. Oberkampf, D. F. DeMenthon, and L. S. Davis, "Iterative Pose Estimation Using Coplanar Feature Points," Comput. Vis. Image Underst. **63**, 495–511 (1996).

109. O. Findl, W. Drexler, R. Menapace, H. Heinzl, C. K. Hitzenberger, and A. F. Fercher, "Improved prediction of intraocular lens power using partial coherence interferometry," J. Cataract Refract. Surg. **27**, 861–867 (2001).

110. J. Németh, O. Fekete, and N. Pesztenlehrer, "Optical and ultrasound measurement of axial length and anterior chamber depth for intraocular lens power calculation," J. Cataract Refract. Surg. **29**, 85–88 (2003).

111. Z. Zhang, "A flexible new technique for camera calibration," IEEE Trans. Pattern Anal. Mach. Intell. **22**, 1330–1334 (2000).

112. "Camera Calibration Toolbox for Matlab," http://www.vision.caltech.edu/bouguetj/calib_doc/index.html.

113. E. Trucco and A. Verri, *Introductory Techniques for 3-D Computer Vision* (Prentice Hall, 1998).

114. Y. Huang, X. Liu, C. Song, and J. U. Kang, "Motion-compensated hand-held common-path Fourier-domain optical coherence tomography probe for image-guided intervention," Biomed. Opt. Express **3**, 3105–3118 (2012).

115. A. M. Rollins, M. D. Kulkarni, S. Yazdanfar, R. Ung-arunyawee, and J. A. Izatt, "In vivo video rate optical coherence tomography," Opt. Express **3**, 219–229 (1998).

116. K. K. M. Silva, A. V. Zvyagin, and D. D. Sampson, "Extended range, rapid scanning optical delay line for biomedical interferometric imaging," Electron. Lett. **35**, 1404–1406 (1999).

117. R. H. Webb, G. W. Hughes, and F. C. Delori, "Confocal scanning laser ophthalmoscope," Appl. Opt. **26**, 1492–1499 (1987).

118. R. D. Ferguson, D. X. Hammer, and R. H. Webb, "A Line-Scanning Laser Ophthalmoscope (LSLO)," Invest. Ophthalmol. Vis. Sci. **44**, 3624–3624 (2003).

119. G. J. Tearney, R. H. Webb, and B. E. Bouma, "Spectrally encoded confocal microscopy," Opt. Lett. **23**, 1152–1154 (1998).

120. Y. K. Tao, S. Farsiu, and J. A. Izatt, "Interlaced spectrally encoded confocal scanning laser ophthalmoscopy and spectral domain optical coherence tomography," Biomed. Opt. Express **1**, 431–440 (2010).

121. Y. K. Tao and J. A. Izatt, "Spectrally encoded confocal scanning laser ophthalmoscopy," Opt. Lett. **35**, 574–576 (2010).

122. E. D. Montigny, W.-J. Madore, O. Ouellette, G. Bernard, M. Leduc, M. Strupler, C. Boudoux, and N. Godbout, "Double-clad fiber coupler for partially coherent detection," Opt. Express **23**, 9040–9051 (2015).

123. S. Lemire-Renaud, M. Strupler, F. Benboujja, N. Godbout, and C. Boudoux, "Double-clad fiber with a tapered end for confocal endomicroscopy," Biomed. Opt. Express **2**, 2961–2972 (2011).

124. M. Wojtkowski, V. J. Srinivasan, T. H. Ko, J. G. Fujimoto, A. Kowalczyk, and J. S. Duker, "Ultrahigh-resolution, high-speed, Fourier domain optical coherence tomography and methods for dispersion compensation," Opt. Express **12**, 2404–2422 (2004).

125. S.-H. Choi, W.-H. Kim, Y.-J. Lee, H. Lee, W.-J. Lee, J.-D. Yang, J.-W. Shim, and J.-W. Kim, "Visualization of Epidermis and Dermal Cells in ex vivo Human Skin Using the Confocal and Two-photon Microscopy," J. Opt. Soc. Korea **15**, 61–67 (2011).

126. I. Veilleux, J. A. Spencer, D. P. Biss, D. Cote, and C. P. Lin, "In Vivo Cell Tracking With Video Rate Multimodality Laser Scanning Microscopy," IEEE J. Sel. Top. Quantum Electron. **14**, 10–18 (2008).

127. M. Rajadhyaksha, R. R. Anderson, and R. H. Webb, "Video-rate confocal scanning laser microscope for imaging human tissues in vivo," Appl. Opt. **38**, 2105–2115 (1999).

128. N. Iftimia, R. D. Ferguson, M. Mujat, A. H. Patel, E. Z. Zhang, W. Fox, and M. Rajadhyaksha, "Combined reflectance confocal microscopy/optical coherence tomography imaging for skin burn assessment," Biomed. Opt. Express **4**, 680–695 (2013).

129. J. A. Izatt, E. A. Swanson, J. G. Fujimoto, M. R. Hee, and G. M. Owen, "Optical coherence microscopy in scattering media," Opt. Lett. **19**, 590–592 (1994).

130. *Handbook of Biological Confocal Microscopy | James Pawley | Springer* (n.d.).

131. D. Terhorst, A. Maltusch, E. Stockfleth, S. Lange-Asschenfeldt, W. Sterry, M. Ulrich, and B. Lange-Asschenfeldt, "Reflectance confocal microscopy for the evaluation of acute epidermal wound healing," Wound Repair Regen. **19**, 671–679 (2011).

132. P. Guitera, G. Pellacani, C. Longo, S. Seidenari, M. Avramidis, and S. W. Menzies, "In vivo reflectance confocal microscopy enhances secondary evaluation of melanocytic lesions," J. Invest. Dermatol. **129**, 131–138 (2009).

133. E. S. Flores, M. Cordova, K. Kose, W. Phillips, A. Rossi, K. Nehal, and M. Rajadhyaksha, "Intraoperative imaging during Mohs surgery with reflectance confocal microscopy: initial clinical experience," J. Biomed. Opt. **20**, 61103 (2015).

134. C. E. Scarff, "Reflectance confocal microscopy of cutaneous tumors: an atlas with clinical, dermoscopic and histological correlations," Australas. J. Dermatol. **50**, 152–152 (2009).

135. V. Ntziachristos, "Going deeper than microscopy: the optical imaging frontier in biology," Nat. Methods **7**, 603–614 (2010).

136. R. C. Hughes and C. Alessi-Fox, "Reflectance Confocal Microscopy," in *The Melanocytic Proliferations*, A. N. C. MD, C. M. gro MD, and rtin C. M. J. MD, eds. (John Wiley & Sons, Inc., 2014), pp. 474–487.

137. M. Rajadhyaksha, M. Grossman, D. Esterowitz, R. H. Webb, and R. R. Anderson, "In vivo confocal scanning laser microscopy of human skin: melanin provides strong contrast," J. Invest. Dermatol. **104**, 946–952 (1995).

138. T. Klein, W. Wieser, C. M. Eigenwillig, B. R. Biedermann, and R. Huber, "Megahertz OCT for ultrawide-field retinal imaging with a 1050nm Fourier domain mode-locked laser," Opt. Express **19**, 3044–3062 (2011).

139. A. Camino, M. Zhang, C. Dongye, A. D. Pechauer, T. S. Hwang, S. T. Bailey, B. Lujan, D. J. Wilson, D. Huang, and Y. Jia, "Automated registration and enhanced processing of clinical optical coherence tomography angiography," Quant. Imaging Med. Surg. **6**, 391–401 (2016).

140. M. F. Kraus, B. Potsaid, M. A. Mayer, R. Bock, B. Baumann, J. J. Liu, J. Hornegger, and J. G. Fujimoto, "Motion correction in optical coherence tomography volumes on a per A-scan basis using orthogonal scan patterns," Biomed. Opt. Express **3**, 1182–1199 (2012).

141. P. Zang, G. Liu, M. Zhang, C. Dongye, J. Wang, A. D. Pechauer, T. S. Hwang, D. J. Wilson, D. Huang, D. Li, and Y. Jia, "Automated motion correction using parallel-strip registration for wide-field en face OCT angiogram," Biomed. Opt. Express **7**, 2823–2836 (2016).

142. J. Lezama, D. Mukherjee, R. P. McNabb, G. Sapiro, A. N. Kuo, and S. Farsiu, "Segmentation guided registration of wide field-of-view retinal optical coherence tomography volumes," Biomed. Opt. Express **7**, 4827–4846 (2016).

143. Y. Chen, Y.-J. Hong, S. Makita, and Y. Yasuno, "Three-dimensional eye motion correction by Lissajous scan optical coherence tomography," Biomed. Opt. Express **8**, 1783–1802 (2017).

144. S. Choi, P. Kim, R. Boutilier, M. Y. Kim, Y. J. Lee, and H. Lee, "Development of a high speed laser scanning confocal microscope with an acquisition rate up to 200 frames per second," Opt. Express **21**, 23611–23618 (2013).

145. T. Tanaami, S. Otsuki, N. Tomosada, Y. Kosugi, M. Shimizu, and H. Ishida, "High-speed 1-frame/ms scanning confocal microscope with a microlens and Nipkow disks," Appl. Opt. **41**, 4704–4708 (2002).

146. E. Wang, C. M. Babbey, and K. W. Dunn, "Performance comparison between the high-speed Yokogawa spinning disc confocal system and single-point scanning confocal systems," J. Microsc. **218**, 148–159 (2005).

147. C. Boudoux, S. Yun, W. Oh, W. White, N. Iftimia, M. Shishkov, B. Bouma, and G. Tearney, "Rapid wavelength-swept spectrally encoded confocal microscopy," Opt. Express **13**, 8214–8221 (2005).

148. S. C. Schlachter, D. Kang, M. J. Gora, P. Vacas-Jacques, T. Wu, R. W. Carruth, E. J. Wilsterman, B. E. Bouma, K. Woods, and G. J. Tearney, "Spectrally encoded confocal microscopy of esophageal tissues at 100 kHz line rate," Biomed. Opt. Express **4**, 1636–1645 (2013).

149. J. D. Malone, M. T. El-Haddad, I. Bozic, L. A. Tye, L. Majeau, N. Godbout, A. M. Rollins, C. Boudoux, K. M. Joos, S. N. Patel, and Y. K. Tao, "Simultaneous multimodal ophthalmic imaging using swept-source spectrally encoded scanning laser ophthalmoscopy and optical coherence tomography," Biomed. Opt. Express **8**, 193–206 (2017).

150. C. Glazowski and M. Rajadhyaksha, "Optimal detection pinhole for lowering speckle noise while maintaining adequate optical sectioning in confocal reflectance microscopes," J. Biomed. Opt. **17**, 0850011–0850015 (2012).

151. T. Wilson1 and A. R. Carlini, "Size of the detector in confocal imaging systems," Opt. Lett. **12**, 227–229 (1987).

152. S. Y. Ryu, H. Y. Choi, J. Na, E. S. Choi, and B. H. Lee, "Combined system of optical coherence tomography and fluorescence spectroscopy based on double-cladding fiber," Opt. Lett. **33**, 2347–2349 (2008).

153. S. Liang, A. Saidi, J. Jing, G. Liu, J. Li, J. Zhang, C. Sun, J. Narula, and Z. Chen, "Intravascular atherosclerotic imaging with combined fluorescence and optical coherence tomography probe based on a double-clad fiber combiner," J. Biomed. Opt. **17**, 0705011–0705013 (2012).

154. C. Olsovsky, T. Hinsdale, R. Cuenca, Y.-S. L. Cheng, J. M. Wright, T. D. Rees, J. A. Jo, and K. C. Maitland, "Handheld tunable focus confocal microscope utilizing a double-clad fiber coupler for in vivo imaging of oral epithelium," J. Biomed. Opt. **22**, 056008–056008 (2017).

155. A. Vašiček, "The Reflection of Light from Glass with Double and Multiple Films," JOSA **37**, 623–634 (1947).

156. P. M. Lane, "Terminal reflections in fiber-optic image guides," Appl. Opt. **48**, 5802–5810 (2009).

157. S. Martinez-Conde, S. L. Macknik, X. G. Troncoso, and D. H. Hubel, "Microsaccades: a neurophysiological analysis," Trends Neurosci. **32**, 463–475 (2009).

158. A.-H. Dhalla, K. Shia, and J. A. Izatt, "Efficient sweep buffering in swept source optical coherence tomography using a fast optical switch," Biomed. Opt. Express **3**, 3054–3066 (2012).

159. O. Pomerantzeff, M. Pankratov, G. J. Wang, and P. Dufault, "Wide-angle optical model of the eye," Am. J. Optom. Physiol. Opt. **61**, 166–176 (1984).

160. Z. Wang, H.-C. Lee, O. O. Ahsen, B. Lee, W. Choi, B. Potsaid, J. Liu, V. Jayaraman, A. Cable, M. F. Kraus, K. Liang, J. Hornegger, and J. G. Fujimoto, "Depth-encoded all-fiber swept source polarization sensitive OCT," Biomed. Opt. Express **5**, 2931–2949 (2014).

161. W. Choi, B. Potsaid, V. Jayaraman, B. Baumann, I. Grulkowski, J. J. Liu, C. D. Lu, A. E. Cable, D. Huang, J. S. Duker, and J. G. Fujimoto, "Phase-sensitive swept-source optical coherence tomography imaging of the human retina with a vertical cavity surface-emitting laser light source," Opt. Lett. **38**, 338–340 (2013).

162. R. Poddar, P. Raju, D. E. Cortés, J. S. Werner, M. J. Mannis, and R. J. Zawadzki, "Three-dimensional anterior segment imaging in patients with type 1 Boston Keratoprosthesis with switchable full depth range swept source optical coherence tomography," J. Biomed. Opt. **18**, 86002 (2013).

163. I. Arganda-Carreras, C. O. S. Sorzano, R. Marabini, J. M. Carazo, C. Ortiz-de-Solorzano, and J. Kybic, "Consistent and Elastic Registration of Histological Sections Using Vector-Spline Regularization," in *Computer Vision Approaches to Medical Image Analysis*, Lecture Notes in Computer Science (Springer, Berlin, Heidelberg, 2006), pp. 85–95.

164. "ANSI Z136.1 - Safe Use of Lasers - LIA," https://www.lia.org/publications/ansi/Z136-1.

165. B. D. Goldberg, B. J. Vakoc, W.-Y. Oh, M. J. Suter, S. Waxman, M. I. Freilich, B. E. Bouma, and G. J. Tearney, "Performance of reduced bit-depth acquisition for optical frequency domain imaging," Opt. Express **17**, 16957–16968 (2009).

166. J. P. Zinter and M. J. Levene, "Maximizing fluorescence collection efficiency in multiphoton microscopy," Opt. Express **19**, 15348–15362 (2011).

167. T. Kasahara, "Microscope objective lens," United States patent US6501603B2 (December 31, 2002).

168. J. A. Kurvits, M. Jiang, and R. Zia, "Comparative analysis of imaging configurations and objectives for Fourier microscopy," J. Opt. Soc. Am. A **32**, 2082 (2015).

169. D. Malacara-Doblado and I. Ghozeil, "Hartmann, Hartmann–Shack, and Other Screen Tests," in *Optical Shop Testing*, Daniellacara, ed. (John Wiley & Sons, Inc., 2007), pp. 361–397.

170. W. Brouwer, *Matrix Methods in Optical Instrument Design* (1964).

171. A. Gerrard and J. M. Burch, *Introduction to Matrix Methods in Optics* (Courier Corporation, 1994).

172. P.-D. Lin and C.-C. Hsueh, "6×6 matrix formalism of optical elements for modeling and analyzing 3D optical systems," Appl. Phys. B **97**, 135–143 (2009).

173. M. L. Dufour, G. Lamouche, V. Detalle, B. Gauthier, and P. Sammut, "Low-coherence interferometry – an advanced technique for optical metrology in industry," https://www.ingentaconnect.com/content/bindt/insight/2005/00000047/00000004/art00009.

174. S. Ortiz, D. Siedlecki, L. Remon, and S. Marcos, "Optical coherence tomography for quantitative surface topography," Appl. Opt. **48**, 6708–6715 (2009).

175. E. Martinez-Enriquez, P. Pérez-Merino, M. Velasco-Ocana, and S. Marcos, "OCT-based full crystalline lens shape change during accommodation in vivo," Biomed. Opt. Express **8**, 918–933 (2017).

176. R. C. Youngquist, S. Carr, and D. E. N. Davies, "Optical coherence-domain reflectometry: a new optical evaluation technique," Opt. Lett. **12**, 158–160 (1987).

177. S. Ortiz, D. Siedlecki, I. Grulkowski, L. Remon, D. Pascual, M. Wojtkowski, and S. Marcos, "Optical distortion correction in Optical Coherence Tomography for quantitative ocular anterior segment by three-dimensional imaging," Opt. Express **18**, 2782–2796 (2010).

178. G. J. Tearney, M. E. Brezinski, J. F. Southern, B. E. Bouma, M. R. Hee, and J. G. Fujimoto, "Determination of the refractive index of highly scattering human tissue by optical coherence tomography," Opt. Lett. **20**, 2258–2260 (1995).

179. V. N. Kumar and D. N. Rao, "Using interference in the frequency domain for precise determination of thickness and refractive indices of normal dispersive materials," JOSA B **12**, 1559–1563 (1995).

180. H. Maruyama, S. Inoue, T. Mitsuyama, M. Ohmi, and M. Haruna, "Low-coherence interferometer system for the simultaneous measurement of refractive index and thickness," Appl. Opt. **41**, 1315–1322 (2002).

181. J. Na, H. Y. Choi, E. S. Choi, C. Lee, and B. H. Lee, "Self-referenced spectral interferometry for simultaneous measurements of thickness and refractive index," Appl. Opt. **48**, 2461–2467 (2009).

182. P. H. Tomlins and R. K. Wang, "Simultaneous analysis of refractive index and physical thickness by Fourier domain optical coherence tomography," IEE Proc. - Optoelectron. **153**, 222–228 (2006).

183. T. Fukano and I. Yamaguchi, "Simultaneous measurement of thicknesses and refractive indices of multiple layers by a low-coherence confocal interference microscope," Opt. Lett. **21**, 1942–1944 (1996).

184. M. Haruna, M. Ohmi, T. Mitsuyama, H. Tajiri, H. Maruyama, and M. Hashimoto, "Simultaneous measurement of the phase and group indices and the thickness of transparent plates by low-coherence interferometry," Opt. Lett. **23**, 966–968 (1998).

185. T. Fukano and I. Yamaguchi, "Separation of measurement of the refractive index and the geometrical thickness by use of a wavelength-scanning interferometer with a confocal microscope," Appl. Opt. **38**, 4065–4073 (1999).

186. R. Chlebus, P. Hlubina, and D. Ciprian, "Direct measurement of group dispersion of optical components using white-light spectral interferometry," Opto-Electron. Rev. **15**, 144–148 (2007).

187. S. Diddams and J.-C. Diels, "Dispersion measurements with white-light interferometry," JOSA B **13**, 1120–1129 (1996).

188. D. Francis, H. D. Ford, and R. P. Tatam, "Spectrometer-based refractive index and dispersion measurement using low-coherence interferometry with confocal scanning," Opt. Express **26**, 3604–3617 (2018).

189. M. Galli, F. Marabelli, and G. Guizzetti, "Direct measurement of refractive-index dispersion of transparent media by white-light interferometry," Appl. Opt. **42**, 3910–3914 (2003).

190. C. Sáinz, P. Jourdain, R. Escalona, and J. Calatroni, "Real time interferometric measurements of dispersion curves," Opt. Commun. **111**, 632–641 (1994).

191. A. Piratelli-Filho, N. Anwer, C. M. Souzani, G. Devedzic, and R. V. Arencibia, "Error evaluation in reverse engineering of aspherical lenses," in *17th International Congress of Metrology* (EDP Sciences, 2015), p. 13007.

192. M. Polyansky, "refractiveindex.info," https://refractiveindex.info/cite.php.

193. "On the Limitations of the Confocal Scanning Optical Microscope as a Profilometer: Journal of Modern Optics: Vol 42, No 9," https://www.tandfonline.com/doi/abs/10.1080/09500349514551551.

194. L. Shen, O. Carrasco-Zevallos, B. Keller, C. Viehland, G. Waterman, P. Desouza, P. Hahn, A. Kuo, C. A. Toth, and J. A. Izatt, "Novel microscope-integrated stereoscopic display for intrasurgical optical coherence tomography," in *Ophthalmic Technologies XXV* (International Society for Optics and Photonics, 2015), Vol. 9307, p. 930706.

195. M. T. El-Haddad and Y. K. Tao, "Non-destructive geometric and refractive index characterization of single and multi-element lenses using optical coherence tomography," in *Optical Coherence Tomography and Coherence Domain Optical Methods in Biomedicine XXII* (International Society for Optics and Photonics, 2018), Vol. 10483, p. 104832O.

196. J. Polans, B. Jaeken, R. P. McNabb, P. Artal, and J. A. Izatt, "Wide-field optical model of the human eye with asymmetrically tilted and decentered lens that reproduces measured ocular aberrations," Optica **2**, 124–134 (2015).

197. M. T. El-Haddad and Y. K. Tao, "Advances in intraoperative optical coherence tomography for surgical guidance," Curr. Opin. Biomed. Eng. (2017).

198. B. Keller, M. Draelos, G. Tang, S. Farsiu, A. N. Kuo, K. Hauser, and J. A. Izatt, "Real-time corneal segmentation and 3D needle tracking in intrasurgical OCT," Biomed. Opt. Express **9**, 2716–2732 (2018).

199. N. Gessert, M. Schlüter, and A. Schlaefer, "A deep learning approach for pose estimation from volumetric OCT data," Med. Image Anal. **46**, 162–179 (2018).

200. M. T. El-Haddad, I. Bozic, and Y. K. Tao, "Spectrally encoded coherence tomography and reflectometry: Simultaneous en face and cross-sectional imaging at 2 gigapixels per second," J. Biophotonics **11**, e201700268 (2018).

201. J. D. Li, J. D. Malone, M. T. El-Haddad, A. M. Arquitola, K. M. Joos, S. N. Patel, and Y. K. Tao, "Image-guided feedback for ophthalmic microsurgery using multimodal intraoperative swept-source spectrally encoded scanning laser ophthalmoscopy and optical coherence tomography," in *Proc. of SPIE Vol* (2017), Vol. 10053, pp. 100530I–1.

202. J. D. Malone, M. T. El-Haddad, K. C. Leeburg, B. D. Terrones, and Y. K. Tao, "Resolution and throughput optimized intraoperative spectrally encoded coherence tomography and reflectometry (iSECTR) for multimodal imaging during ophthalmic microsurgery," in *Optical Coherence Tomography and Coherence Domain Optical Methods in Biomedicine XXII* (International Society for Optics and Photonics, 2018), Vol. 10483, p. 1048316.

203. J. Redmon and A. Farhadi, "YOLOv3: An Incremental Improvement," ArXiv180402767 Cs (2018).

204. Alexey, *Windows and Linux Version of Darknet Yolo v3 & v2 Neural Networks for Object Detection (Tensor Cores Are Used): AlexeyAB/Darknet* (2018).

205. O. Ronneberger, P. Fischer, and T. Brox, "U-Net: Convolutional Networks for Biomedical Image Segmentation," in *Medical Image Computing and Computer-Assisted Intervention – MICCAI 2015*, N. Navab, J. Hornegger, W. M. Wells, and A. F. Frangi, eds., Lecture Notes in Computer Science (Springer International Publishing, 2015), pp. 234–241.

206. L. Fang, D. Cunefare, C. Wang, R. H. Guymer, S. Li, and S. Farsiu, "Automatic segmentation of nine retinal layer boundaries in OCT images of non-exudative AMD patients using deep learning and graph search," Biomed. Opt. Express **8**, 2732–2744 (2017).

207. V. Kajić, B. Považay, B. Hermann, B. Hofer, D. Marshall, P. L. Rosin, and W. Drexler, "Robust segmentation of intraretinal layers in the normal human fovea using a novel statistical model based on texture and shape analysis," Opt. Express **18**, 14730–14744 (2010).

208. A. Shah, L. Zhou, M. D. Abrámoff, and X. Wu, "Multiple surface segmentation using convolution neural nets: application to retinal layer segmentation in OCT images," Biomed. Opt. Express **9**, 4509–4526 (2018).

209. K. A. Vermeer, J. van der Schoot, H. G. Lemij, and J. F. de Boer, "Automated segmentation by pixel classification of retinal layers in ophthalmic OCT images," Biomed. Opt. Express **2**, 1743–1756 (2011).

210. M. Ramamurthy and V. Lakshminarayanan, "Human Vision and Perception," in *Handbook of Advanced Lighting Technology*, R. Karlicek, C.-C. Sun, G. Zissis, and R. Ma, eds. (Springer International Publishing, 2017), pp. 757–784.

211. L. Ginner, A. Kumar, D. Fechtig, L. M. Wurster, M. Salas, M. Pircher, and R. A. Leitgeb, "Noniterative digital aberration correction for cellular resolution retinal optical coherence tomography in vivo," Optica **4**, 924–931 (2017).

212. A. Roorda, F. Romero-Borja, W. J. D. Iii, H. Queener, T. J. Hebert, and M. C. W. Campbell, "Adaptive optics scanning laser ophthalmoscopy," Opt. Express **10**, 405–412 (2002).

213. A. Dubra, Y. Sulai, J. L. Norris, R. F. Cooper, A. M. Dubis, D. R. Williams, and J. Carroll, "Noninvasive imaging of the human rod photoreceptor mosaic using a confocal adaptive optics scanning ophthalmoscope," Biomed. Opt. Express **2**, 1864–1876 (2011).

214. R. J. Zawadzki, S. M. Jones, S. Pilli, S. Balderas-Mata, D. Y. Kim, S. S. Olivier, and J. S. Werner, "Integrated adaptive optics optical coherence tomography and adaptive optics scanning laser ophthalmoscope system for simultaneous cellular resolution in vivo retinal imaging," Biomed. Opt. Express **2**, 1674–1686 (2011).

215. F. Felberer, J.-S. Kroisamer, B. Baumann, S. Zotter, U. Schmidt-Erfurth, C. K. Hitzenberger, and M. Pircher, "Adaptive optics SLO/OCT for 3D imaging of human photoreceptors in vivo," Biomed. Opt. Express **5**, 439–456 (2014).

216. Y. Jian, S. Lee, M. J. Ju, M. Heisler, W. Ding, R. J. Zawadzki, S. Bonora, and M. V. Sarunic, "Lens-based wavefront sensorless adaptive optics swept source OCT," Sci. Rep. **6**, 27620 (2016).

217. D. Hillmann, H. Spahr, C. Hain, H. Sudkamp, G. Franke, C. Pfäffle, C. Winter, and G. Hüttmann, "Aberration-free volumetric high-speed imaging of *in vivo* retina," Sci. Rep. **6**, 35209 (2016).

218. A. Kumar, W. Drexler, and R. A. Leitgeb, "Subaperture correlation based digital adaptive optics for full field optical coherence tomography," Opt. Express **21**, 10850 (2013).

219. J. R. Fienup, "Synthetic-aperture radar autofocus by maximizing sharpness," Opt. Lett. **25**, 221–223 (2000).

220. B. C. Flores, "Robust method for the motion compensation of ISAR imagery," in *Intelligent Robots and Computer Vision X: Algorithms and Techniques* (International Society for Optics and Photonics, 1992), Vol. 1607, pp. 512–518.

221. S. T. Thurman and J. R. Fienup, "Phase-error correction in digital holography," JOSA A **25**, 983–994 (2008).

222. "Cone Photoreceptors," http://retina.anatomy.upenn.edu/~rob/lance/cone.html.

223. "Photoreceptors by Helga Kolb – Webvision," (n.d.).

224. "OSA | Phase retrieval algorithms: a comparison," https://www.osapublishing.org/ao/abstract.cfm?URI=ao-21-15-2758.

225. G. Zheng, R. Horstmeyer, and C. Yang, "Wide-field, high-resolution Fourier ptychographic microscopy," Nat. Photonics **7**, 739–745 (2013).

226. X. Ou, R. Horstmeyer, C. Yang, and G. Zheng, "Quantitative phase imaging via Fourier ptychographic microscopy," Opt. Lett. **38**, 4845 (2013).

227. X. Ou, G. Zheng, and C. Yang, "Embedded pupil function recovery for Fourier ptychographic microscopy," Opt. Express **22**, 4960 (2014).

228. "Visible-light optical coherence tomography: a review," https://www.spiedigitallibrary.org/journals/journal-of-biomedical-optics/volume-22/issue-12/121707/Visible-light-optical-coherence-tomography-a-review/10.1117/1.JBO.22.12.121707.full?SSO=1.

229. S. P. Chong, T. Zhang, A. Kho, M. T. Bernucci, A. Dubra, and V. J. Srinivasan, "Ultrahigh resolution retinal imaging by visible light OCT with longitudinal achromatization," Biomed. Opt. Express **9**, 1477–1491 (2018).